TAC
15 June 2000

ITER
TECHNICAL ADVISORY
COMMITTEE MEETING

25-27 June 2000
St Petersburg

PROGRESS IN RESOLVING OPEN DESIGN ISSUES FROM THE ODR

Report by the Director

Table of Contents

1. Introduction

In January 2000, the ITER Meeting *"accepted the ITER-FEAT Outline Design Report, taking note of the TAC Report and recommendations, and agreed to transmit the report to the Parties for their consideration and domestic assessment".* It further *"agreed that the Outline Design Report provides the basis for continuing design work by JCT and Home Teams", and "recognising the importance to optimise a single agreed design,... asked the Director and JCT to interact with the Parties during the course of their domestic assessments. The Parties should keep the Director informed of the findings of their domestic assessments with a view to optimising a design for approval, following TAC review, at the coming ITER Council Meeting, in the context of the planned Joint Assessment."*

The above-mentioned interaction has now taken place, and the Parties have transmitted to the JCT their domestic assessments. Given the parallel nature of the continuing design work in the JCT and HomeTeams, as well as the Parties' assessment, some issues raised remain to be addressed by the developing design: for the most part either because the available experimental results do not provide a good enough basis for a confident extrapolation (for example ELMS, NTM stabilisation, steady state, etc.), or because the R&D on questions specific to ITER, and clearly identified, are ongoing (for example tritium codeposition with graphite and its removal, etc.) Nevertheless, as agreed at the Meeting, it has been possible to prepare "a progress report which will briefly summarise the choices made for the few remaining design options" addressing, where sufficiently known, the concerns of the Parties.

This report therefore covers all those design features of ITER which result from a resolution of a choice of options. More details on other features of the design will be given in the Final Design Report for ITER-FEAT, after more detailed engineering studies. The report also takes the opportunity to address issues raised by the physics assessments of the Parties, in discussions of the operating scenarios, projection sensitivities, and divertor-edge physics. The object of this report is not to repeat the ODR information, but to concentrate on the specific open issues and the progress towards their resolution.

2. Physics

2.1. Introduction

This report summarises the Physics analysis activities since the last TAC meeting, in an effort to address some of the recommendations raised by TAC and HTs. Also the structure and goals of Physics Expert Group activities are briefly described.

Section 2.2 discusses inductive operation scenario and sensitivity analysis on effects of sawtooth, operation boundaries, impurity, density and temperature profile, ion heating and degradation near the Greenwald density. Section 2.3 presents the possibility of high Q (~ 50) and ignition operation with a short pulse heating. Section 2.4 presents recent analysis work on long-pulse and steady-state operation. Section 2.5 discusses the confinement and pedestal database used for projection. Section 2.6 addresses divertor physics. Section 2.7 discusses recent theoretical work on neoclassical tearing mode suppression by ECCD, and Section 2.8 the structure and goals of Physics Expert Group activities.

2.2. Inductive operation scenario of Q=10 and sensitivity analysis

2.2.1. Typical operation scenario

The performance of ELMy H-mode operation in ITER-FEAT is assessed by using 1.5 D transport codes PRETOR[1] and ASTRA[2]. The transport coefficients are normalised in a way that the global confinement time is equal to that given by the scaling law. The confinement enhancement factor (H_H-factor) over ELMy H mode scaling[3] IPB98(y,2) is used.

Figure 2.2-1 shows the time evolution of plasma parameters in a typical operation with the flat top current of 15 MA. The simulation is performed from X-point formation (XPF) to the end of burn (EOB). The average electron density is controlled by pre-programming. During the flat top, 33 MW of NB and 7 MW of RF heating are used and about 400 MW of fusion power is produced (Q = 10). The helium accumulation is calculated for the condition that $\tau_{He}^*/\tau_E = 5$. Argon (Ar) impurity up to 0.12% is seeded to keep the power to the divertor target about 30 MW, which gives less than 5 MW/m^2 on the divertor target. The corresponding effective charge is 1.69 and the helium contribution is about 0.16 with f_{He} = 4.3%. The power across the separatrix is 86 MW. This power and the separatrix density of 0.3 x 10 ^{20} m^{-3} are given to 2-D divertor simulation code (see section 2.6 for details). Ar transport and its radiation are yet to be included in 2D divertor calculation. However, even without Ar radiation in the divertor plasma, the maximum heat load on the target is estimated to be 8 MW/m^2. Carbon impurity level at the separatrix is only 0.19 % from 2D divertor calculations, which is negligible compared with the effect of Ar in PRETOR. Recent experimental results suggest that wall impurity sources are as important as divertor sources. Therefore 2D divertor calculations provide an underestimate of impurity contamination. 2 % of beryllium is assumed in PRETOR as impurity from the wall. The helium level is also

[1] D. Boucher, *et. al.*, in Proc. 16h IAEA Fusion Energy Conference, Montreal, 1996 (IAEA,Vienna, 1997) 945.
[2] G. V. Pereverzev, *et. al.*, IPP 5/42 (1991).
[3] ITER Physics Basis, Nucl. Fusion 39 (1999) 2137.

estimated to be much lower with the divertor code than with PRETOR. On this point, the PRETOR results give a conservative estimate. Efforts to improve consistency or resolve inconsistency of the analysis between PRETOR and 2-D divertor code is underway.

Figure 2.2-2 shows the detailed time trace in the starting phase. Plasma heating starts just after the current flat top. At this time, the electron density should be small enough to reduce the threshold power for H-mode transition and large enough to avoid shine through of neutral beams. In this case, NBI heating starts at 100s when $n_e = 4\times10^{19}/m^3$. In the simulation, H-mode transition occurs at 110s, when the second NB is injected.

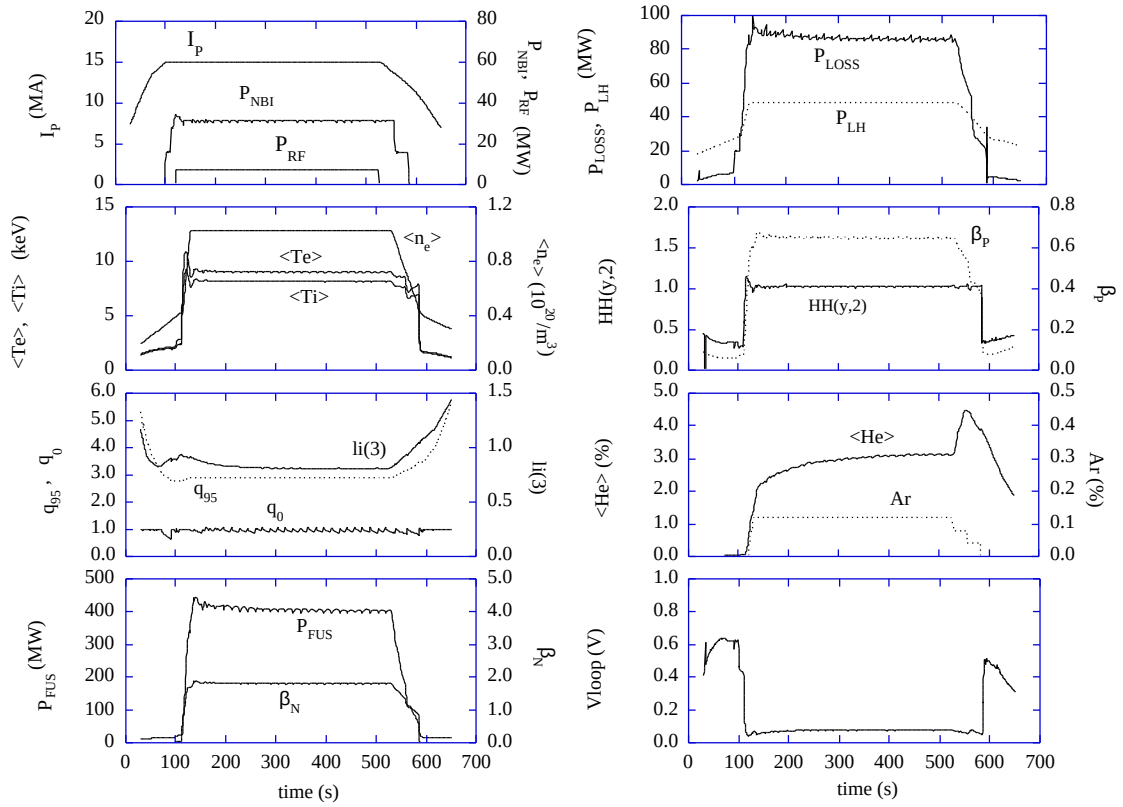

Figure 2.2-1: Time evolution of plasma parameters for 400MW operation without pre-heating during the current ramp up

In this simulation, the outermost flux surface is fixed during the simulation and the full size plasma is studied, and 2-D equilibrium is calculated consistently with the pressure change. The simulation for the growing phase to the full-size plasma, including the X-point formation, is done by using the DINA code[4] with a simplified transport model. The PF-coil system is consistent with the whole phase of the plasma operation.

The requirement for plasma shut down in ITER-FEAT is eased since the transition to L-mode can be easily achieved by switching off the auxiliary heating power. The threshold power, however, decreases when the electron density is reduced, which is also necessary to decrease the fusion power. In the simulation, a threshold power reduction by 50% for the H-L transition is implemented to be conservative. The transition to L-mode occurs at 580s, when all the heating power is switched off in this case.

[4] R.R. Khayrutdinov, V.E. Lukash, J. Comp. Physics 109 (1993) 193.

The loop voltage at the flat top is about 75mV and the burn time is estimated to 400s when the available flux is 30Vs. To prolong the operation pulse length, pre-heating during current ramp up can be used. In this case, 5 to 10 Vs is saved and the burn time is ~ 500 s.

Figure 2.2-3 shows the profiles of plasma parameters at the flat top. Here, a flat density profile is assumed for the reference scenario, to be conservative. Temperature profile is calculated by the RLWB energy transport model[5] and the edge pedestal is created by reducing χ in the region r/a>0.9. Helium accumulation level at the magnetic axis is about 4.2% and Z_{eff} at the axis is 1.69. The fraction of bootstrap current is about 15%. Main physics parameters at the flat top are summarised in Table 2.2-1. All major parameters such as beta, n_e/n_{GW}, divertor heat load, τ_{He}^*/τ_E and Z_{eff} are in a reasonable range.

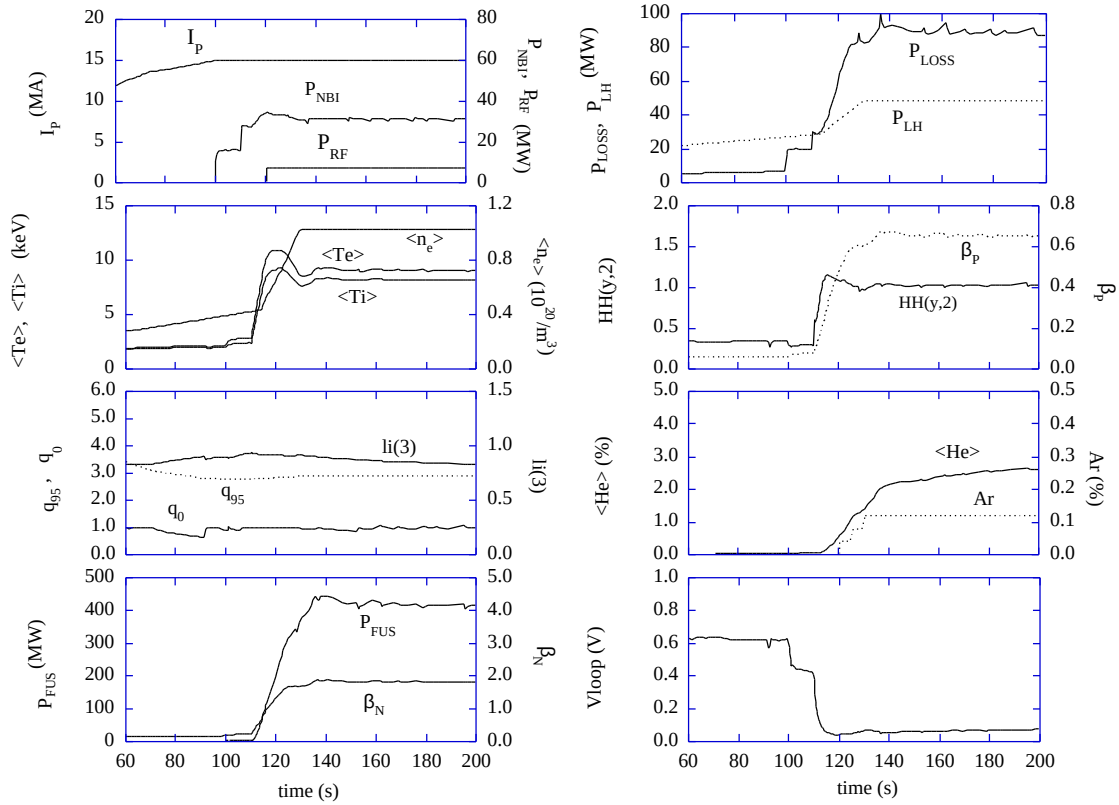

Figure 2.2-2: Time evolution of plasma parameters for 400MW operation (start-up)

[5] D. Boucher and P.-H. Rebut, in Proc. IAEA TCM on Advances in Simulations of Modeling of Thermonuclear Plasmas, 1992, IAEA, Vienna (1993) 142.

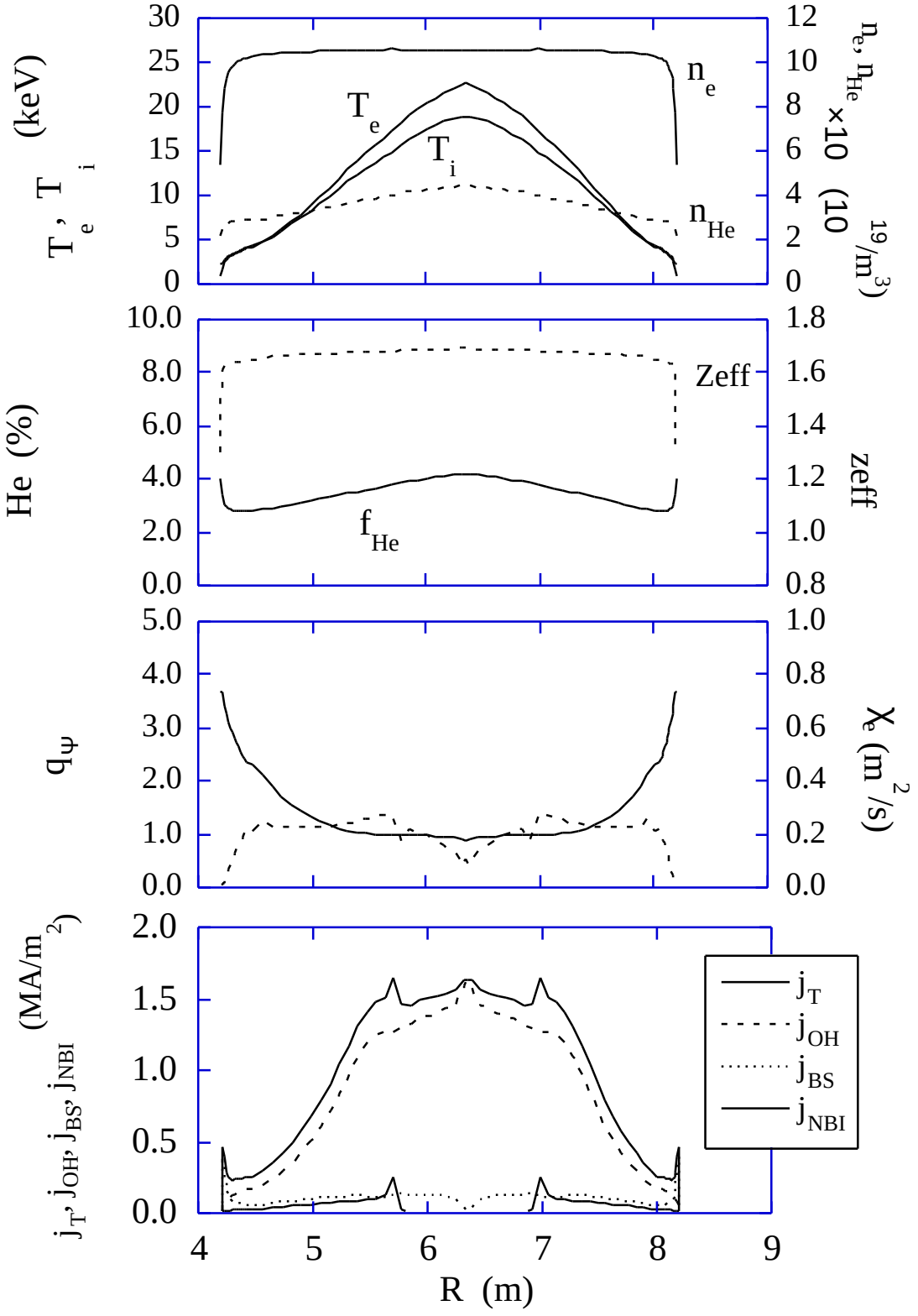

Figure 2.2-3: Profiles of plasma parameters. Here, P_{FUS} = 400 MW, P_{NBI} / P_{RF} = 33 MW / 7 MW and $H_H(y,2)$ = 1.0, respectively

Table 2.2-1 Parameters of ITER-FEAT for typical inductive operation scenario

Parameter		
R/a	(m/m)	6.2/2.0
Volume	(m^3)	815
Surface	(m^2)	673
Sep. length	(m)	18.0
$S_{cross\text{-}sect.}$	(m^2)	21.9
B_T	(T)	5.3
I_P	(MA)	15.0
κ_x/δ_x		1.84/0.5
κ_{95}/δ_{95}		1.7/0.3
$l_i(3)$		0.82
V_{loop}	(mV)	75
q_{95}		3
β_N		1.81
$<n_e>$	($10^{19}/m^3$)	10.2
n_e/n_{GW}		0.85
$<T_e>$	(keV)	9.1
$<T_i>$	(keV)	8.2
$<\beta_T>$	(%)	2.6
β_p		0.65
P_α	(MW)	80
$P_{RF}+P_{NB}$	(MW)	7+33

Parameter		
P_{OH}	(MW)	1
P_{TOT}	(MW)	121
P_{BRM}	(MW)	22
P_{SYN}	(MW)	7
P_{LINE}	(MW)	17
P_{RAD}	(MW)	46
P_{FUS}	(MW)	400
P_{LOSS}/P_{LH}		86/48
$n_{e,sep}$	($10^{19}/m^3$)	3
q_{target}	(MW/m^2)	8
Q		10
τ_E	(s)	3.7
W_{th}	(MJ)	323
W_{fast}	(MJ)	31
$H_{H\text{-}IPB\ 98(y,2)}$		1.0
τ_{He}^*/τ_E		5.0
$Z_{eff,axis}$		1.69
$f_{He,\ axis}$	(%)	4.3
$f_{Be,\ axis}$	(%)	2.0
$f_{C,\ axis}$	(%)	0.0
$f_{Ar,\ axis}$	(%)	0.12

2.2.2. Effect of Sawteeth

The PRETOR code is also used to evaluate the effects of sawteeth. In order to model the effects of the internal magnetic reconnection empirically, the temperature and pressure profiles within a mixing radius determined by the location of q = 1 surfaces are flattened when the perturbed magnetic energy reaches the threshold value. The present model is based on magnetic turbulence[6] and the stabilizing effect due to fast alpha particles and trapped ions are included.

Figure 2.2-4 shows the detailed time trace of plasma parameters at the current flat top. Here, Te(0), Ti(0), q(0), P_α, P_{IN} and P_{FUS} denote the electron and ion temperatures, safety factor at the magnetic axis, alpha heating power, power across the separatrix and fusion power, respectively. By the present sawtooth model, the predicted sawtooth period is about 15s for full reconnection. A significant central temperature change is observed but the fusion power change at the crash is about 3%. The alpha heating power increases at the crash since the slowing down time of fast alpha particles becomes short when they are ejected to the peripheral region.

Figure 2.2-5 shows the profiles just before and after the sawtooth crash. In the present model, the inversion radius is relatively large (~ 0.6 × r/a). When the crash occurs, the power to the

[6] D. Boucher and P.-H. Rebut, in Proc. IAEA TCM on Advances in Simulations of Modeling of Thermonuclear Plasmas, 1992, IAEA, Vienna (1993) 142.

SOL (P_{IN}) increases slightly due to the increase of alpha power (2MW in this case) and the formation of a steep temperature gradient. This effect, however, does not cause any severe impact on the first wall load, nor divertor target heat load.

The sawtooth prediction involves many uncertainties, but there are experimental and theoretical bases for controlling the sawtooth period by ECCD or ICH. The goal in ITER is to keep the sawtooth period short, to prevent problems such as impurity accumulation in the core and input to NTM seed islands.

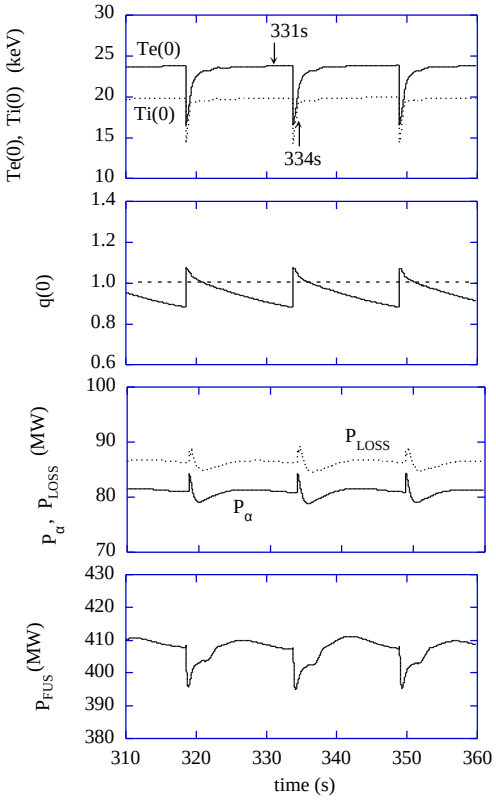

Figure 2.2-4 Time evolution of plasma after the sawtooth crash

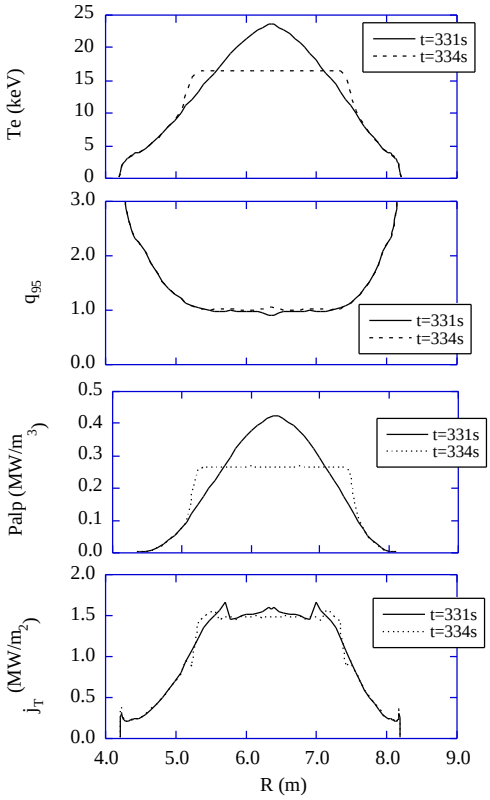

Figure 2.2-5 Plasma profiles before and parameters during flat top

2.2.3. Operation Boundaries

If the electron density is increased close to the Greenwald density n_{GW}, the fusion power increases to 580MW at I_P = 15 MA and $H_H(y,2)$ = 1.0. In this case, the argon impurity should be increased to 0.15% to keep the power flux to the divertor region ≤ 30 MW and Z_{eff} goes up to 1.78. The normalised beta β_N increases to 2.2. Neoclassical tearing modes (NTM) may limit the achievable β_N and cause a degradation of confinement time. Control and suppression of NTMs by ECCD is planned to assure operation of the device at β_N = 2.2. Simulation predicts that NTMs with m/n = 3/2 and 2/1 could be stabilised by 20 MW of ECCD power[7]. Requirements for fuelling, such as the high field side pellet injection will be studied.

[7] G. Saibene, *et. al*., 25th EPS Conference on Controlled Fusion and Plasma Physics, Praha (1998).

The operation would start from relatively low density, e.g. $n_e \sim 0.7 \times n_{GW}$. In this case, the fusion power is about 260 MW at $H_H(y,2) = 1.0$. Figure 2.2-6 shows the time evolution for these cases, with the parameters at the important moments summarised in Table 2.2-2. The poloidal field coil system is designed to cover these operation scenarios.

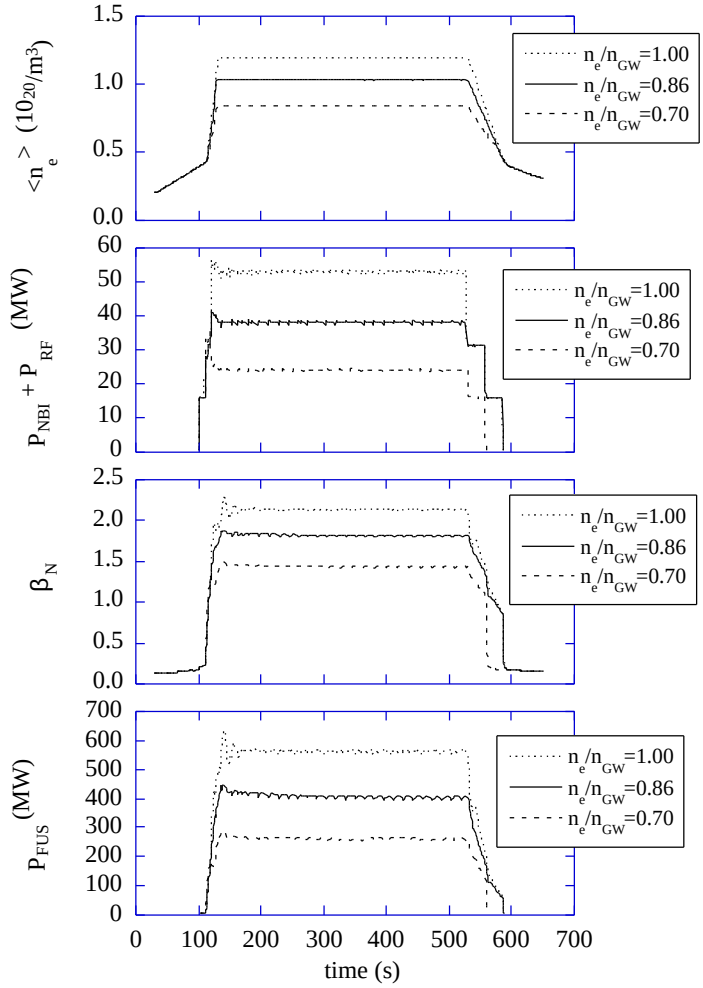

Figure 2.2-6 Time history for various electron density. Here, $H_H = 1.0$ and $Q = 10$

Table 2.2-2 Range of plasma parameters for inductive 15MA, Q = 10 scenario without heating during I_p ramp-up

phase	XPF	SOF/H	SOB	EOB	EOC
t, s	30	100	130	530	590
I_p, MA	7.5	15	15	15	12
q_{95}	5.3	3.0	3.0	3.0	3.0
q_0	1.0	1.0	1.0	1.0	1.0
nom. $<n_{e,20}>$	0.2	0.4	1.02	1.02	0.5
min. $<n_{e,20}>$	↑	↑	0.84	0.84	↑
max. $<n_{e,20}>$	↑	↑	1.20	1.20	↑
nom. n_e/n_{GW}	0.20	0.40	0.85	0.85	0.43
min. n_e/n_{GW}	↑	↑	0.70	0.70	↑
max. n_e/n_{GW}	↑	↑	1.00	1.00	↑
nom. P_{fusion}	0	0	400	400	0
min. P_{fusion}	↑	↑	260	260	↑
max. P_{fusion}	↑	↑	580	580	↑
nom. P_{aux}, MW	0	0	40	40	0
min. P_{aux}, MW	↑	↑	26	26	0
max. P_{aux}, MW	↑	↑	60	60	0
nom. $Z_{eff,\ axis}$	1.3	1.3	1.69	1.69	1.4
min. $Z_{eff,\ axis}$	↑	↑	1.57	1.57	↑
max. $Z_{eff,\ axis}$	↑	↑	1.78	1.78	↑
nom. β_p	0.1	0.05	0.65	0.65	0.1
min. β_p	↑	↑	0.52	0.52	↑
max. β_p	↑	↑	0.79	0.79	↑
nom. β_N	0.1	0.2	1.81	1.81	0.2
min. β_N	↑	↑	1.45	1.45	↑
max. β_N	↑	↑	2.20	2.20	↑

*1 Minimum fusion power is defined by good ELMy-H mode ($P_{IN}/P_{LH} \geq 1.3$) and maximum fusion power by $n_e/n_{GW} \leq 1$.
*2 Burn time is calculated for nominal operation case ($V_{loop} = 75$mV).
*3 Burn time can be prolonged by heating during I_P ramp-up.

2.2.4. Impurity Effect

In surveys of operation scenarios of ITER-FEAT, 2% of beryllium is assumed as a main impurity, and helium accumulation is calculated for the condition that $\tau_{He}^*/\tau_E = 5$. The assumption of $\tau_{He}^*/\tau_E = 5$ is reasonable for ELMy H mode plasmas. In addition, argon (Ar) impurity up to 0.2% or carbon impurity up to 1.2% is considered. In this case, the corresponding effective charge, Z_{eff}, is 1.4 to 1.8.

Figures 2.2-7 and 2.2-8 show the plasma parameters with various impurity contents when the fusion power P_{FUS} = 400 MW, fusion gain Q = 10 and $H_H(y,2) = 1.0$. In the simulation, we assume $\tau_{He}^*/\tau_E = 5$.

When argon impurity is seeded, the line radiation increases significantly, while the increase of the required operation density is small. This means that the operation point is robust and the only effect is decrease of burn time due to the increase of loop voltage. In the case of carbon, the line radiation power is small. The increase of the operation density, however, is larger than that for argon case, and the resultant radiation loss power including bremsstrahlung loss power is almost same level as argon case.

The effective charge Z_{eff} in the present confinement database is shown in Figure 2.2-9. Here, the horizontal axis represents the scaling formula

$$Z_{Scaling} = 1 + 7 \times \frac{P_{RAD}(MW)}{n_{e20}{}^2 S_P\,(m^2)}$$

where P_{RAD} is the radiation power, n_{e20} is electron density in 10^{20} m^{-3}, and S_p is the plasma surface area. If the data for similar conditions with ITER-FEAT ($\kappa > 1.4$, $q_{95} < 3.5$, $n_e/n_{GW} > 0.65$, $P_{RAD}/P < 0.5$) are selected, $1 < Z_{eff} < 2.1$ as is shown in Figure 2.2-10. In the figure, the symbol (+) denotes JET data. This figure means that Z_{eff} for high density plasmas with a Be first wall is relatively small and close to assumptions used in this report.

To summarise, the requirement from performance is that Z_{eff} should be smaller than 2.0. On the other hand, radiative cooling is such that the peak divertor heat load is lower than 8 MW/m^2. According to calculations of divertor transport described in section 2.6, the peak power load can be lowered to 8 MW/m^2 at a separatrix density of 3.2×10^{19} m^{-3}. At the same time Z_{eff} and helium concentration can remain at low values controlled by the divertor operation. These calculations suggest that the ITER FEAT divertor can exhaust heat and particles efficiently. However, this estimate is probably underestimating the impurity influx since it neglects the impurity flux from the first wall. Presently PRETOR is assuming 2 % of beryllium and helium concentrations, higher than 2D divertor calculation (4.3 % vs. 1.2 %), to be conservative.

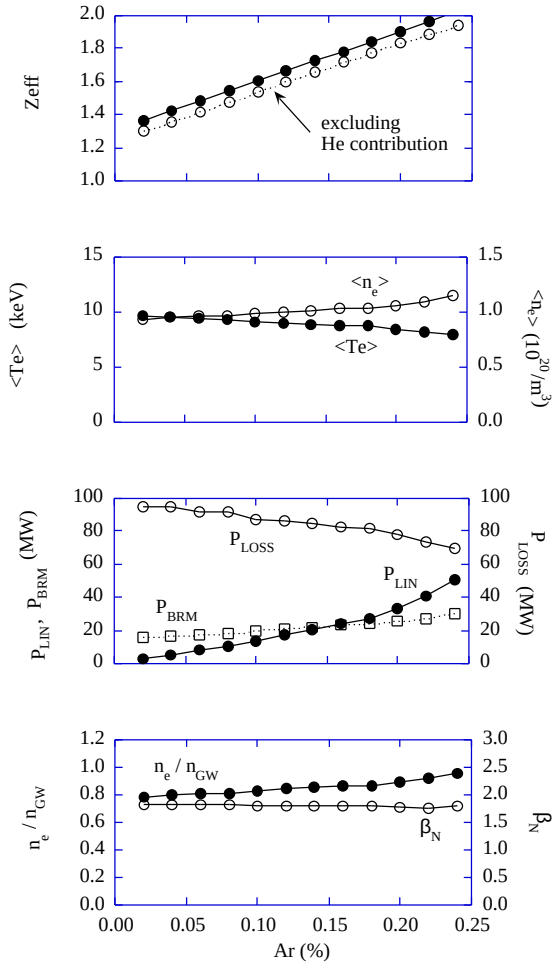

Figure 2.2-7 Plasma parameters for various Ar fractions. Here, Q=10, H_H=1 and P_{FUS}=400MW

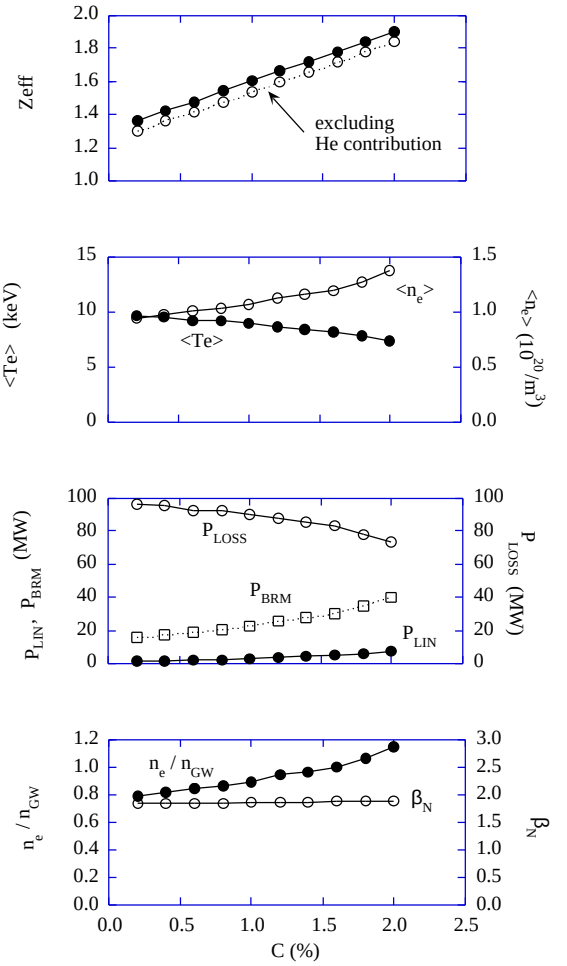

Figure 2.2-8 Plasma parameters for various C fractions. Here, Q=10, H_H=1 and P_{FUS}=400MW

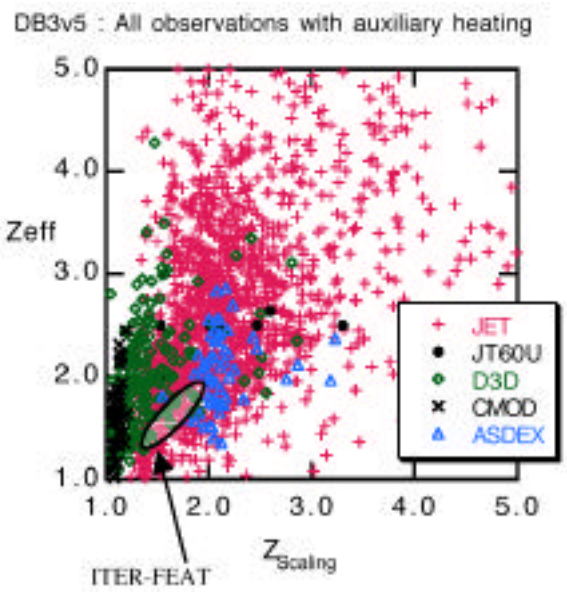

Figure 2.2-9 Z_{eff} for all shots in database DB3v5

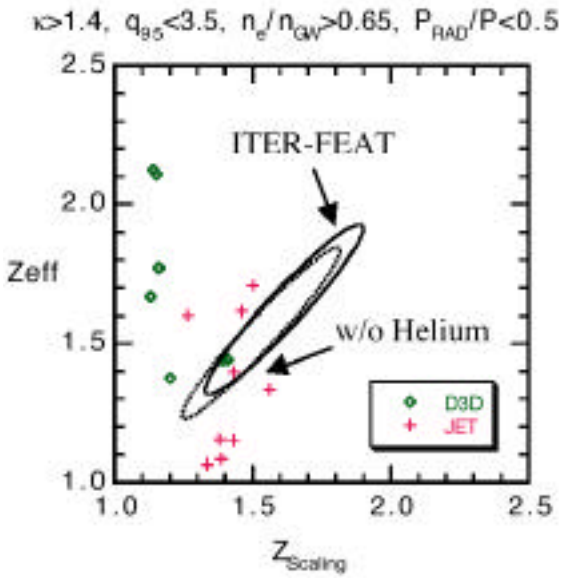

Figure 2.2-10 Z_{eff} for shots with κ>1.4, q_{95}<3.5, n_e/n_{GW}>0.65,P_{RAD}/P<0.5

2.2.5. Density Profile Effect

In the reference scenario, a flat density profile is assumed. In general, peaked density profiles tend to produce larger fusion power for the same average density. Operation with peaked density profile due to the pinch effect has been examined using the PRETOR code. Figure 2.2-11 shows the density profiles when a pinch term proportional to the thermal diffusivity and to the magnetic shear is included with a different pinch coefficient V_p. The pinch effect is not significant in the core region (r/a < 0.5) where the shear is small. Figure 2.2-12 shows the fusion power for various pinch coefficients. Here, the ratio n_e/n_{GW} of average electron density to Greenwald density is fixed to 0.85.

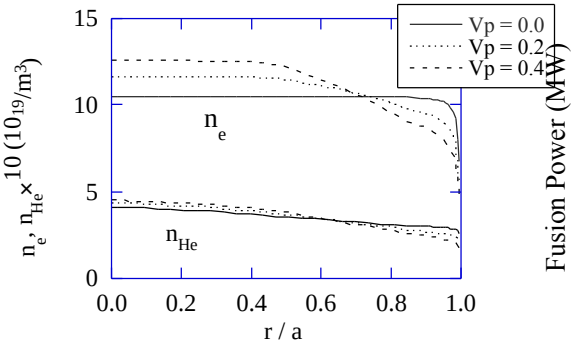

Figure 2.2-11 Density profiles for various pinch coefficients V_p (n_e / n_{GW} = 0.85)

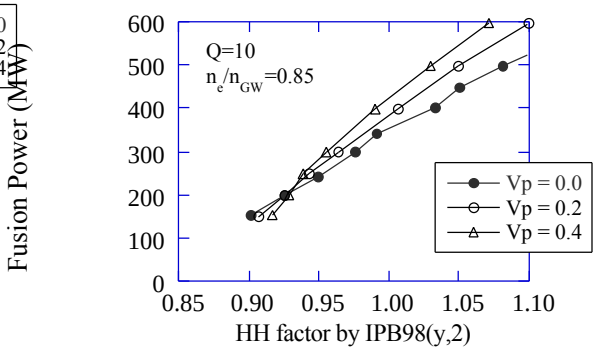

Figure 2.2-12 Dependence of fusion power on H_H factor for the pinch coefficients shown in Figure 2.2-11

Significantly higher fusion power is available in the nominal to high H_H-factor region, while the margin below 1.0 in H_H-factor is decreased from 10 to 8 % since the temperature decreases with the increase of density. Helium accumulation due to the pinch effect also degrades the performance. Deep fuelling by pellet injection from the high field side will be studied.

2.2.6. Ion Heating Effect

Strong ion heating by ICH is also favourable for the improvement of the confinement margin. Figure 2.2-13 shows the relation between the H_H-factor and fusion power for different ion heating fractions $P_I/(P_I + P_E)$ from PRETOR analysis. Here, heating power $P_I + P_E$ is adjusted to Q = 10 with $n_e/ n_{GW} = 0.85$. Fusion power increases through the H_H range, and the lower H_H margin is improved from 10% to 12%. ICH power alone of 20MW would allow a fusion power of 200 - 300 MW.

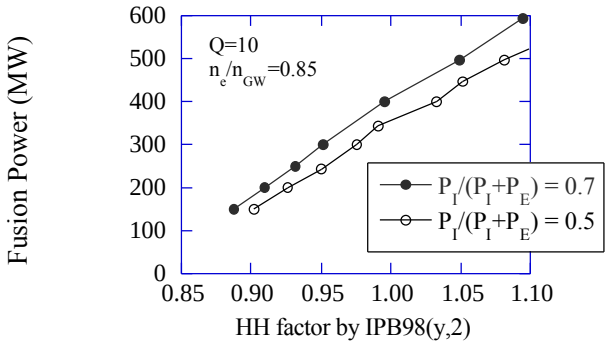

Figure 2.2-13 Dependence of Fusion Power on H_H Factor for Various Ion Heating Fractions.

2.2.7. Temperature Profile Effect

In this section, operation domains for various temperature profiles calculated by a simple 0-D code are presented. A parabolic temperature profile $T(x) = T(0) (1-x^2)^{AT}$ is assumed with a parameter AT.

Figures 2.2-14 show the operation domain in H_H-factor and fusion power space when Q = 10. The confinement margin does not change significantly with the change of temperature profile. In higher fusion power region, however, the requirement for the density limit is mitigated and the confinement margin increases when the temperature profile becomes flat (AT decreases). There is no significant difference between the cases with AT = 1.0 and AT = 1.5 when Q = 10.

Figures 2.2-15 show the operation domain in H_H-factor and fusion power space when Q = 50. A similar tendency is seen.

a) AT = 2.0, Q = 10

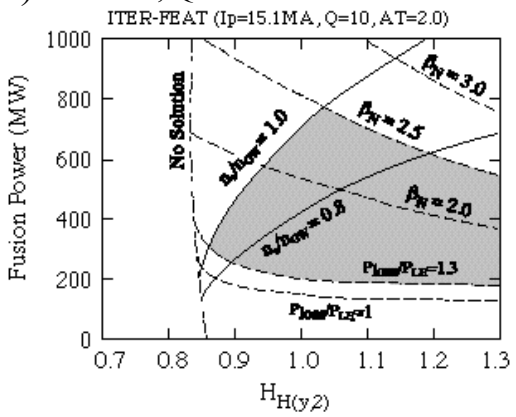

b) AT = 1.5, Q = 10

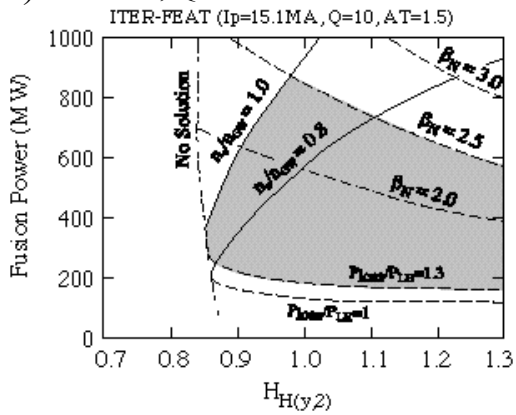

c) AT = 1.0, Q = 10

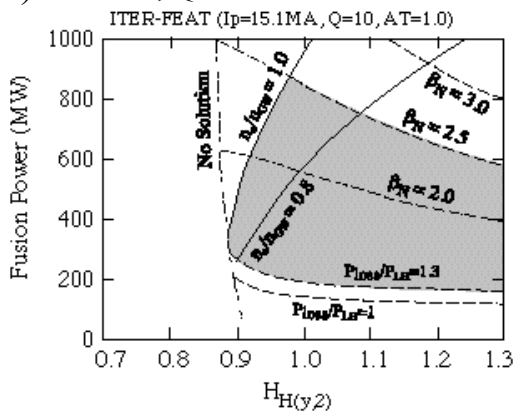

Figure 2.2-14 Operation space of ITER-FEAT when I_P = 15.1 MA and Q = 10 Here, $T(x) = T(0)\,(1-x^2)^{AT}$ a) AT = 2.0, b) AT = 1.5, c) AT = 1.0

a) AT = 2.0, Q = 50

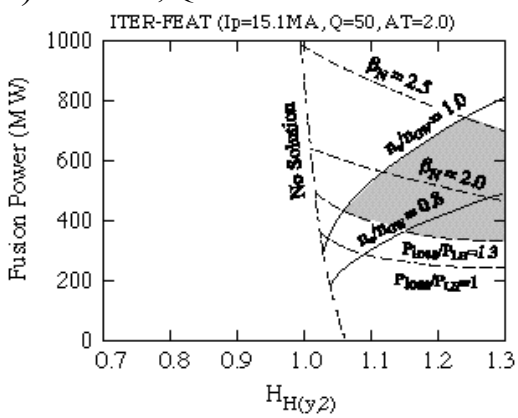

b) AT = 1.5, Q = 50

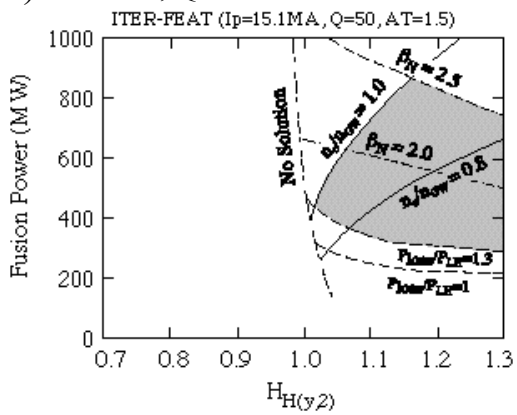

c) AT = 1.0, Q = 50

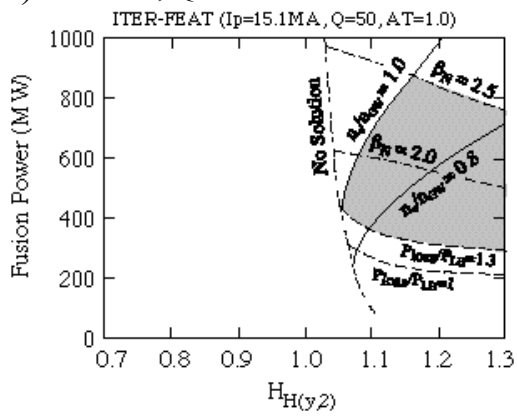

Figure 2.2-15 Operation space of ITER-FEAT when I_P = 15.1 MA and Q = 50 Here, $T(x) = T(0)\,(1-x^2)^{AT}$ a) AT = 2.0, b) AT = 1.5, c) AT = 1.0.

2.2.8. Effect of Degradation near the Greenwald Density

Confinement time degradation near the operation boundary (especially near the density limit) is generally observed in experiments[8]. The deterioration can be mitigated by high triangularity. In JET, for example, with triangularities ~0.35, good confinement is maintained up to 0.8 x n_{GW}. Furthermore, the confinement near the Greenwald density can be improved by high-field-side pellet injection. This area remains an intensive research subject, but one possible explanation can be given by the physics of the edge pedestal, which is described in section 2.5. In this section, the sensitivity of operation performance to confinement saturation is investigated by using a 0-D code. An example of confinement saturation is examined, in which the density dependence of confinement is neglected when the electron density is above $0.8 \times n_{GW}$. This is not a very conservative assumption, but it provides a sensitivity analysis.

Figure 2.2-16 shows the plasma parameters as functions of the normalised density. Here, CASE-A denotes the case with original IPB98(y,2) scaling and CASE-B corresponds to the case including the saturation of confinement time. The confinement time is constant above $0.8 \times n_{GW}$ and the corresponding H_H-factor decreases; therefore the fusion power saturates. In this case, a fusion power of 400 MW can be produced with $n_e \sim 0.95$ x n_{GW}. Here, Q = 10, $\tau_{He}^*/\tau_E = 5$, Be = 2% and Ar = 0.12% to be conservative. (The fraction of Ar could be reduced in high density operation.) The density profile is flat and a temperature profile $T(x) = T(0)(1-x^2)^{AT}$ with AT=2.15 is used.

[8] G. Saibene, *et. al*., 25th EPS Conference on Controlled Fusion and Plasma Physics, Praha (1998).

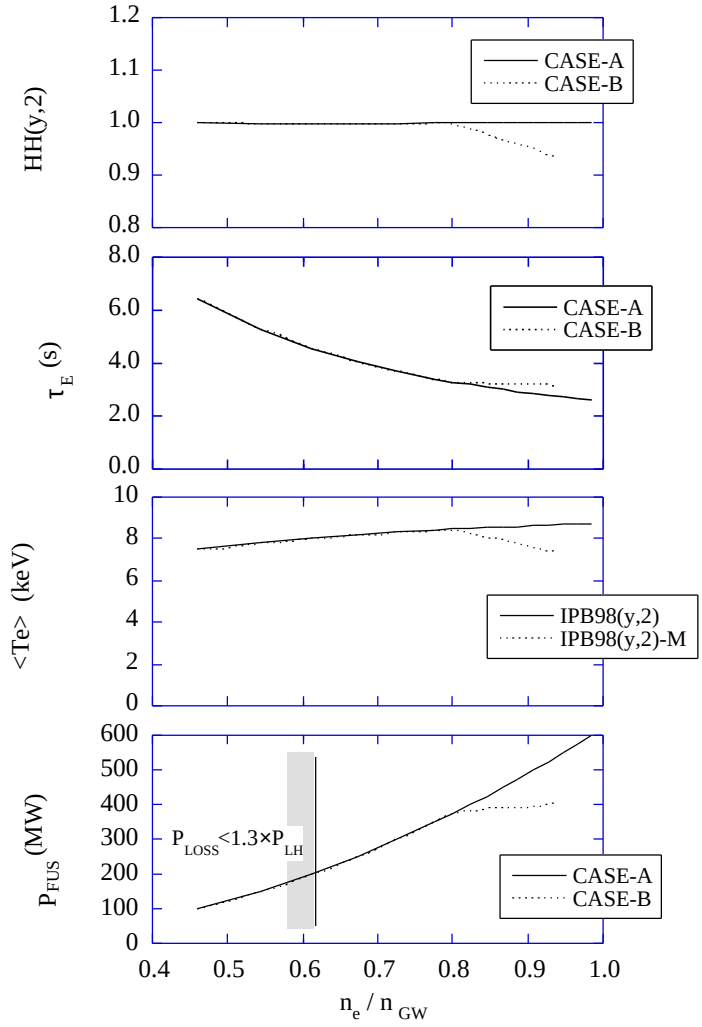

Figure 2.2-16 : Operation parameters as a function of electron density normalised by Greenwald density n_{GW}. Here, Q=10, τ_{He}^*/τ_E =5, Be=2% and Ar=0.12% Density profile is flat and temperature profile $T(x)=T(0)\,(1-x^2)^{AT}$ with AT=2.15. CASE-A : IPB98(y,2) scaling CASE-B : IPB98(y,2) scaling, but no density dependence when $n_e > 0.8 \times n_{GW}$.

2.3. High-Q (~50) Operation and Possibility of Ignition

As described in the ODR[9], high-Q (~50) operation is possible with $H_H = 1.0$ when the plasma current is 17 MA. In this section, the method to achieve such an operation is examined and the possibility of ignition is explored. Here, the current ramp-up and density build-up are not considered for simplicity.

Figure 2.3-1 shows the PRETOR simulation for high-Q operation when the plasma current is 17MA and the electron density is $1.1 \times 10^{20}/m^3$ (~ $0.81 \times n_{GW}$). Helium accumulation is calculated by assuming $\tau_{He}^*/\tau_E = 5$. At the flat top, auxiliary heating power (P_{AUX}) is 10 MW and about 450 MW (Q = 45) of fusion power (P_{FUS}) is produced. In this case, 73 MW of auxiliary heating power is added from 10s to 13.5s to achieve the H-mode transition. Here, P_{LH} is the threshold power for LH-transition and P_{LOSS} is the power across the H-mode edge pedestal. In the early phase of the discharge, thermal instability can be observed. This result implies that ignition is possible by turning off the auxiliary heating power for a short period.

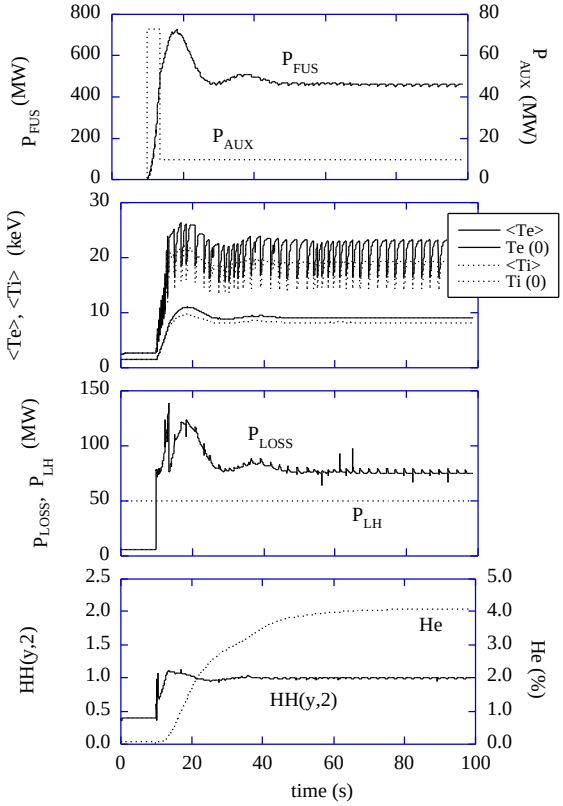

Figure 2.3-1 Time evolution of plasma parameters for transient ignition. Here, I_p=17 MA, $<n_e>=1.1\times10^{20}/m^3$ (n_e/n_{GW}=0.81) and τ_{He}^*/τ_E=5.

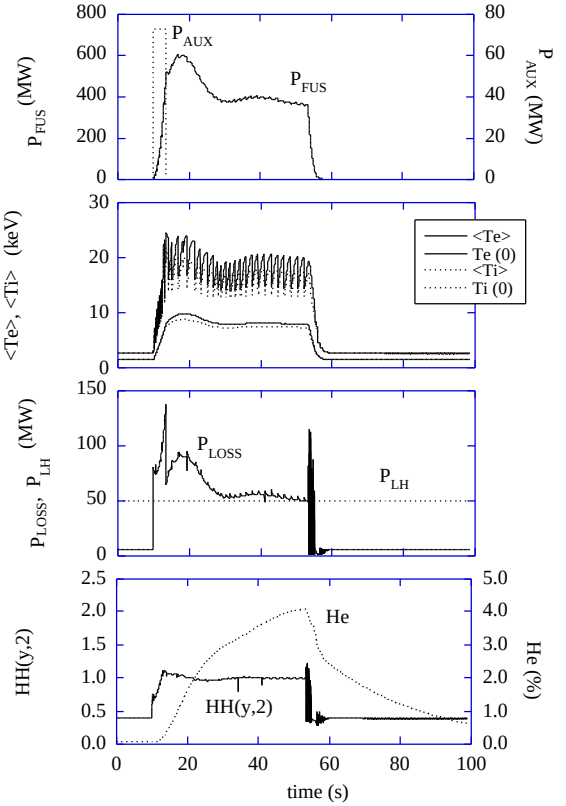

Figure 2.3-2 Time evolution of plasma parameters for high-Q operation. Here, I_p=17 MA, $<n_e>=1.1\times10^{20}/m^3$ (n_e/n_{GW}=0.81) and τ_{He}^*/τ_E=5.

Figure 2.3-2 shows the result for ignition. When the heating power is turned off at t = 13.5s, the helium level is very small and the self-heating power is large enough to stay in H-mode.

[9] Technical Basis for the ITER-FEAT Outline Design G A0 RI 2 00-01-18 R1.0.

Other assumptions are the same as Figure 2.3-1. In this case, the ignition state is maintained for about 40s and the L-mode transition occurs at t = 55 s. In this study, hysteresis for HL-transition is not assumed and dW/dt is not included in P_{LOSS} to be conservative.

Figure 2.3-3 shows the results for various helium accumulation levels. The ignition operation continues in steady state when $\tau_{He}^*/\tau_E \leq 4$. It is seen that a transient ignition experiment can be performed even for lower pumping efficiency ($\tau_{He}^*/\tau_E = 7$).

Figure 2.3-4 shows the results when the H_H-factor is improved by 10%. In this case, $\tau_{He}^*/\tau_E = 5$ is assumed but other assumptions are the same as previous figures. When $H_H = 1.1$, the fusion power increases by about 25% and the ignition continues as long as PF-coil flux (more than 100 s) is available even when $\tau_{He}^*/\tau_E = 5$.

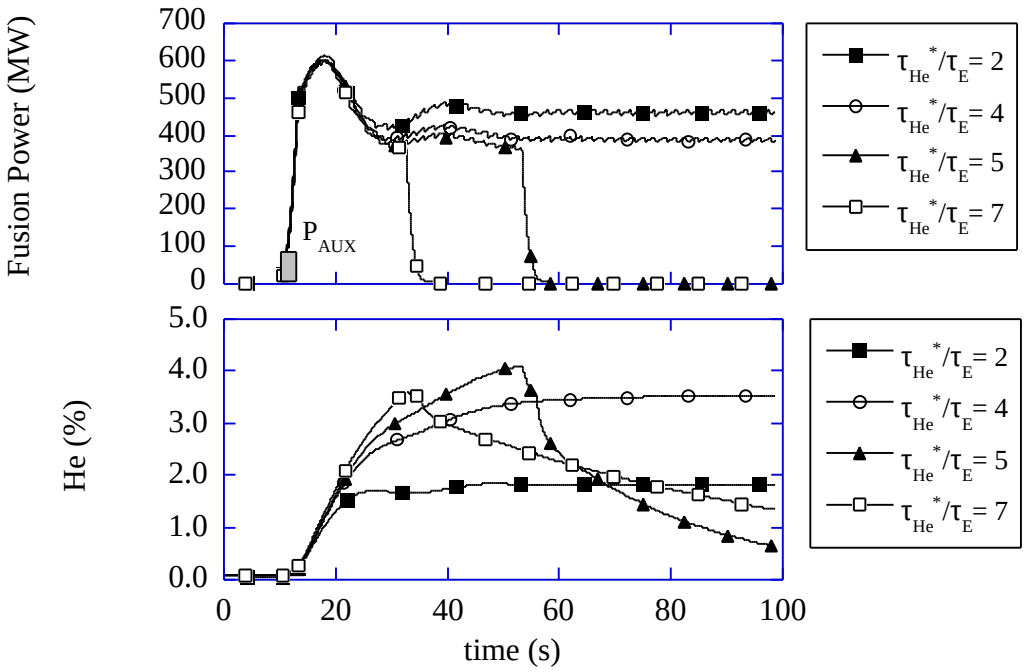

Figure 2.3-3: Time traces of fusion power and helium fraction for various τ_{He} assumptions. Here, I_p = 17 MA, $<n_{e20}>$ = 1.1 (n_e/n_{GW} = 0.81) and P_{AUX} = 73 MW from t = 10s to t = 13.5s. L-mode transition occurs when the loss power P_{LOSS} is less than P_{LH}

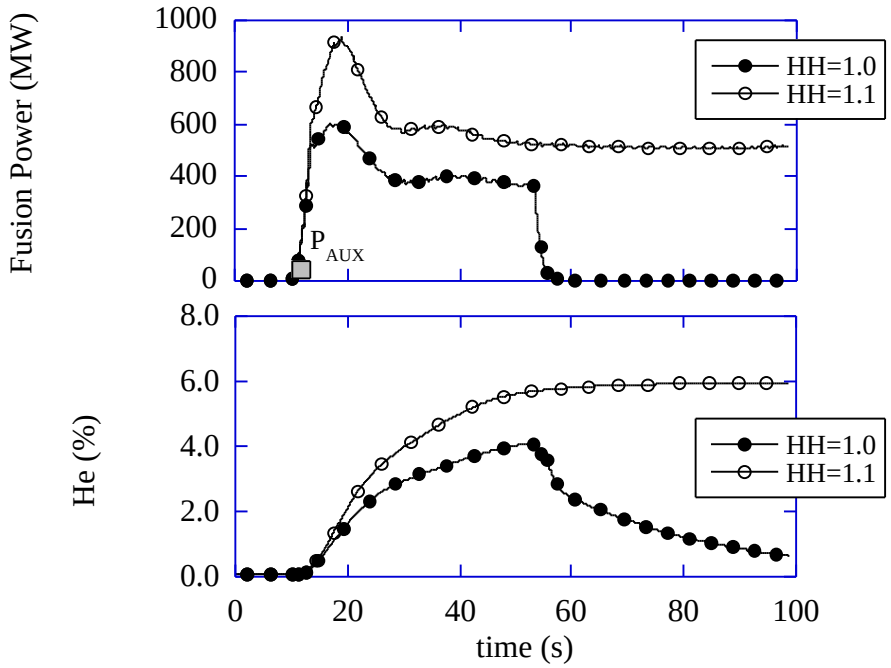

Figure 2.3-4: Time traces of fusion power and helium fraction when H_H-factor is improved. Here, $\tau_{He*}/\tau_E = 5$, $I_p = 17$ MA, $\langle n_{e20} \rangle = 1.1$ ($n_e/n_{GW} = 0.81$) and $P_{AUX} = 73$ MW from t = 10s to t = 13.5s. L-mode transition occurs when P_{LOSS} is less than P_{LH}.

2.4. Long Pulse and Steady-state Operations

2.4.1. Long Pulse Operations

A hybrid mode of operation, in which a substantial fraction of the plasma current is driven by external CD power and the bootstrap current, is a promising route towards the establishment of true steady-state modes of operation. Table 2.4-1 shows two scenarios of hybrid operation, with plasma currents of 13.5 MA. These scenarios satisfy Q ~ 5 and burn time ~ 1000 s at H_H = 1. Both scenarios use the full size plasmas (R/a = 6.2 m/2.0 m). Scenario 1, with a fusion power of 400 MW, is compatible with the auxiliary heating power available in the initial phase (73 MW), while scenario 2, with a fusion power of 500 MW, requires a total auxiliary heating power of 100 MW. The advantage of high current (13.5 MA) scenario is that the requirements on β_N and density are very modest. These scenarios show that long pulse operation regimes are accessible to ITER-FEAT at a modest requirement, in particular at 400 MW – 1000 s.

Table 2.4-1 PRETOR simulation: Hybrid mode 400/500 MW

	1	2
R (m) / a (m)	6.2 / 2.0	(
κ_{95} / δ_{95}	1.7 / 0.33	(
V_P (m^3)	814	(
B_T (T)	5.3	(
I_P (MA)	13.5	(
q_{95}	3.2	(
$<n_e>$ ($10^{19}m^{-3}$)	9.3	10.0
n / n_{GR}	0.87	0.94
$<T_i>$ (keV)	8.4	8.8
$<T_e>$ (keV)	9.7	10.2
$ß_N$	1.98	2.25
P_{FUS} (MW)	400	500
P_{NBI} (MW)	33	40
P_{RF} (MW)	40	60
$Q = P_{FUS} /(P_{NBI}+P_{RF})$	5.4	5.0
P_{loss} / P_{LH}	115/46	152/48
τ_E (s)	2.70	2.29
He (axis/ave) %	3.6 / 2.6	3.3 / 2.4
Ar (axis) %	0.17	0.20
Z_{eff} (ave)	1.79	1.88
P_{RAD} (MW)	51.9	65.1
β_p	0.79	0.90
l_i (3)	0.93	0.93
I_{CD} / I_P %	25	32
I_{BS} / I_P %	18	21
γ20NBI (A/Wm^2)	0.24	0.23
γ20RF (A/Wm^2)	0.30	(
γ20TOT (A/Wm^2)	0.27	0.28
V_{loop} (mV)	60	**52**
H_H-98 (y2)	1.0	←
τ_α^* / τ_E	5	←
Burn time (s)*	880	1020

2.4.2. Steady-state Operation

Here, the possibility of steady-state operation in ITER-FEAT is examined by using a 1.5-D transport code. In the simple analysis reported in the ODR[10], it was shown that a relatively large H_H-factor is required to achieve steady-state operation with Q = 5, even with a somewhat high efficiency of current drive. In this section, an H_H-factor survey is performed for given current-drive power, and the achievable fusion power (and Q-value) is investigated. The current-drive efficiency of NBI is given by the Mikkelsen-Singer model[11] and the normalised current drive efficiency for RF is fixed to about 0.24×10^{20}A/Wm^2. In this survey, 40 MW of RF power (5 MW on axis and 35 MW in the peripheral region) is used. Two cases (33MW and 60 MW) of NBI power are investigated.

Figure 2.4-2 shows the relation between H_H-factor and the achievable Q-value in non-inductive operation of ITER-FEAT. When the current-drive power is 73 MW (NBI 33 MW and RF 40 MW), the required H_H-factor is about 1.6 to achieve steady-state operation with Q = 5. In this case, $n_e/n_{GW} = 0.7$ and $\beta_N = 3.1$. When the current-drive power is 100 MW (NBI 60 MW and RF 40 MW), the required H_H-factor is about 1.4 to achieve steady-state operation with Q = 5. In this case, $n_e/n_{GW} = 0.65$ and $\beta_N = 3.2$. Further study is needed.

[10] Technical Basis for the Outline Design of ITER-FEAT, G A0 RI 2 00-01-18 R1.0
[11] D. R. Mikkelsen and C. E. Singer, Nucl. Technol. /Fusion 4 (1983) 237.

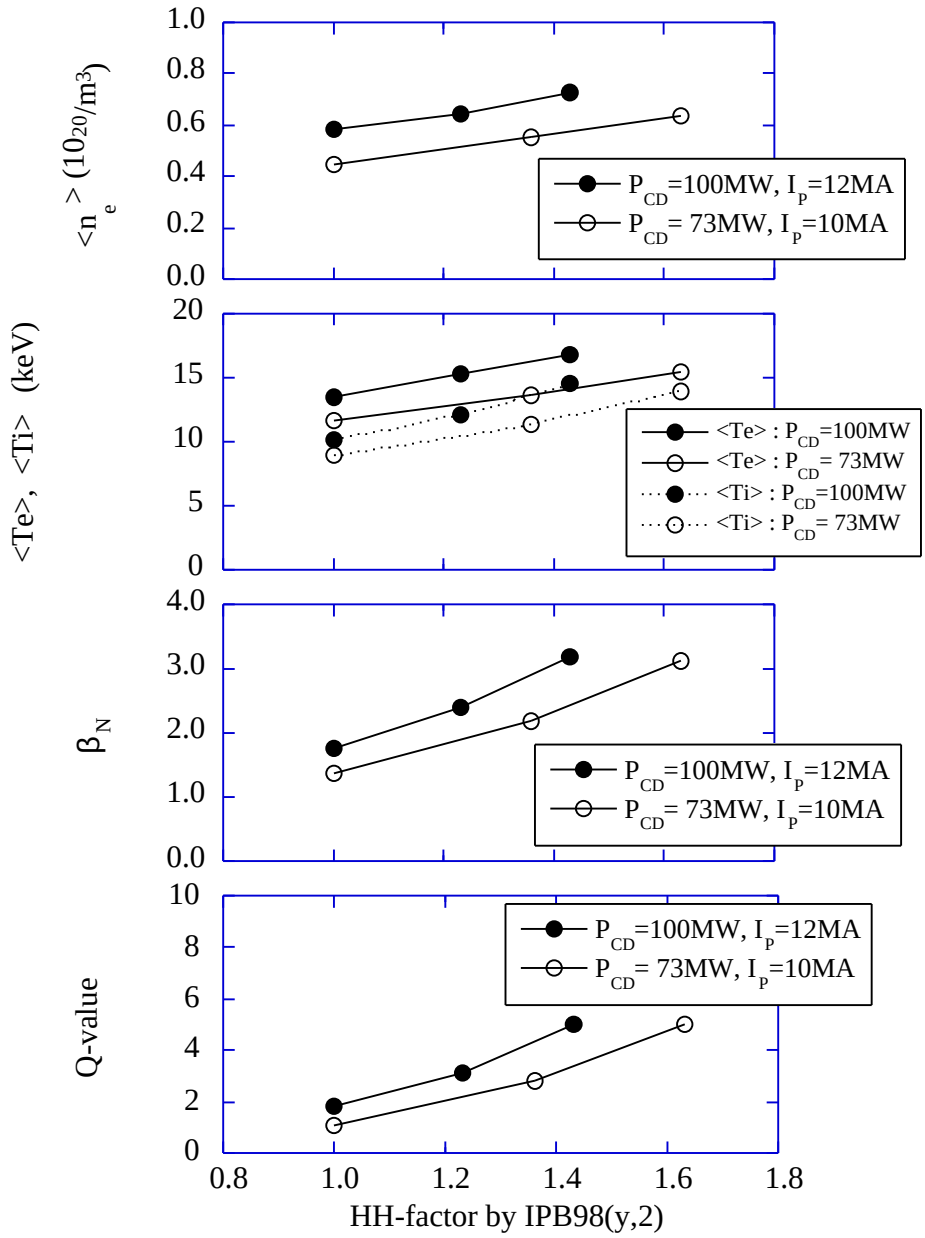

Figure 2.4-2 Steady-state operation parameters of ITER-FEAT.

2.5. Confinement Database

2.5.1. Present ELMy H-mode Confinement Database

For information, the ITER-FEAT reference point is compared with the data from the H-mode confinement database DB3v5[12]. The subset of the database for (y,2) scaling is used. The data represents a cloud of points in multi-dimensional space of different parameters. This cloud is projected onto the planes of $H_H(y,2)$ factor ($H_H(y,2) = \tau_{exp}/\tau_{y,2}$) versus the following parameters:

β_N - normalised beta;
κ_a - elongation calculated through area;
δ_x - triangularity at separatrix;
q_{95} - safety factor;
P/P_{LH} - heating power related to predicted threshold power of L- to H-mode transition;
ν^*- normalised collisionality;
n/n_{GW} - plasma density related to Greenwald density.

The position of the ITER-FEAT reference point is indicated on the figures. All figures with $H_H(y,2)$ versus β_N, κ_a, δ_x, q_{95}, P/P_{LH}, ν^* demonstrate that the ITER-FEAT point lies in the interior of the cloud of experimental points, except for Figure 2.5-7: $H_H(y,2)$ versus n/n_{GW}. The ITER-FEAT reference point lies close to the boundary of the cloud of experimental points on this graph.

All of these graphs indicate that there are many experiments with $H_H(y,2)$ 1 at parameters relevant to ITER-FEAT, but (not evident in the graphs) there are only a few data points having simultaneously parameters relevant to ITER-FEAT and which give $H_H \sim 1$. However, the width of the distribution in H_H against all other parameters is not representative of a probability distribution against random values of the other parameters: distinct physical phenomena are acting, not all of which are identified and understood.

[12] ITER Physics Basis, Nucl. Fus. 39 (1999) 2175

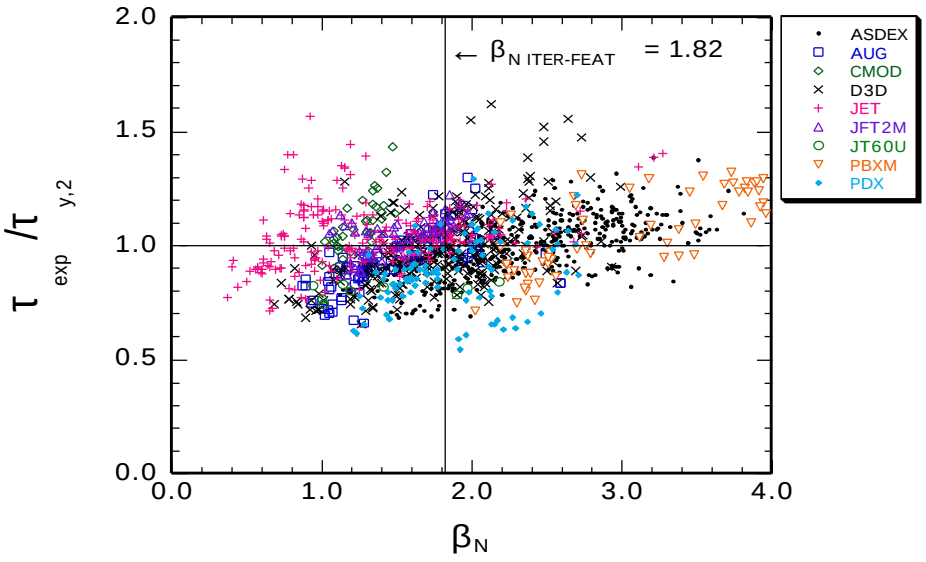

Figure 2.5-1 $H_H(y,2) = \tau_{exp}/\tau_{y,2}$ versus β_N.

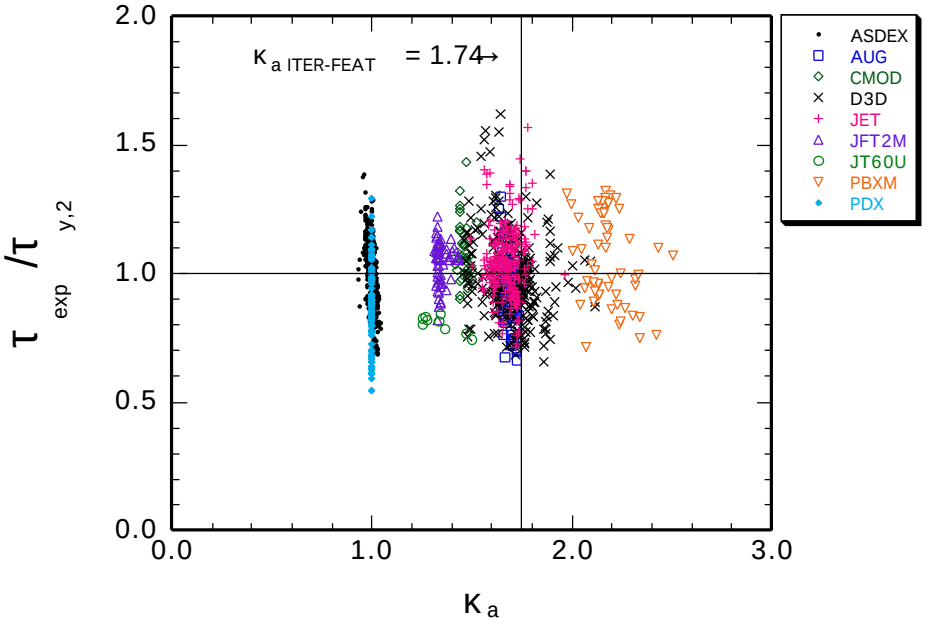

Figure 2.5-2 $H_H(y,2) = \tau_{exp}/\tau_{y,2}$ versus κ_a.

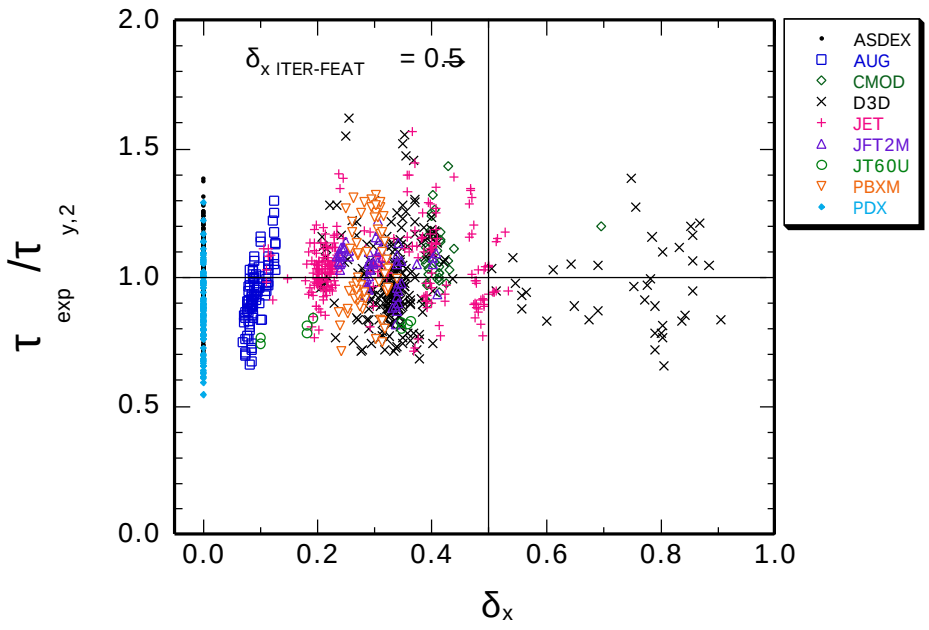

Figure 2.5-3 $H_H(y,2) = \tau_{exp}/\tau_{y,2}$ versus δ_x.

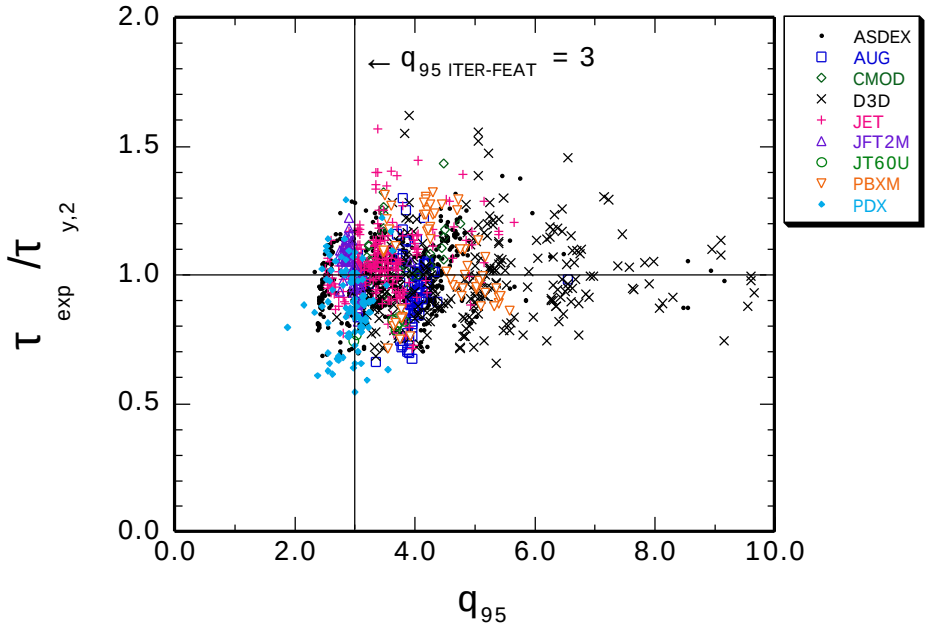

Figure 2.5-4 $H_H(y,2) = \tau_{exp}/\tau_{y,2}$ versus q_{95}.

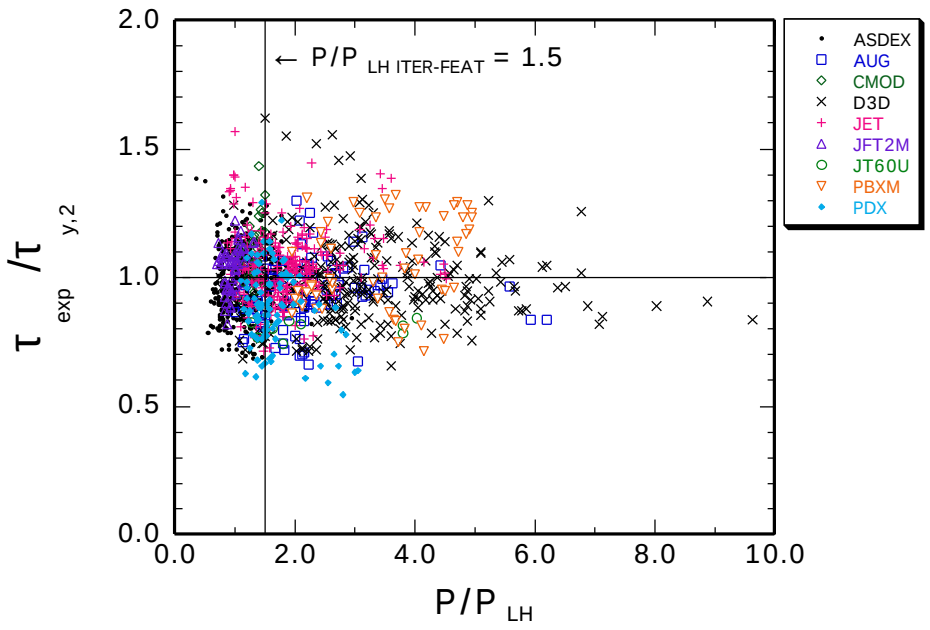

Figure 2.5-5 $H_H(y,2) = \tau_{exp}/\tau_{y,2}$ versus P/P_{LH}.

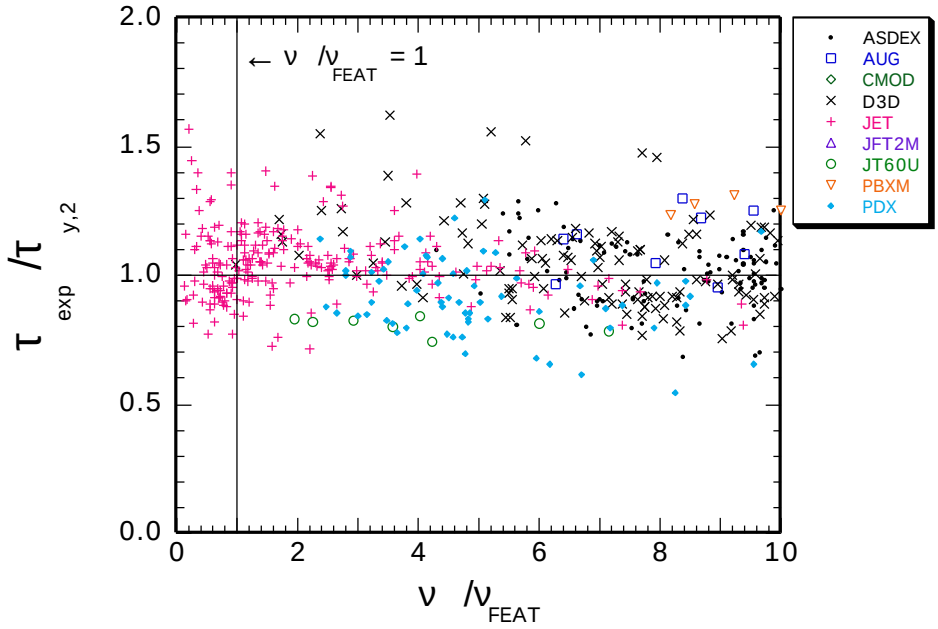

Figure 2.5-6 $H_H(y,2) = \tau_{exp}/\tau_{y,2}$ versus ν^*/ν^*_{FEAT}, points with $\nu^*/\nu^*_{FEAT} > 10$ are omitted.

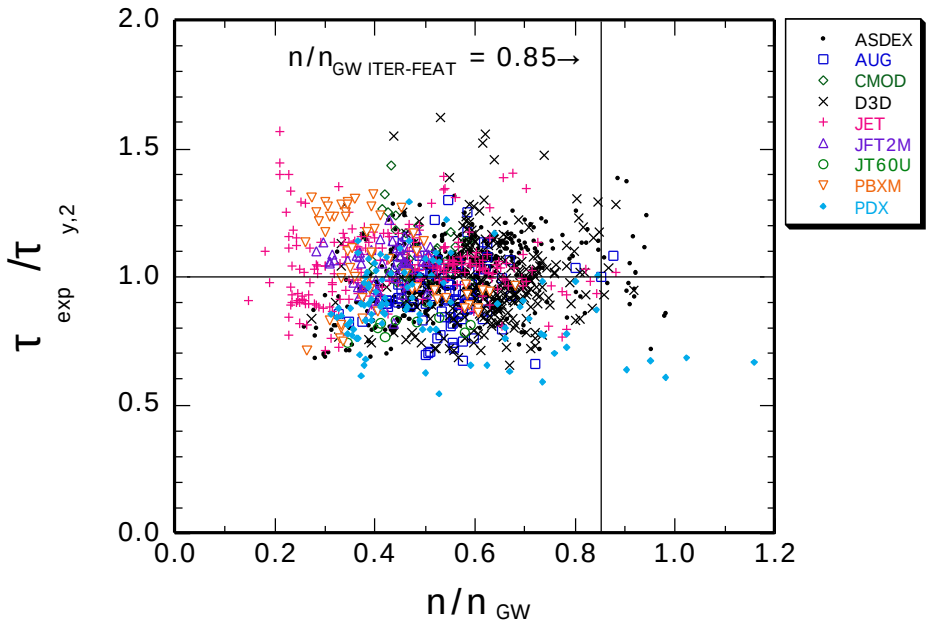

Figure 2.5-7 $H_H(y,2) = \tau_{exp}/\tau_{y,2}$ versus n/n_{GW}.

2.5.2. Necessity of Dimensionless Transport Studies

There are no data for the Dimensionless Transport Study for ITER-FEAT. New experiments in the present tokamaks are required.

2.5.3. Offset non-linear confinement scalings and edge pedestal

During recent years, increasing attention has been paid to development of the physics based on offset non-linear confinement scalings taking account of different transport properties of the core and edge plasmas. This activity is presently in its early stage and suffers mainly from the absence of a reliable model for the edge pedestal parameters. The next section provides one insight into this problem from a very different point of view.

2.5.4. Predictions of ELM Energy Loads and their Control in ITER-FEAT

During recent years a basic understanding of the relation between the H-mode pedestal and the core energy confinement has emerged[13] which allows to understand e.g. the importance of

[13] G. Janeschitz, Yu. Igitkhanov, M. Sugihara et al., 26 the EPS Conference on Contr. Fusion Plasma Physics, Maastricht, (1999) p 1445.
M. Sugihara, Y. Igitkhanov, G. Janeschitz, Pedestal Width Scaling, to be published in Nucl Fusion

high triangularity for good H-mode confinement at densities near the Greenwald density. The choice of relatively high triangularity ($\delta_{95\%} \sim 0.35$) of the ITER-FEAT equilibria is based on this knowledge and on experimental observations[14]. Based on these observations a minimum temperature at the top of the pedestal, is required in order to achieve good H-mode confinement (Figure 2.5-8a, 2.5-8b)[15].

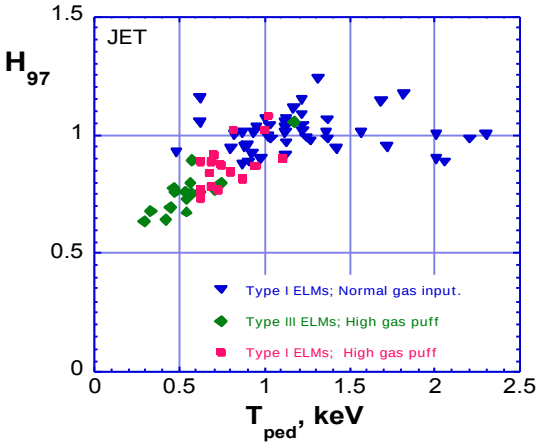

Figure 2.5-8a H-factor normalised to the H97 scaling versus the temperature on top of the pedestal (T_{ped}) for discharges with different gas puff scenarios and ELM types in JET. One can clearly see that the H factor in discharges with low pedestal temperature is proportional to T_{ped} (characteristic for stiff temperature profiles) while it becomes independent of T_{ped} at high pedestal temperatures (non-stiff branch).

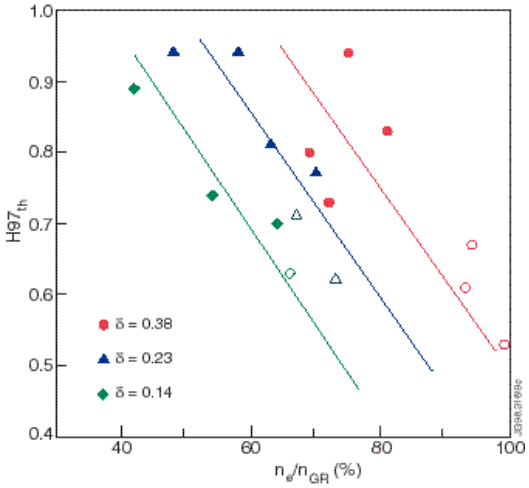

Figure 2.5-8b H-factor versus density normalised to the Greenwald density for JET discharges with different triangularities. From these data it can be clearly seen that at higher triangularity (higher pedestal pressure) the confinement degradation starts at higher density, i.e. the critical T_{ped} of Figure 2.5-8a (TPT) is reached at higher density.

However, the pedestal temperature decreases with increasing density due to the fact that the pedestal width, the maximum pressure gradient in the pedestal (ballooning limited) and thus the pressure on top of the pedestal is more or less constant for a given set of magnetic parameters (I_P, triangularity, etc). This is also true if one varies the heating power, because due to the pressure gradient limit and a more or less constant pedestal width only the ELM frequency increases without changing the average pressure on top of the pedestal when increasing the heat flux through the pedestal. Therefore, if one wants to operate with good confinement at high density a high pedestal pressures and thus high triangularity is needed resulting in a high pedestal energy content. The above considerations explain the degradation of energy confinement at high density and its dependence on triangularity (Figure 2.5-8b). Due to a large pedestal energy content in high triangularity Type I ELM scenarios (high

Kotchenreuter, M., et al, 16th IAEA Fusion Energy Conference, Montreal, Canada, (1996) IAEA-F1-CN-64/D1-5.

[14] G. Saibene, L. D. Horton, R. Sartori, et al., Nucl. Fusion **39** (1999) 1133.
Stober J et al 1999 26th EPS Conference on Controlled Fusion and Plasma Physics, Maastricht, ECA **23J** 1401
O. Gruber, et al., 17th IAEA Fusion Energy Conference, Yokohama, Japan, IAEA-F1-CN-69/OV4/3 (1998).
Y. Kamada, et al., 17th IAEA Fusion Energy Conference, Yokohama, Japan, IAEA-F1-CN-69/CD2/EX9/2 (1998).

[15] G. Janeschitz, Yu. Igitkhanov, M. Sugihara et al., 26 the EPS Conference on Contr. Fusion Plasma Physics, Maastricht, (1999) p 1445.

pedestal pressure) larger energy losses during ELMs can be expected and are in fact observed[16].

A possible model to quantify the pedestal energy content

The importance of high triangularity and thus of a high H-mode pedestal pressure and energy content can be understood by assuming stiff temperature profiles, which are related to Ion Temperature Gradient (ITG) driven turbulence[17]. In fact several machines observe such profile stiffness in their H-mode discharges, albeit, in some cases, only at medium to high densities (e.g. JET (Figure 2.5-8a), JT60U) while other machines are almost always in a stiff temperature regime (e.g. C-mod, ASDEX-UP, DIII-D)[18]. In cases where the stiffness of the temperature profiles disappears (above a certain edge – pedestal temperature) energy transport behaviour very different from ITG turbulence takes over[19] and it is suspected that this transport behaviour is dominated by the electrons (assuming strong energy equipartion, i.e. higher densities). Based on these considerations, it is reasonable to assume that the above-defined TPT is an optimised operation point for good H-mode confinement (optimised for minimum ELM size and good energy confinement). In order to understand how this TPT scales with machine size and with plasma parameters a simple analytical model presented[20] is employed, which is able to explain the change over between stiff and non-stiff temperature profiles on machines in which both branches of confinement behaviour are observed (DIII-D, JET, JT60U). Recently also ASDEX-UP found a change of confinement behaviour (loss of stiffness)[21] at a pedestal temperature predicted by the simple model (Figure 2.5-9a), giving some confidence for predicting a TPT for existing machines as well as for ITER-FEAT.

Applying this model to ITER-FEAT gives a TPT of ~ 3.5 keV (Figure 2.5-9b). While this temperature should be taken to be approximate rather than an accurate number, it is in the same range as the ones predicted to be required for good H-mode confinement by detailed transport code calculation based on ITG models[22]. A similar pedestal temperature for ITER-FEAT at the nominal operation point is predicted by a model for the pedestal width[23] when assuming a pressure gradient in the pedestal close to the ballooning limit.

---

[16] Saibene G. et al, Nuclear Fusion 39, 1133 (1999)

Leonard, A., et al., J. Nucl. Materials **266-269** (1999) 109.

[17] G. Janeschitz, Yu. Igitkhanov, M. Sugihara et al., 26 the EPS Conference on Contr. Fusion Plasma Physics, Maastricht, (1999) p 1445.

Kotchenreuter, M., et al, 16th IAEA Fusion Energy Conference, Montreal, Canada, (1996) IAEA-F1-CN-64/D1-5.

[18] G. Janeschitz, Yu. Igitkhanov, M. Sugihara et al., 26 the EPS Conference on Contr. Fusion Plasma Physics, Maastricht, (1999) p 1445.

M. Sugihara, Y. Igitkhanov, G. Janeschitz, et al., 26 the EPS Conference on Contr. Fusion Plasma Physics, Maastricht, (1999) p1449.

[19] G. Janeschitz, Yu. Igitkhanov, M. Sugihara et al., 26 the EPS Conference on Contr. Fusion Plasma Physics, Maastricht, (1999) p 1445.

[20] G. Janeschitz, Yu. Igitkhanov, M. Sugihara et al., 26 the EPS Conference on Contr. Fusion Plasma Physics, Maastricht, (1999) p 1445.

[21] J. Stober, et.al., 7th IAEA Workshop on H-mode physics and Transport Barriers, Oxford 1999, to be published in PPCF

[22] e.g Kotchenreuter, M., et al, 16th IAEA Fusion Energy Conference, Montreal, Canada, (1996) IAEA-F1-CN-64/D1-5.

[23] M. Sugihara, Y. Igitkhanov, G. Janeschitz, et al., 26 the EPS Conference on Contr. Fusion Plasma Physics, Maastricht, (1999) p1449.

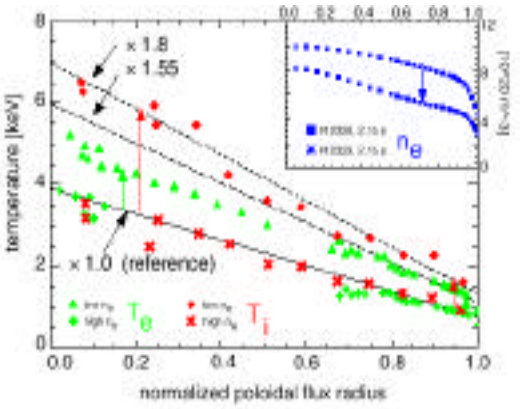

Figure 2.5-9a Electron (green) and ion (red) temperature profiles in ASDEX-UP for two discharges with different density[24]. While at the higher density (low pedestal temperature) both temperature profiles seem to be stiff, the electrons deviate from a stiff behaviour at the lower density (high T_{ped}). This change happens at a TPT predicted by the analytic model[25]. Due to the relatively low density the ions are decoupled from the electrons and continue thus to display a stiff behaviour which would not be the case at higher density, i.e. stronger energy equipartition.

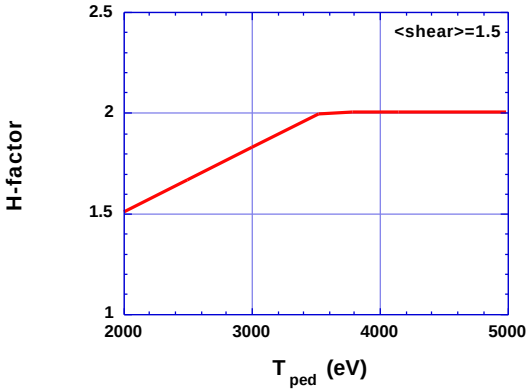

Figure 2.5-9b H-factor versus pedestal temperature predicted for ITER-FEAT by the analytic model. The two areas of confinement behaviour (stiff / non stiff) and the TPT of ~ 3.5 keV can be seen

By knowing the temperature (TPT ~ 3.5 keV) and assuming that the density on top of the pedestal is 0.8 of the operation density (0.8 $n_{average}$, ~ $0.8x10^{20}m^{-3}$), the energy content of the pedestal can be obtained. These considerations yield an energy stored in the pedestal of ITER-FEAT of ~ 107 MJ (53.5 MJ electron energy) which is ~ 1/3 of the total stored energy (stored energy ~ 350 MJ for the reference operation point at ~ 410 MW fusion power). Again this is in line with e.g. JET discharges with low gas puff at medium density and good H-mode confinement which also have pedestal energies in the order of 1/3 of the total stored energy. Of course there are other ways than the one described here to obtain the pedestal temperature and/or the pedestal energy content (e.g. offset linear confinement scaling). However, when comparing all existing attempts to extrapolate the pedestal energy content to ITER-FEAT, only the considerations described here are consistent with all experimental observations (e.g. confinement behaviour, energy stored in pedestal on existing machines, etc.).

Fraction of the pedestal energy content lost during an ELM

Once the energy stored in the pedestal is known, one has to assess the fraction of this energy which is lost during an ELM. One way of extrapolating the fraction of stored energy lost per ELM from present machines to ITER is by empirical scaling using the ELM database[26] constructed from JET and DIII-D discharges at separatrix triangularities between 0.25 and 0.3. From this database analysis it was found that the energy loss per ELM is about ~ 31% ±

[24] J. Stober, et.al., 7th IAEA Workshop on H-mode physics and Transport Barriers, Oxford 1999, to be published in PPCF

[25] G. Janeschitz, Yu. Igitkhanov, M. Sugihara et al., 26 the EPS Conference on Contr. Fusion Plasma Physics, Maastricht, (1999) p 1445.

[26] Leonard, A., et al., J. Nucl. Materials **266-269** (1999) 109.

5 % of the pedestal electron energy content. Assuming that the loss fraction will be the same in ITER-FEAT, the energy loss per ELM can be evaluated yielding an average energy loss per ELM of ~ 14 to 19 MJ which is 4% to 5.5% of the total stored energy. This result is in principle in line with observations on present machines[27], for low gas puff good energy confinement H-modes at < 0.5 of the Greenwald density.

The energy loss per ELM can be reduced by increasing the gas puffing rate. However, increasing the gas puffing rate and/or the density of a discharge significantly causes in many cases not only a reduction of the ELM size but also of energy confinement (Figure 2.5-10a). This loss of energy confinement can be understood from a reduction of the average pedestal pressure (ELMs are triggered early before maximum possible pressure is achieved) or by reducing the pedestal temperature below the TPT.

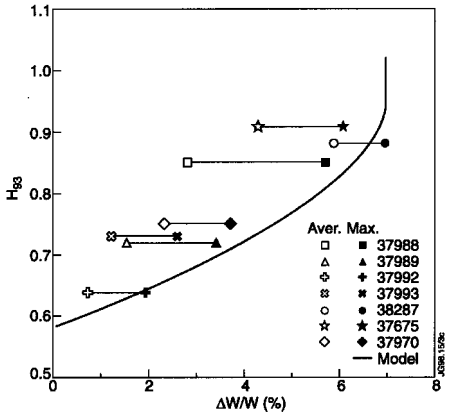

Figure 2.5-10a H-factor versus fraction of stored energy lost during an ELM in JET. In this series of discharges by increasing the gas puff (decreasing average pedestal energy content) the confinement decreases[28]

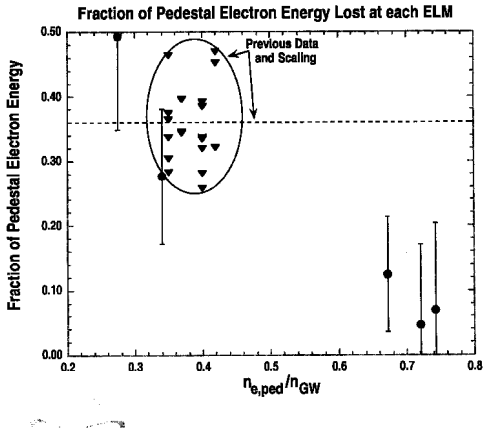

Figure 2.5-10b ELM electron energy loss fraction in DIII-D for standard medium density discharges (36%) and for discharges close to the Greenwald density (<10%) with relatively good energy confinement.

There are, however, several DIII-D discharges where the ELM energy losses were reduced by ~ factor 5 at high density (Figure 2.5-10b) when compared to low and medium density discharges with only moderately decreased energy confinement[29]. These discharges are at present limited to low power operation (< 3 MW NBI-heating) and the physics mechanism, which allows to retain reasonably good H-mode confinement, is not yet fully understood and it is therefore not known whether these discharges can be extrapolated to ITER-FEAT.

Also in ASDEX-UP a lower fraction of the total stored energy than in JET and DIII-D is lost in Type I ELMs (~ 2%) even at comparable triangularities. The times during which this energy is deposited on the divertor plates varies also and tends to be longer in DIII-D and ASDEX-UP (< 350 μs in medium densities and close to 1 ms in the very high density cases) when compared to JET and JT60U where the ELM energy deposition time at low to medium

[27] e.g. J. Stober, et.al., 7th IAEA Workshop on H-mode physics and Transport Barriers, Oxford 1999, to be published in PPCF
Fishpool, G.M., Nucl. Fusion **38** (1998) 1373.
[28] Fishpool, G.M., Nucl. Fusion **38** (1998) 1373.
[29] A. Leonard, et. al., Proceedings of the 14th PSI Conference, Rosenheim, May 2000

density is ~ 150 μs to 180 μs. These different observations suggest that a simple empirical scaling of the energy loss fraction and of the deposition time as a method to extrapolate to ITER-FEAT is at least questionable and should therefore be accompanied by some physics considerations.

The short deposition times reported by the larger machines suggest that there might be a collisionless transport of energy and particles to the divertor plates. In fact when assessing the collisionality in the SOL during an ELM for these machines, it is in the order of 0.1 (Figure 2.5-12a), based on the assumption that during an ELM the temperature and density at the separatrix are for a short period similar to the pedestal temperature and density and by taking the connection length from the midplane to the divertor into account. During an ELM, the bulk of the energy cannot travel faster than with the ion sound speed (ambipolarity, more than 50% of energy in the ions, low collisionality, no time for energy equipartition) which gives for a typical JET ELM a characteristic time of ~ 150 to 180 μs. However, in high density low pedestal temperature discharges such as the high density discharges in DIII-D and also in some discharges in ASDEX-UP, the SOL can become collisional also during an ELM, resulting in even longer energy deposition times (can be up to 1 ms) (Figure 2.5-11b). When assessing the collisionality during an ELM for ITER-FEAT it will be similar to JET and JT60U discharges (Figure 2.5-12) and not as large as in the high density discharges of DIII-D and ASDEX (> 1.0). Thus a collisionless transport of energy with ion sound speed can be expected also for ITER-FEAT ELMs.

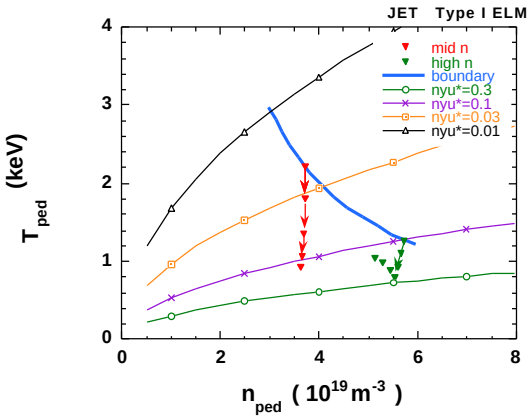

Figure 2.5-11a Pedestal n – T diagram for typical JET discharges and the estimated collisionality (0.03 to 0.1) when assuming pedestal n and T values in the SOL. Trajectories for ELMs are also shown.

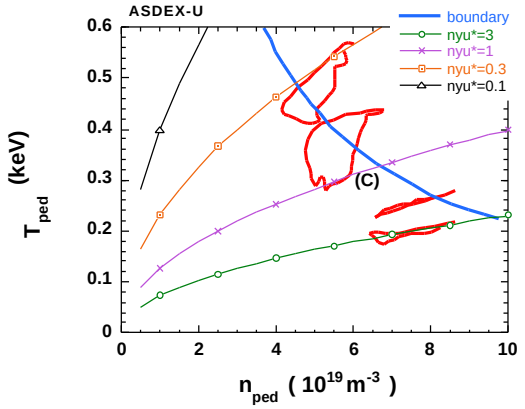

Figure 2.5-11b n-T diagram for ASDEX-UP and the collisionality (at C ~ 1.0 – 3.0) in the SOL assuming pedestal plasma parameters during an ELM. Trajectories for ELMs are also shown

The following mechanism can possibly control the fraction of pedestal stored energy lost per ELM. If one assumes that an ELM occurs because a pressure gradient limit (e.g. ballooning) is exceeded and if the transport of energy and particles across field lines is due to turbulence similar to an avalanche effect, as reported for the core plasma in heat pulse experiments, the driving term (pressure gradient) and thus the turbulence should last only a few 10th of μs, i.e. the gradient disappears on this fast timescale) Thus it becomes most likely shorter than the energy transport time along fieldlines when assuming ion convection is dominating there.

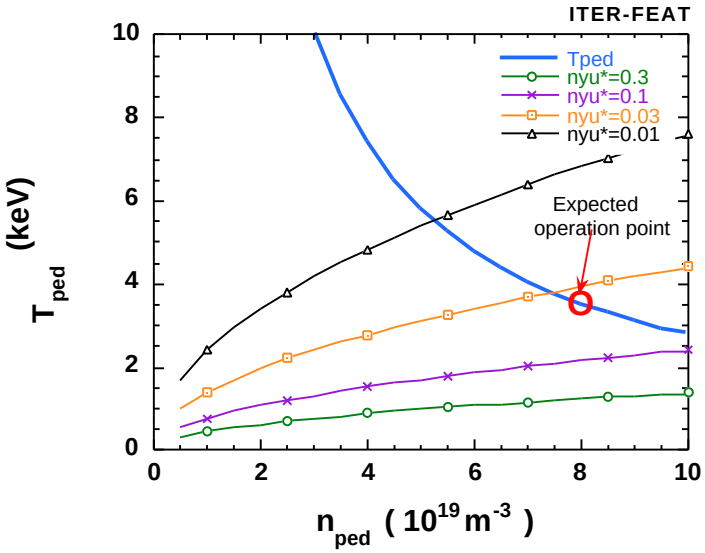

Figure 2.5-12 The expected n-T diagram for ITER-FEAT and the collisionality (~ 0.03) in the SOL assuming pedestal plasma parameters during an ELM.

This means that, with the assumed very short ELM avalanche, the maximum energy which can be lost during an ELM is determined by the characteristic loss time in the SOL and not by the pedestal physics. This loss time is in turn dependent on the temperature which exists in the SOL during an ELM and thus on the pedestal temperature. In order to apply such a scaling the ELM time (time of turbulence) and the fraction of stored energy which would be lost during an ELM without a transport limit in the SOL are unknowns. Therefore this model (idea) is an "ansatz" which has to be calibrated by data from one machine and can then be checked if it fits the observations on other machines.

A low and a very high density discharge of DIII-D have been taken for this calibration and the model then applied to JET, JT60U and ASDEX-UP. After the calibration on DIII-D the model predicts the observed energy loss fractions (compared to total stored energy) and as far as known also the correct deposition times in JET, JT60U and ASDEX-UP. It thus unifies the otherwise confusing observations with very different energy loss fractions and deposition times. While these considerations are very preliminary and must be checked in more detail, the good agreement of the model with data from existing machines encourages its use for extrapolation to ITER-FEAT as one possible way to assess an upper limit for the pedestal energy fraction lost during an ELM.

In ITER-FEAT the characteristic transport time in the SOL is ~ 310 μs when considering a pedestal temperature of 3.5 keV and a pedestal density of 8.0 $x10^{19}m^{-3}$ and thus twice as long as the one in JET and JT60U. This results in not quite a factor of 2 lower pedestal energy loss fraction than the one observed in JET and JT60U.

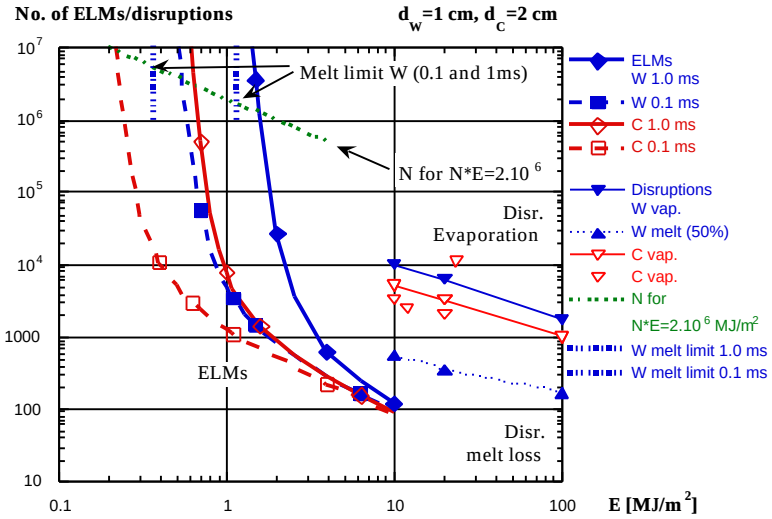

Figure 2.5-13 Divertor target lifetime in number of ELMs versus the energy deposited during an ELM for CFC and W clad targets

Table 2.5-1 Allowable Energy deposition on the divertor targets during ELMs

	C (0.3 ms)	W (0.3 ms)
Allowable energy deposition E (MJ/m^2) for 10^6 ELMs, deposition time = 0.3 ms	0.4	0.93 (0.64)
Allowable W_{ELM} (MJ) for 10^6 ELMs with deposition area $S = S_{SS} = 8\ m^2$	3.2	7.44 (5.1)
Allowable W_{ELM} (MJ) for 10^6 ELMs with deposition area $S = 2xS_{SS} = 16\ m^2$	6.4	14.9 (10.2)

S_{SS} -. Strike zone Surface ( ) considering melting

In order to decide whether ELMs are tolerable for the divertor targets of ITER-FEAT one has to be aware that during a 400 sec long discharge approximately 1000 ELMs will occur and that the lifetime of the targets should be in the order of several 1000 discharges. Due to the large number of ELMs during the life of an ITER divertor target no evaporation or melting of the target material can be accepted (too large erosion per ELM) resulting in the power deposition limits reported[30] and in table 2 for CFC and W targets, respectively. From Figure 2.5-13 and Table 2.5-1 one can see that an energy load of only 0.4 MJm^{-2} and 0.64 MJm^{-2} is allowed for CFC and W targets, respectively, when assuming an energy deposition time of 0.3 ms. The total allowed energy loss from the plasma during an ELM depends also on the surface area which receives this load (see Table 2.5-2). From present day machines we know that there is either no broadening of the strike zones (S_{SS} in Table 2.5-2) or at most a factor 2 widening of the main power deposition area[31].

Combining the energy deposition limits with the expected energy loss during ELMs in ITER-FEAT when using the physics based scaling and assuming 310 μs deposition time yields the results shown in Figure 2.5-14 for CFC (Figure 2.5-14a) and W targets (Figure 2.5-14b). The variation of the energy loss per ELM over fusion power in Figure 2.5-14 is obtained by using the assumed proportionality between fusion power and stored energy

[30] G. Federici, et. al., "Assessment of Erosion and co-deposition in ITER-FEAT", PSI 1999
[31] Leonard, A., et al., J. Nucl. Materials **266-269** (1999) 109.

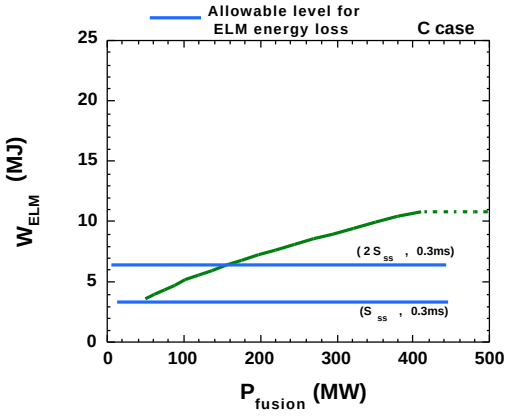

Figure 2.5-14aThe predicted ELM energy loss) and the allowable pulsed energy load for a CFC target. The predicted ELM energy loss exceeds the allowable above 200 MW fusion power.

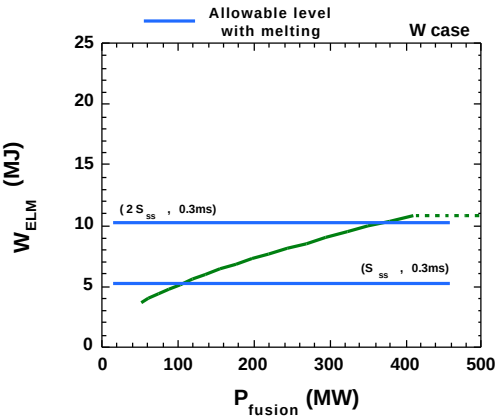

Figure 2.5-14bThe predicted ELM energy loss and the allowable pulsed energy load for a W target (melt limits from Figure - 2.5-13 are assumed). The predicted ELM energy loss has some overlap with the limits defined by melting almost up to the reference operation point..

Figure 2.5-14 shows that the energy loss per ELM might exceed the allowable level for vaporisation of the divertor plates for CFC targets and might be more acceptable for a W target when considering a factor 2 widening of the deposition zone. It is assumed that the ELM energy loss does not increase above the reference operation point because the pedestal energy content does not increase anymore above the TPT. If the high density discharges reported by DIII-D[32] could be directly extrapolated (same energy loss fraction) to ITER-FEAT, then a much larger overlap between allowable and expected ELM energy loss could be achieved. However, due to the different collisionality regimes between the ELMs in these DIII-D discharges and of the ones in ITER-FEAT, it is very questionable if such a direct extrapolation of the energy loss fraction to ITER is allowed.

Due to the fact that the error bars in all the above extrapolations are large and due to the fact that a model for the ELM itself does not exist, the predicted ELM energy loss in ITER-FEAT has certainly large error bars. Therefore, definitive conclusions cannot be reached at present. Nevertheless, it might be that a Type-I ELM regime without mitigation techniques for the ELM energy losses, which must not reduce the energy confinement, will only be marginally usable in ITER-FEAT

However, if it is possible to peak the density profiles and thus to reduce the pedestal density, at constant or even increased line-average density, the pedestal pressure and thus also the pedestal energy content can be decreased without a significant loss of confinement (pedestal temperature stays above TPT). This has been observed in pellet-fuelled discharges[33]. A simple assessment for ITER-FEAT shows that with a density peaking factor of 2, a reduction in the ELM energy loss by ~ factor 2 (lower pedestal energy content), is feasible without a loss of confinement which would make Type-I ELMs most likely compatible with a W and a CFC target. While this example demonstrates that there is in principle some experimental

[32] A. Leonard, et. al., Proceedings of the 14th PSI Conference, Rosenheim, May 2000

[33] O. Gruber, et al., 17th IAEA Fusion Energy Conference, Yokohama, Japan, IAEA-F1-CN-69/OV4/3 (1998).

flexibility which might allow Type-I ELM operation in ITER-FEAT, the situation remains marginal and alternative high energy confinement regimes need to be investigated for their applicability to ITER-FEAT.

An H-mode regime with high pedestal pressure, good confinement and small or no ELMs exists. It is called either grassy ELM[34], Type-II ELM[35] or Enhanced D-Alpha (EDA)[36] regime and might be a backup solution for the reference Type-I ELM regime in ITER-FEAT. However, based on present knowledge it can only be obtained at $q_{95\%} > 3.5$ and at high triangularity > 0.4. Only if more data and a better understanding of this regime is available it will be possible to assess its applicability to an ITER like machine.

The RI mode is another possible high confinement regime and can in principle be understood in the same way as the pellet injection discharges from the high field side, i.e., the peaking of the density profile compensates the reduction of the pedestal pressure or in extreme cases the existence of an L-mode edge by directly improving the ITG caused transport[37]. The relevance of this operation regime for ITER-FEAT must be demonstrated on large machines (e.g. JET, JT60U), before this scenario can be employed as a backup for the Type I ELMy H-mode.

2.5.5. Probabilistic Performance Assessment using Different Confinement Scalings

A probabilistic performance assessment has been made by assuming a normal distribution function for the H_H-factor with standard deviation σ. Under this assumption, the expectation of achieving a Q value of at least a specified value, Q_0 is estimated considering the beta $\beta_N \leq 2.5$, the L-H transition threshold power, P_{LH}, and the density $n_e / n_{GW} \leq 0.85$. In this section, results for various scaling formulae are shown. Here, IPB98(y,1) scaling, IPB98(y,2) scaling, IPB98(y,3), IPB98(y,4) scaling and IPB98(y) scaling are examined.

Figure 2.5-15 shows calculation results for the expectation of achieving $Q \geq Q_0$ for various scaling formulae when $\tau_{He}^*/\tau_E = 5$, $n_e/n_{GW} \leq 0.85$, $P_{LOSS}/P_{LH} \geq 1.0$ and the uncertainty for the scaling formula $\sigma = 20\%$. Here, the "maximised conditional probability (MCP)" is obtained by optimizing the heating power[38]. When $\sigma = 20\%$, the MCPs of achieving $Q \geq 10$ are about 65-90%, and those of achieving $Q \geq 50$ is 25-60%. The MCPs for $Q \geq 10$ are not sensitive to the assumption for LH-transition power assumptions ($P_{LOSS}/P_{LH} \geq 1.3$ or 1.0).

Figure 2.5-16 shows the case when $\sigma = 10\%$. The MCPs of achieving $Q \geq 10$ are about 80-95%, and those of achieving $Q \geq 50$ is 10-70%.

[34] Y. Kamada, et al., 7th IAEA TCM on H-mode and Transport Barrier Physics, Oxford, Sep. 1999.
[35] T. Ozeki, et al., Nucl. Fusion **30** (1990) 1425.
[36] M. Greenwald, et al., 17th IAEA Fusion Energy Conference, Yokohama (1998) IAEA-F1-CN-69/EX1/4.
V. P. Bahtnagar, et al., 18th EPS Conference on Controlled Fusion and Plasma Physics, vol. 1 (1991) p369.
[37] A. Messian, et al., Phys. Rev. Lett. **77** (1996) 2487.
[38] ITER EDA Document GA0RI199-02-12 W0.2 Study of RTO/RC ITER Options

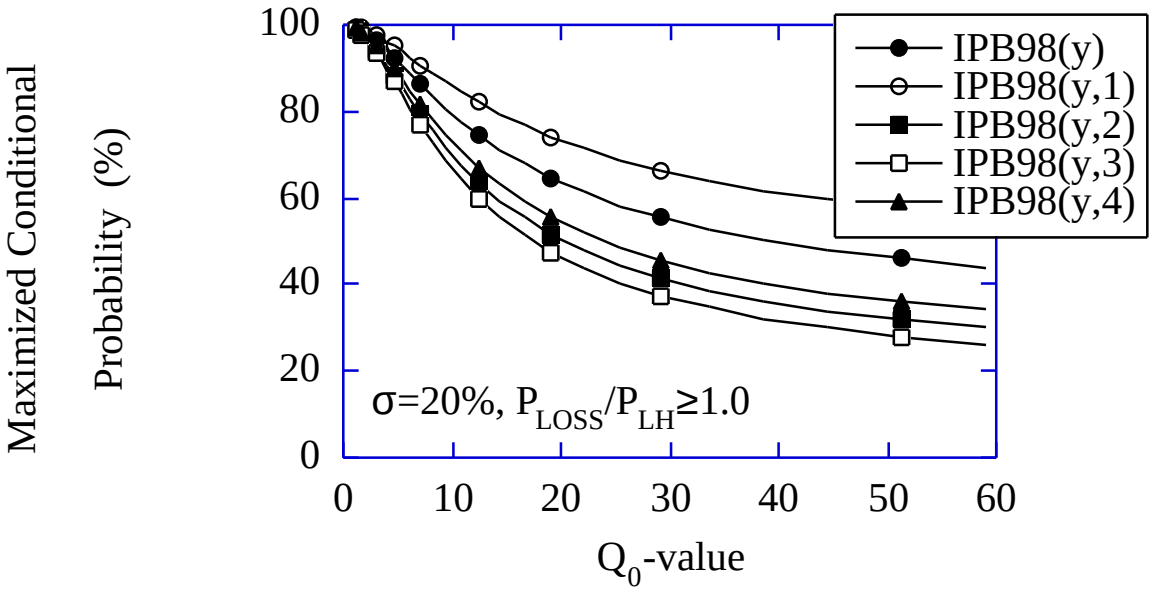

Figure 2.5-15 Expectation of achieving $Q \geq Q_0$ for various scaling formulae when $\tau_{He}^*/\tau_E = 5$, $n_e/n_{GW} \leq 0.85$, $P_{LOSS}/P_{LH} \geq 1.0$ and the uncertainty for the scaling formula $\sigma = 20\%$.

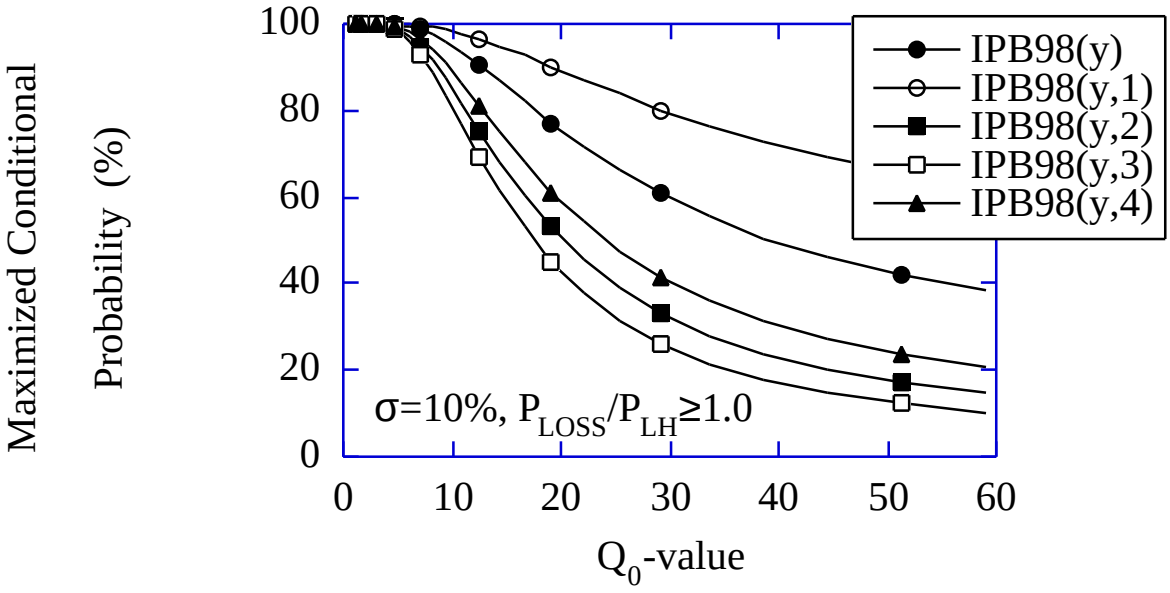

Figure 2.5-16 Expectation of achieving $Q \geq Q_0$ for various scaling formulae when $\tau_{He}^*/\tau_E = 5$, $n_e/n_{GW} \leq 0.85$, $P_{LOSS}/P_{LH} \geq 1.0$ and the uncertainty for the scaling formula $\sigma = 10\%$.

2.5.6. A Dimensional Extrapolation Technique based on a System Code Applied to the ITER H-mode Energy Confinement Database

[The content of this section was first presented at the last TAC meeting in Naka in December 1999 as a result of preliminary studies and was included in the final version of the ODR submitted to the Parties in January 2000. It is provided here with further elaboration for the benefit of TAC members.]

This novel approach tries, amongst other things, to overcome the difficulty associated with the simultaneous choice of non-dimensional parameters (A = R/a, κ, δ, q_{95}, β_N, n/n_{GW}) which, when close to their respective limits, may have some significant hidden interactions which affects the energy confinement. As an example, this is observable in the effect of shear (triangularity, q, κ, A) on confinement in high density discharges, or the effect of sawteeth on low edge safety factor discharges at high elongation and triangularity[39].

In addition, the proposed methodology addresses, in part, the fact that the enhancement factor H_H cannot be treated as a simple scalar because it may hide some additional variables as well as explicitly treated terms (in the energy confinement formula), for example the density or elongation, the influence of which on the energy confinement time may not be mathematically expressed in a simple monomial form within the empirical formula for energy confinement time. The employed procedure is as follows:

1. each shot in the database is evaluated by extracting all of its parameters and sizing by means of the system code (in accordance with the ITER criteria) for a Q = 10 machine with the same geometry (k, δ, A=R/a) , q_{95}, and n/n_{GW}: these parameters are then assumed to come as a "package";
2. the extrapolation in the energy confinement time is performed based on the empirical scaling coefficients applied only on the parameters not kept constant, and by using relative ratios. There is no need for H_H.

The energy confinement time empirical scaling then becomes:

$$\tau_{E,Q10} = \tau_{E,DBSHOT} \left(\frac{I_{Q10}}{I_{DBSHOT}}\right)^{\alpha_I} \left(\frac{P_{Q10}}{P_{DBSHOT}}\right)^{\alpha_P} \left(\frac{B_{Q10}}{B_{DBSHOT}}\right)^{\alpha_B} \left(\frac{R_{Q10}}{R_{DBSHOT}}\right)^{\alpha_R} \left(\frac{M_{Q10}}{M_{DBSHOT}}\right)^{\alpha_M} \left(\frac{n_{Q10}}{n_{DBSHOT}}\right)^{\alpha_n} \qquad (1)$$

where :

- the subscript "Q10" refers to the Q = 10 machine designed from the shot in the H-mode database and indicated with the subscript "DBSHOT".
- The α_i exponents are the same exponents found in the empirical scaling law for the correspondent parameters.

In addition, considering then the following relationships:

$$q = \frac{BR}{I} * f(\delta, \kappa, A) \quad ; \quad n_{GW} = \frac{I}{\pi a^2} \qquad (2,3)$$

[39] Saibene G. et al, Nuclear Fusion 39, 1133 (1999)
Stober et al, 26th EPS conf. on controlled fusion, Maastricht (1999)
Kamada Y.et al, 14th. IAEA Conf. Plasma Physics, Wuerzburg (1992)
Horton L.D. et al, Nuclear Fusion, 39 993 (1999)

equation (1) further simplifies, because q_{95}, geometry, and normalised density are fixed in the extrapolation, to:

$$\tau_{E,Q10} = \tau_{E,DBSHOT}\left(\frac{P_{Q10}}{P_{DBSHOT}}\right)^{\alpha_P}\left(\frac{B_{Q10}}{B_{DBSHOT}}\right)^{\alpha_B+\alpha_n+\alpha_I}\left(\frac{R_{Q10}}{R_{DBSHOT}}\right)^{\alpha_R-\alpha_n+\alpha_I}\left(\frac{M_{Q10}}{M_{DBSHOT}}\right)^{\alpha_M} \quad (4)$$

Considering, for example, the IPB-98y2 empirical scaling law for ELMy H mode:

$$\tau_{E,th}^{IPB98(y,2)} = 0.0562 H_H I^{0.93} B^{0.15} P^{-0.69} n_{19}^{0.41} M^{0.19} R^{1.97} \varepsilon^{0.58} \kappa_a^{0.78} \quad (5)$$

then expression (4) becomes:

$$\tau_{E,Q10} = \tau_{E,DBSHOT}\left(\frac{P_{Q10}}{P_{DBSHOT}}\right)^{-0.69}\left(\frac{B_{Q10}}{B_{DBSHOT}}\right)^{1.49}\left(\frac{R_{Q10}}{R_{DBSHOT}}\right)^{2.49}\left(\frac{M_{Q10}}{M_{DBSHOT}}\right)^{0.19} \quad (6)$$

Of the more than a thousand shots in the ELMy H-mode database, less than half turn out to extrapolate to a Q = 10 machine whose major radius is smaller than 8 m, however about 70 extrapolate to a Q = 10 machine with R < 6.2 m.

Figure 2.5-17 shows the major radius of the extrapolated Q = 10 machine versus the edge safety factor q_{95} of the analyzed shots. It is apparent that there are a good number of shots, from DIII-D, JET, and ASDEX-U, which confirm the robustness of the ITER-FEAT design in reaching the Q = 10 objective on the basis of the existing experimental results. Of particular interest are those DIII-D shots which are capable of being extrapolated to a competitive Q = 10 device, even at a rather large edge safety factor. It is nevertheless clear that the choice of a safety factor of about 3 is sound.

As an even more general simplification to the proposed approach, the use of an empirical scaling formula for the energy confinement time can be completely avoided if the extrapolated device is sized based on a fusion power requirement and not on the amplification factor Q. In order to do so, the above-mentioned, non-dimensional parameters are chosen to be kept constant, based on the consideration that the most unpredictable, from first principles, turbulent, phenomena taking place in the plasma are mostly influenced by stability and even more so by the geometry of the magnetic field, q and shear profiles. In addition, in this second methodology, the value of $ß_N$ observed in the extrapolated experiment is also fixed. This last hypothesis implies that the magnetic and pressure profiles in the experiment in question and the larger extrapolated device are completely self similar. The pressure scales then as:

$$p \quad B^2 \quad (7)$$

And, for a DT experiment, the fusion power then scales approximately as:

$$P_f \approx p^2 \quad V \quad B^4 R^3 \quad (8)$$

However, considering that the total fusion power is not exactly proportional to T^2, it is in principle necessary, but not too important for the result, to choose an operating density. This can be taken assuming also in this case the same density normalised to the Greenwald density scaling as:

$$n \quad \frac{I}{a^2} \quad \frac{B}{R} \tag{9}$$

Figure 2.5-18 shows the machine major radius versus the safety factor at the edge. Also in this case, a number of shots extrapolate to a 500 MW device with a major radius smaller than the one of ITER-FEAT. In summary, also in accordance with this alternative design methodology, the ITER-FEAT design seems to be soundly based on the extrapolation of many high performance ELMy H-mode shots from JET, DIII-D, and ASDEX-U.

The procedure above thus enables the fusion power to be extrapolated but not the transport losses and thus the value of Q to be predicted. However, by considering that the temperature scales as:

$$T \quad \frac{p}{n} \quad BR \tag{10}$$

and assuming that τ_E scales as gyroBohm, we have:

$$\tau_{E,GyroBohm} \quad \frac{a^2}{\rho^* \quad \chi_{Bohm}} = \frac{R^2}{\frac{\sqrt{MT}}{\varepsilon RB}\left(\frac{T}{B}\right)} \quad R^{1.5} \quad B^{0.5} \quad M^{-0.5} \tag{11}$$

The inverse isotopic mass dependence, shown in equation (11) is not supported by the empirical scaling laws, which typically have a positive exponent. This could be because the positive mass dependence of the pedestal edge width shown in experiments[40] is neglected whereas it is thought that the edge pedestal width scales with a complex function of magnetic shear, machine size and thermal ion Larmor radius. Considering equation (11) for the evaluation of the energy confinement time, the lowest *cost* shots turn out to have a value of Q in the range between 4 and 15.

The scaling derived above can be compared with the different scaling laws expressed in the ITER Physics Basis[41]. By assuming the usual set of non-dimensional parameters equation (6) above becomes:

$$\tau_{E,Q10} = \tau_{E,DBSHOT} \left(\frac{B_{Q10}}{B_{DBSHOT}}\right)^{\frac{\alpha_B+\alpha_n+\alpha_I+2\alpha_P}{1+\alpha_P}} \left(\frac{R_{Q10}}{R_{DBSHOT}}\right)^{\frac{\alpha_R-\alpha_n+\alpha_I+3\alpha_P}{1+\alpha_P}} \left(\frac{M_{Q10}}{M_{DBSHOT}}\right)^{\frac{\alpha_M}{1+\alpha_P}} \tag{12}$$

Figure 2.5-19 compares the various empirical laws with the one derived on the basis of gyroBohm scaling, all under the assumptions of freezing the same non-dimensional parameters (A, k, δ, q_{95}, β_N, n/n_{GW}) in the extrapolation. With the exception of the scaling IPB98(y,3), where a free fit without Kadomtsev constraint was performed, all scalings are very similar in the coefficients γ_B and γ_R. For a given engineering approach the relation between R and B is, to a first approximation, one of proportionality, when aspect ratio and elongation are constant. This means that the sum $\gamma_B + \gamma_R$ is the single most important coefficient in the scaling. When compared with eq. (11), the scalings 98(y), 98(y,1) give a more favourable size/field effect whereas scaling 98(y,2), 98(y,3), and 98(y,4) yield the opposite result.

[40] Cordey J et al, JET P98(53) , Submitted to Nuclear Fusion.
[41] ITER Physics Basis, Nucl. Fus. 39 (1999)

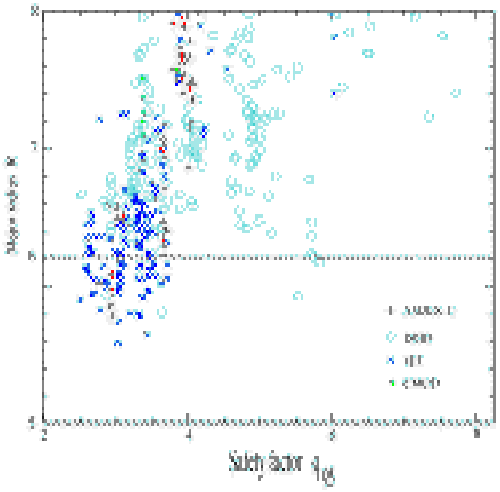

Figure 2.5-17 Major Radius of Q = 10 Machine vs. q_{95} Obtained with Dimensional Extrapolation Methodology

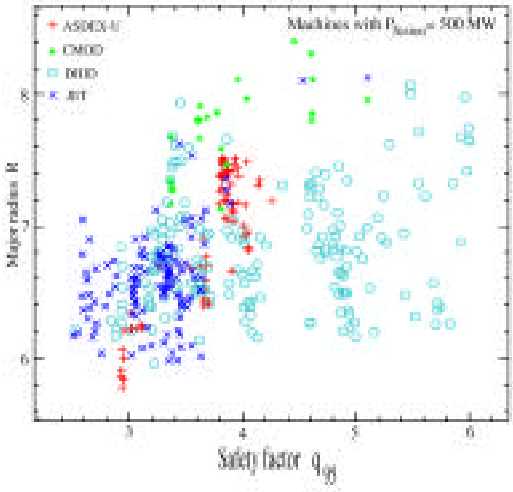

Figure 2.5-18 Major Radius of 500 MW Fusion Power Device versus Safety Factor in the Database under the Assumption of Constant Beta

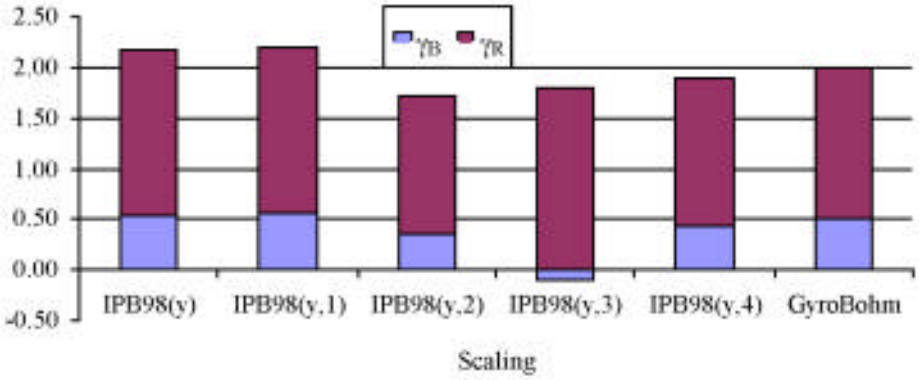

Figure 2.5-19 Comparison of Gyrobohm scaling versus IPB empirical scalings at constant n/n_{GW}, $ß_N$, and magnetic field geometry.

2.6. Progress in Divertor Modelling

2.6.1. SOL Width

Extrapolation of the SOL width to a reactor-scale machine is one of the primary concerns for the divertor design. At present, experiments show a narrow power SOL (well below 1 cm) and, according to the common physical picture developed some 20 years ago[42], it should become even narrower when the power increases. Indeed, the SOL width is determined by a competition between the cross-field and parallel transport. If the cross-field transport stays approximately constant, then an increase of power causes an increase of the plasma temperature at the separatrix and the parallel transport gets significantly faster, making the

[42] Harrison, M., et al., Nucl. Technology/Fusion **3** (1983) 432

SOL narrower. Experiments generally confirm this trend, especially in L-mode discharges, see e. g. Figs.2.6–1, 2.6–3. However, the trend is opposite in the high-power H-mode experiments[43] which show some increase of the SOL width with power, Fig.2.6–2. Increase of the SOL width with the input power for H-mode can also be seen from the JET data, Fig.2.6–3, if one considers only the points with power greater than 8 MW. A formal statistical fit over the whole power range is simply misleading here.

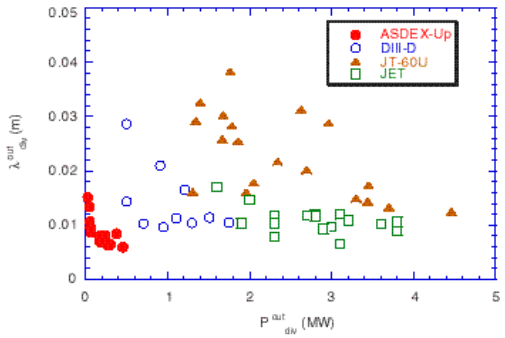

Figure 2.6–1 Width of power deposition profiles in L-mode for different machines (experiment)[44]

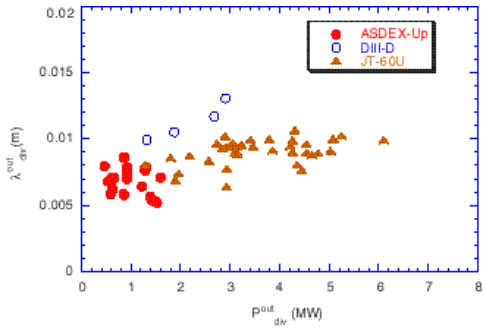

Figure 2.6–2 The same in H-mode

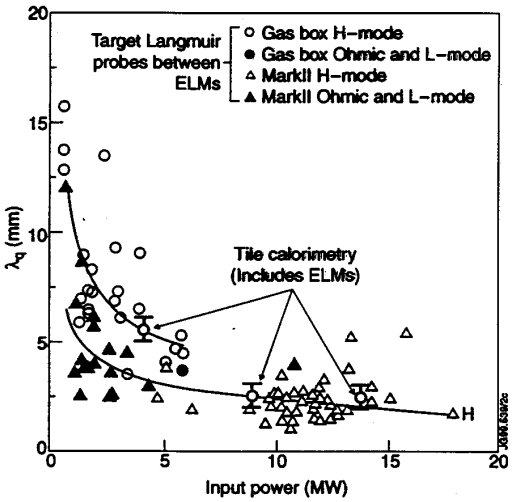

Figure 2.6–3 Width of power deposition profiles from JET (experiment)[45].

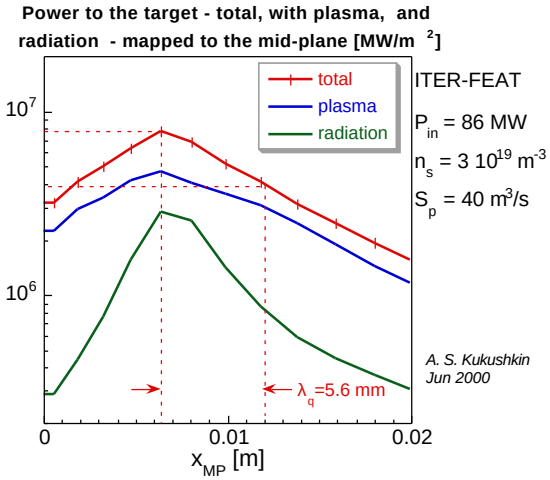

Figure 2.6-4 Typical power deposition profiles on the outer target of ITER-FEAT, mapped to the mid-plane.

Detailed profile measurements on ASDEX Upgrade[46] between ELMs have shown that the temperature gradients in high-power H-mode stay constant, corresponding to the ballooning limit, and continue smoothly across the separatrix. This allows the proposition of a model where the cross-field transport coefficients increase when the gradients approach the

[43] Loarte, A., et al., J. Nucl. Mater. **266-269** (1999) 587
Herrmann, A., et al., Proc. 23rd EPS Conf. Cont. Fusion Plasma Phys., Vol. 20C, Part II (1996) d-039.
Buchenauer, D., et al., J. Nucl. Mater. **196-198** (1992) 133.
Itami, K., et al., J. Nucl. Mater. **196-198** (1992) 755.
[44] Jaquinot, J., TAC meeting, Dec. 1999, Naka; Matthews, G., Expert Group meeting, Dec. 1999, Naka
[45] Jaquinot, J., TAC meeting, Dec. 1999, Naka; Matthews, G., Expert Group meeting, Dec. 1999, Naka
[46] Neuhauser, J., et al. 26th EPS Conf. Contr. Fusion Plasma Phys., Maastricht, 1999. Paper P4.040

ballooning limit[47]. Such a model produces a qualitatively correct dependence of the SOL width on power, and it is consistent with interpretative modelling done for ASDEX Upgrade[48] where an increase of the fitted transport coefficients for H-mode discharges at high power was reported.

In ITER modelling, $\chi = 1$ m^2/s is normally used. This value may appear strongly overestimated in a plain comparison with the coefficients used to fit the experimental profiles in H-mode at low power (typically, below 0.1 m^2/s). However, the SOL width predicted for ITER-FEAT with the reference coefficient is around 5 mm, Figure 2.6–4, and, in line with the previous ASDEX Upgrade results, is consistent with the pressure gradient at the plasma edge in ITER-FEAT being close to the ballooning limit. The choice of the cross-field transport coefficients $\chi = 1$ m^2/s used in ITER-FEAT divertor modelling is therefore reasonable.

2.6.2. Code Validation

The models used for predictions of the divertor performance in ITER-FEAT are validated against the data from a variety of experiments and their predictive capability is probably higher than that for the core plasma models. Detailed model validation is mostly done by the Home Teams. In particular, the B2-Eirene code package has been extensively validated against the data from ASDEX Upgrade[49] and JET[50]. The code had been used to analyse the "Lyra" divertor performance in ASDEX Upgrade before the experiments started, and the results show remarkable accuracy in the predictions of the divertor power load, radiation distribution, and helium and neon compression (see Figures 2.6-5 and 2.6-6). The codes are still unable to reproduce fully the experimentally observed in-out asymmetries – probably because of the lack of adequate description of the drifts and currents in the SOL. Work is being done on the model improvement in this direction[51]. From a broader perspective, many essential features of plasma detachment (e.g. low plasma temperature, importance of volumetric recombination) were first predicted by modelling and then confirmed by experiment. Also some apparently minor but potentially important effects like the self-sustained oscillations in the divertor plasma[52] had been predicted long before they were identified in experiments. The generally good agreement of the modelling results with existing experiments and the proven predictive capability give confidence for predicting the performance of the ITER-FEAT divertor.

[47] Kukushkin, A. S., et al. Proc. 7th PET Workshop, Tajimi, Japan, 1999. To be published in "Contributions to Plasma Phys."
[48] Coster, D., et al., ibid.
[49] Schneider, R., et al. Fusion Energy 1998 (Proc. 117th Conf., Yokohama, 1998) IAEA, Vienna, 1999, p.1525
[50] Loarte, A., et al. J. Nucl. Mater., **266-269** (1999) 146
[51] Chankin, A., et al. Contributions to Plasma Phys. **40** (2000) 288
Schneider, R., ibid.
[52] Krasheninnikov, S. I., et al. Nucl. Fusion **27** (1987) 1805
Loarte, A., et al. Phys. Rev. Let. **83** (1999) 3657

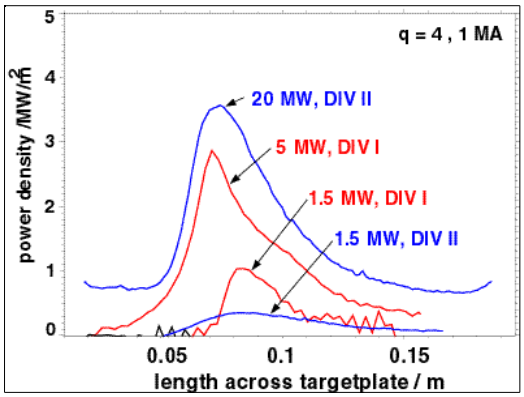

(a) calculated profiles of power load on the outer divertor target

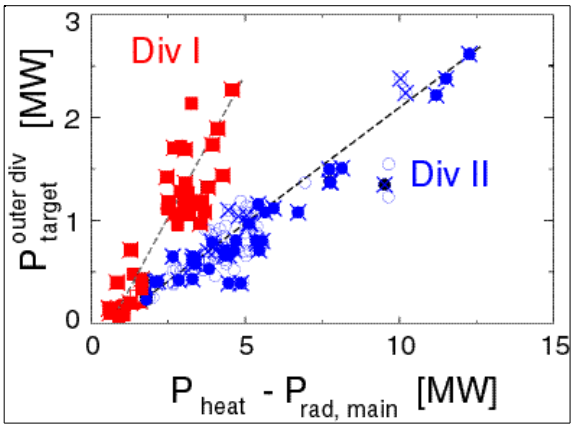

(b) measured power to the outer divertor target

Figure 2.6-5 Predicted reduction of power load by a factor 2 to 3 in Divertor II ("Lyra") of Asdex Upgrade, as compared to Divertor I, is clearly seen in the experiment[53].

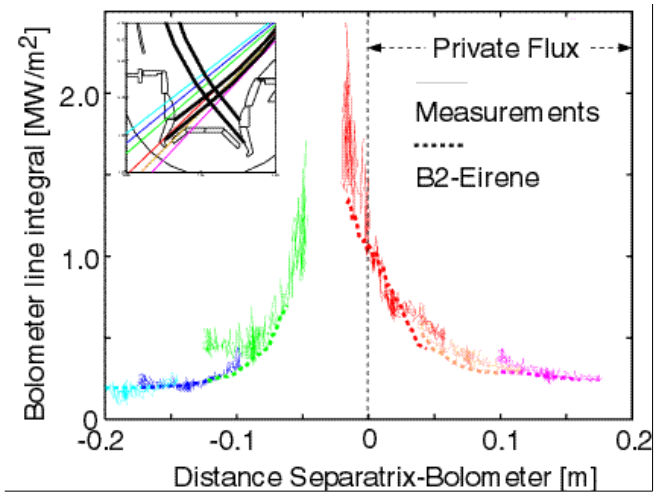

Figure 2.6-6 Comparison of predicted and measured bolometer signals for Divertor II of Asdex Upgrade[54].

2.6.3. Divertor Geometry Effects

Design studies undertaken in the last 2 years and aimed at a reduction of the cost (i. e., of the size) of ITER have resulted in ITER-FEAT. These studies have involved a broad variation of the divertor geometry retaining the vertical target plates in the divertor. From the point of view of divertor modelling, the ODR was based on the results obtained for the earlier versions (LAM, IAM, etc.). The most significant difference in the divertor geometry between FEAT and earlier versions, which was not understood at that time, was in abandoning the dump target, Figure 2.6-7a. The effect of dump target, or the V-shaped divertor bottom near the strike point, has recently been analysed[55]. It is shown that this "V" is beneficial for

[53] Schneider, R., et al. Fusion Energy 1998 (Proc. 17th Conf., Yokohama, 1998) IAEA, Vienna, 1999, p.1525
[54] Schneider, R., et al. Fusion Energy 1998 (Proc. 17th Conf., Yokohama, 1998) IAEA, Vienna, 1999, p.1525
[55] Kukushkin, A. S., et al., 14th PSI Conference, Rosenheim, May 2000. To be published in J. Nucl. Mater.

reduction of the peak power loads primarily because it keeps high neutral density near the strike point and furthers the partial detachment. A similar effect was previously reported from JET experiments where the separatrix was swept across the divertor targets in both Mark I and Mark II divertors[56].

Figure 2.6-8 shows the comparison of the peak power load for one of the previous modifications (LAM) and different variants of the FEAT divertor geometry for the same input power of 100 MW. In these calculations, besides DT and He, the C ions are present in the plasma and they ensure the necessary radiation level. The source of carbon is mostly chemical sputtering of the target surfaces with a constant yield of 1 %, although physical sputtering is also taken into account. The divertor geometries for the compared cases are shown in Figure 2.6-7. The striking difference between the baseline FEAT and LAM can be attributed to the different target shape: the straight target originally proposed for FEAT is less efficient in assisting the plasma detachment around the strike point, whereas the pronounced "V" with the strike point almost in the corner does this job for the LAM. Minor variations of the divertor shape for FEAT ("V-out" and "V-in") also show significant reduction of the peak power, Figure 2.6-8, although in these studies, plugging the "V" by plasma was less efficient than in the LAM cases. Another important parameter which could explain the remaining difference between the V-shaped FEAT divertor and LAM divertor is the pumping speed. It was about 60 m^3/s for the LAM and 75 m^3/s for FEAT calculations shown here, and reduction of the pumping speed increases the neutral pressure in PFR and facilitates the partial detachment near the strike point[57], thus lowering the divertor target load (Figure 2.6-9) without increasing too much the He density at the separatrix.

A V-shaped configuration of the target and divertor floor is beneficial for divertor performance. It provides a considerable reduction of the peak power loads on the target without spoiling the helium removal. The effect is mostly due to accumulation of neutrals near the strike point when the "V" is plugged by plasma, as confirmed by the available experimental data from JET. Such a configuration could also be useful for transients such as ELMs, providing some shielding for the targets. It can however negatively affect the operational flexibility of the machine since the freedom of positioning the strike point is reduced. As a result of these studies, it is recommended to keep a V-shaped target configuration in ITER-FEAT.

[56] Loarte, A., Nucl. Fusion **38** (1998) 587.

Monk, R., et al., Proc. 24th EPS Conf. Contr. Fusion Plasma Phys., Berchtesgaden, 1997, Vol. 21A, p. 117.

[57] Kukushkin, A. S., et al., 14th PSI Conference, Rosenheim, May 2000. To be published in J. Nucl. Mater.

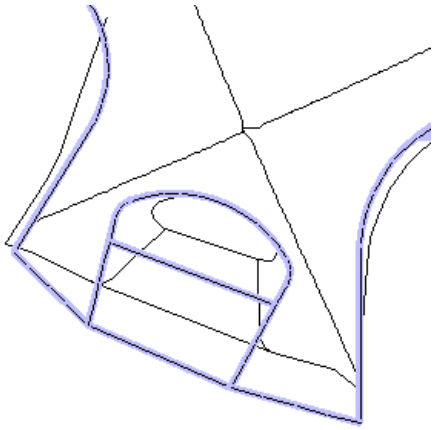

(a) Divertor geometry: FEAT (thick lines) vs. LAM. The picture for LAM is shifted to ensure the same position of the x-point. The V-shaped geometry of the outer target, consisting of the vertical target and dump target wetted by plasma, sharply contrasts the FEAT layout.

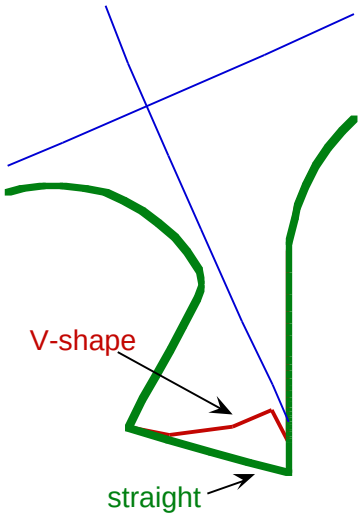

(b) V-shape vs. straight target geometry for FEAT

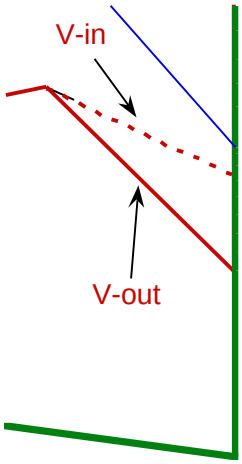

(c) Variations of the V-shape for FEAT (zoomed). V-out: wall shadowed by the dome; V-in: dump target

Figure 2.6-7 Variations of the divertor geometry used for modelling presented in Figure 2.6-8

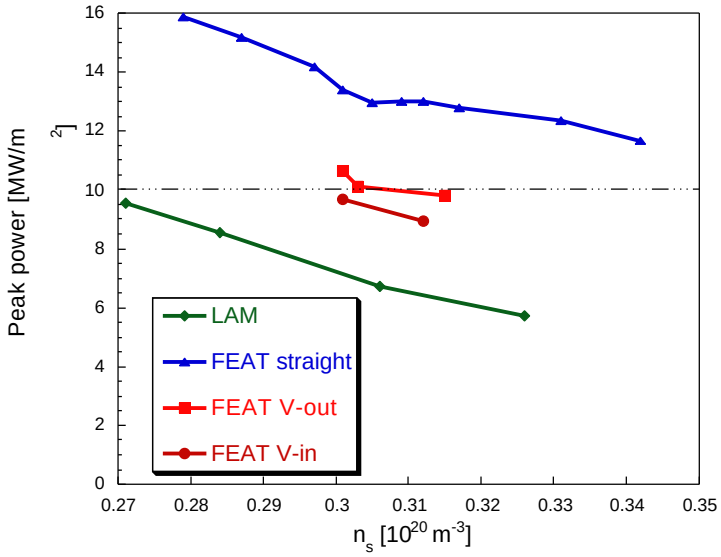

Figure 2.6-8 Peak power load q_{pk} vs. upstream plasma density at the separatrix n_s for different divertor geometry. The total power entering the SOL region is 100 MW. The variation of the divertor geometry is shown in Figure 2.6-7.

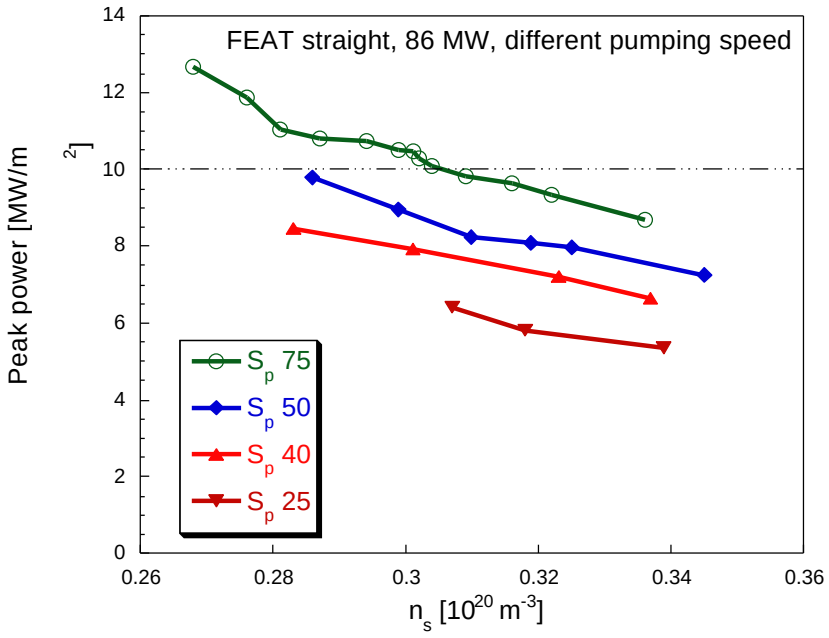

Figure 2.6-9 Peak power load q_{pk} vs. upstream plasma density at the separatrix n_s for different pumping speed (75, 50, 40, and 25 m^3/s), with 86 MW input power, straight target geometry (see Figure 2.6-7)

2.6.4. Operational window for ITER-FEAT

The window for divertor operation in ITER is delimited by several constraints, summarised in Table 2.6-1, arising from core plasma and technology requirements[58]. Several different means of controlling the operational point of the ITER-FEAT divertor in this 6-dimensional window have been considered[59] and the results are briefly summarised as following.

For the baseline ITER-FEAT divertor, without V-shaped geometry, at full pumping speed of 75 m^3/s and without additional impurity seeding, there is no window for the input power above approximately 80 MW. At higher powers, 86 MW and above, whenever the peak power load is brought low enough, the particle throughput and eventually the upstream density become too high. There is however a considerable margin in Z_{eff} and some margin in c_{He}.

Impurity seeding (in addition to the automatically-produced carbon) can permit the window to be extended somewhat. However, neon seeding is not appropriate. Instead of adding to carbon, neon largely replaces carbon as the radiator, radiating further away and thereby reducing the peak heat load, but it produces higher Z_{eff}. It does not radiate much below 20 eV. Seeding with a different impurity having radiation efficiency higher than carbon could be more effective – the tradeoff here is between the radiation and Z_{eff}.

Reducing the pumping speed opens the window for 86 and 100 MW. It leads to higher c_{He} at the same upstream density, but somewhat lower c_{He} at the same throughput.

[58] Janeschitz, G., et al., 14th PSI Conference, Rosenheim, May 2000. To be published in J. Nucl. Mater.
[59] Kukushkin, A. S., et al., 14th PSI Conference, Rosenheim, May 2000. To be published in J. Nucl. Mater.

For the same pumping speed of 75 m^3/s, the V-shaped geometries show much better performance than the straight one: the 100 MW curve lies at the corner of the window in q_{pk}, and Γ_{DT}, and the 86 MW points investigated lie just outside the Γ_{DT} limit implying that acceptable solutions exist at somewhat lower n_s. Reduction of the pumping speed should then increase the available operational space, and the margin in Z_{eff} suggests that impurity seeding can also be used here. Helium removal does not deteriorate with V-shaped target configurations.

An operational window in 6-dimensional phase space for ITER-FEAT is shown in Figure 2.6-10. Only points which satisfy all the constraints and which are produced using the different means of divertor operation control discussed above are shown, demonstrating that powers up to 100 MW can be accommodated. Reduction of the upstream plasma density below $2.5 \cdot 10^{19}$ m^{-3}, which may be needed for non-inductive operation, does not however look feasible. Variation of the pumping speed and fuelling rate in combination with impurity seeding provides control of the operational point within the window. Further exploration of these control means is in progress.

Table 2.6-1 Limits of the operational window of the ITER-FEAT divertor

Peak power load on the targets	$q_{pk} \le 10$ MW/m^2
D-T particle throughput	$\Gamma_{DT} \le 200$ Pa·m^3/s
Core fuelling	$0 \le \Gamma_{core} \le 100$ Pa·m^3/s
Upstream plasma density	$n_s \le 0.33 \cdot 10^{20}$m^{-3}
Helium concentration in the core plasma	$c_{He} \le 0.06$
Z_{eff} in the core plasma	$Z_{eff} \le 1.6$

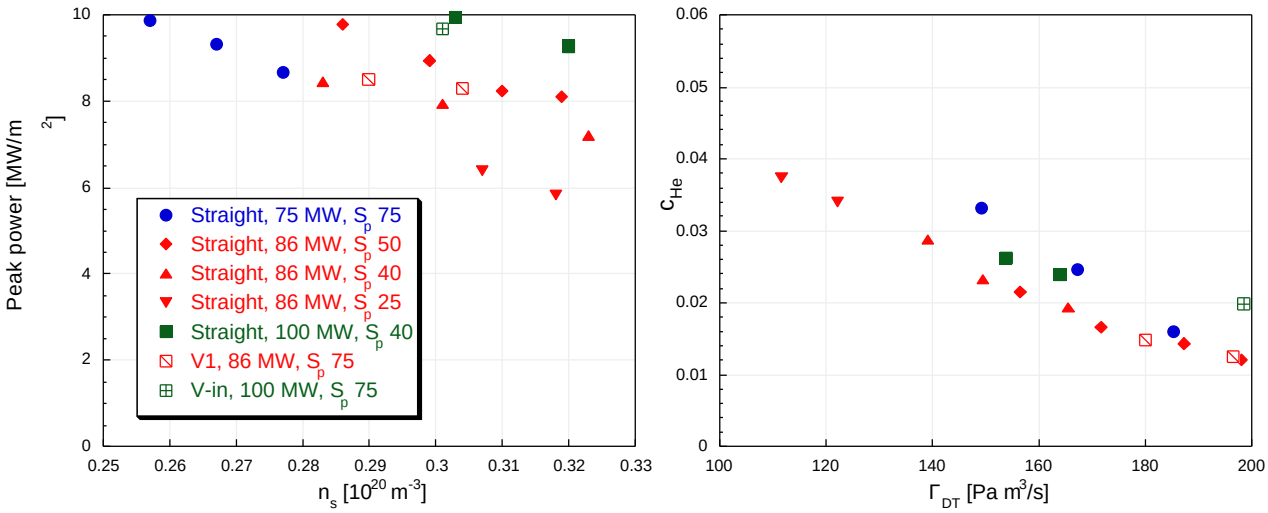

Figure 2.6-10 2 cross-sections of the 6D operational window for the FEAT divertor. Only acceptable points within window and without neon seeding are shown. V1 is a slight modification of the V-out geometry.

2.7. NTM Suppression by ECCD

Optimisation of ECCD has been carried out[60] in frequency, poloidal (θ_p) and toroidal (θ_t) injection angle and injection position (defined by the poloidal angle χ_i) from the equatorial plane, solving ray-tracing and using the relativistic Fokker-Planck equation. The calculation has been carried out for ITER-FEAT-like parameters (R/a = 6.2 m/1.9 m, $n_{eo} = 1.17 \times 10^{20}$ m^{-3}, T_{eo} = 30 keV, Z_{eff} = 2) but with slightly higher B field (5.5 T). The density profile is assumed to be flat ($\sim(1-\psi/\psi_s)^{0.15}$) and the temperature profile is assumed to be parabolic ($\sim(1-\psi/\psi_s)$). Figure 2.7-1 shows that for off-axis current drive, optimal injection position is ~70 degrees, and the frequency is 180 GHz (~170 GHz for B=5.3T). Figure 2.7-2 shows the sensitivity to optimal toroidal injection angle, indicating the need for accurate control of injection angle. In this figure, at each frequency and each injection position, values for the toroidal and poloidal angles are chosen to have the maximum efficiency at a given radius ρ. The figure shows, for 190 GHz and for this angle χ_i =70°, the variation of these angles θ and the current density and efficiency, when the radius is varied. Other key points include:
(1) control of both poloidal and toroidal angles is essential for tangential resonance, which is the condition of optimisation;
(2) it is also essential to avoid the second harmonic resonance;
(3) estimated required power for stabilisation of NTM is several MW under the condition that the driven current is localised within 3% of minor radius from the optimised resonance point.

Modelling of modulated ECCD stabilisation of NTMs has been done for FEAT equilibria and the required EC power has been determined[61]. Equatorial and upper port launching has been considered. It has been shown that NTM detection in the early stage of evolution allows the requirements on EC power to be eased. A reasonable island size to be detected w/a=0.04 (w~10cm) allows the power required for stabilisation of both 3/2 and 2/1 NTMs to be reduced from 28 to 18MW for upper launching and from 35 to 22MW for equatorial launching. For small islands the polarisation current term in Rutherford's equation is essential, so an accurate model for this term is desirable.

Theoretical investigation[62] of NTM suppression has shown recently that the polarisation current is stabilising not only for subdrift island propagating in the ion drift direction ($0< \omega/\omega_{*i} < 1$) but also for islands propagating in the electron drift direction with a sufficiently low rotation velocity($0< -\omega/\omega_{*i} < k^*$~0.118).

Clearly, some experimental verification of models in present experiments is required, before a definite conclusion can be drawn with confidence.

[60] K. Hamamatsu, private communication and in preparation for publication.
[61] Zvonkov(Kurchatov)
[62] Mikailovskii et al.(Kurchatov)

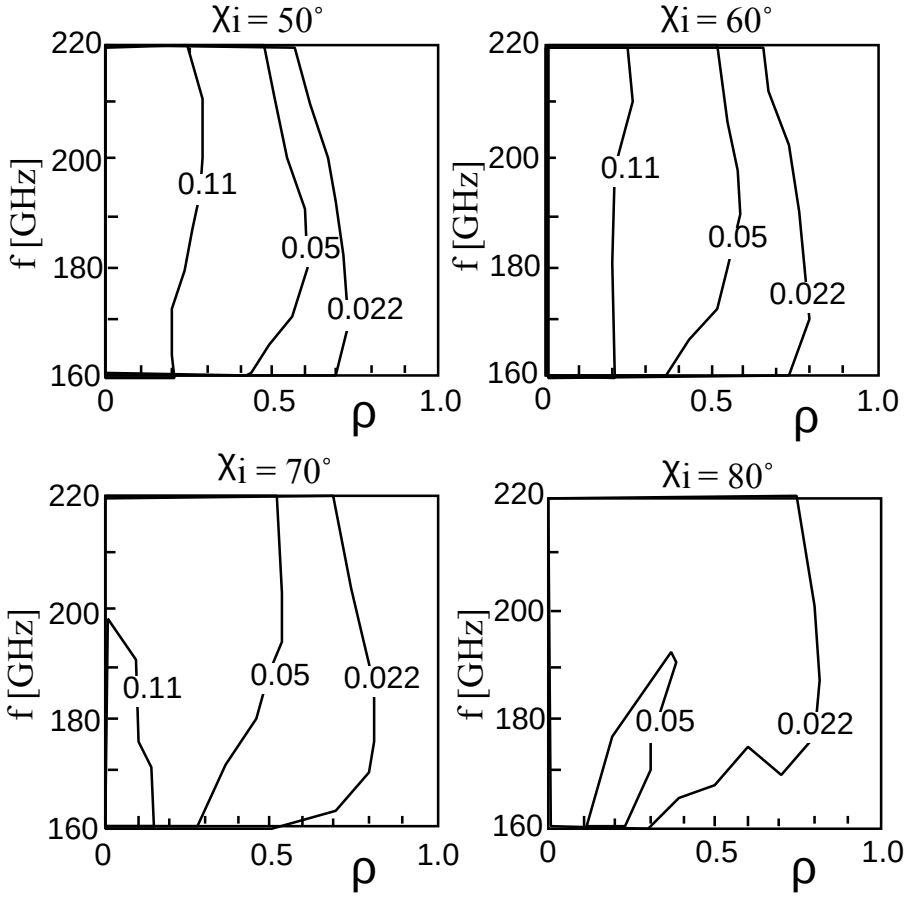

Figure 2.7-1 Contours of driven current density (in MA/m^2 per MW input) (frequency f vs. normalised radius ρ) for different poloidal injection angles χ_i.

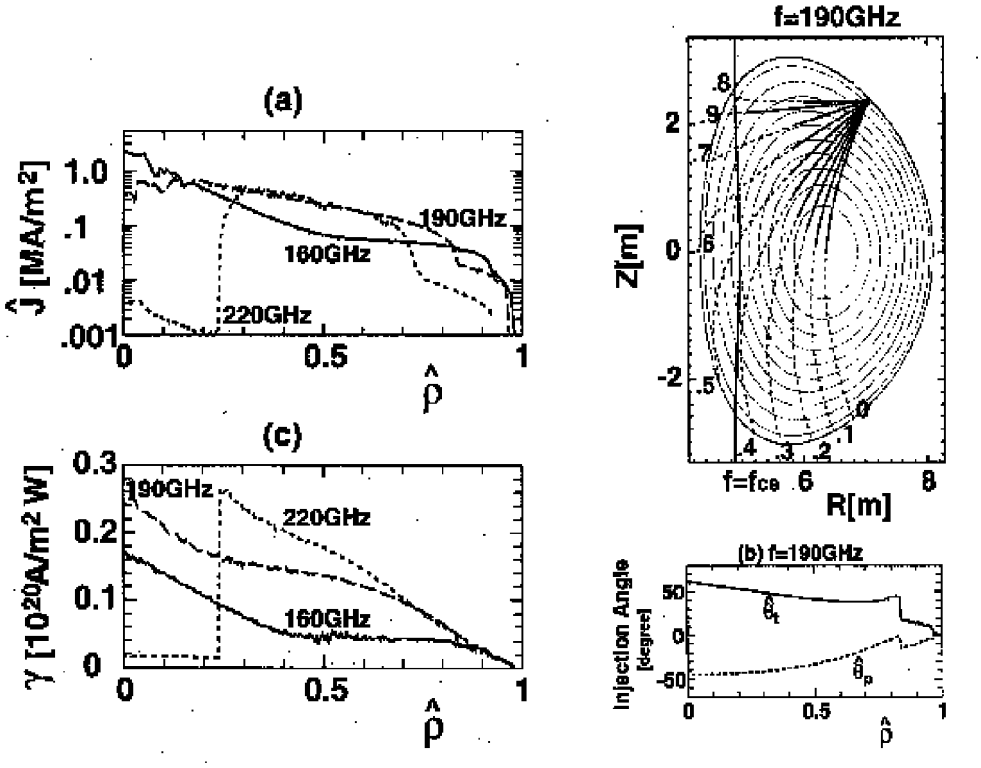

Figure 2.7-2 Current density per MW of injected power (a) with the optimum choice of injection angles, at one frequency (b) versus normalised radius. Global efficiency is shown in (c) for the same conditions

2.8. ITER Physics R&D

The projections of ITER performance require extrapolations from present experience and these must rest on established theory and experimental results from the leading laboratories, facilities and universities that together pursue the Parties' fusion science programmes.

The Parties undertake their Physics work for ITER on a voluntary basis outside of the framework of task assignments established for ITER Tasks in technology R&D and Design. Nonetheless the Parties' various efforts are undertaken in a structure designed to offer coherence and co-ordination of the voluntary contributions. An ITER Physics Committee comprising the Director and the Parties' designated persons for ITER Physics exercises oversight and is supported by seven Physics Expert Groups in the areas of

- Diagnostics
- Scrape-off-layer and Divertor Physics
- Edge and Pedestal Physics
- MHD, Disruption and Control
- Energetic Particles, Heating and Steady State Operation
- Transport and Internal Barrier Physics
- Confinement, Database and Modelling

Expert Groups meet up to twice a year and communicate their recent results to the ITER JCT, and they assist JCT via recommending physics basis and methodologies for physics design calculations to be used for ITER-FEAT. The results are reported to Physics Committee held once a year, and research priorities are determined from the perspective of addressing ITER-relevant problems most efficiently using the facilities and resources available to the Parties. Table 2.8-1 shows the Urgent and High-Priority Research Areas for the year 2000.

With the support and commitment of individuals and organisations throughout the Parties, this structure has proved to be extremely effective in providing the necessary physics support to the ITER design activities, the results of which have been published in the December 1999 edition of the Nuclear Fusion Journal. At the same time, ITER has proved a catalyst to general progress in tokamak physics through the discipline and focus required to identify and address efficiently the main challenges of establishing the ITER Physics Basis.

After the withdrawal of U.S. from ITER Expert Group activities, a decision was made in July 1999 at the Program Directors' Meeting to arrange as much as possible a 'pre-Meeting' or international workshop/conference, where generic issues will be discussed including the U.S. scientists, in conjunction with the Expert Group Meeting. Considerable efforts have been made successfully to involve U.S. scientists in voluntary physics activities by combining Expert Group Meetings with international meetings (U.S.-Japan Workshop, IAEA TCM, etc.).

Table 2.8-1 Urgent (Bold) and High Priority Physics Research Areas

Research Areas	Issues
Finite-β effects	**Tolerable ELMs (dW/W<2%) with good confinement alternate to type-I ELMs (e.g. type II, Type III+core confinement)** **Stabilisation of neoclassical islands** and recovery of ß
Plasma termination and halo currents	**Runaway electron currents: production and quenching, e.g. at low safety factor**
Sol and divertor	Achievement of high n_{sep} and relation of $n_{sep}/<n_e>$ in ELMy H-modes Carbone Chemical sputtering and deuterium retention/cleaning methods
Diagnostics	Determine requirements for q(r) and assess possible methods that can be applied to ITER Determine life-time of plasma facing mirrors and optical elements(incl. Those in divertor) Reassessment of measurement requirements in divertor region + recommendation of diagnostic techniques
Core confinement	Non dimensional scaling and identity experiments; effect of finite β and flow shear Determine dependence of τ_E upon shaping, density peaking etc.
Internal transport barrier properties	ITB power thresholds vs n, B, q, Te/Ti, Vrotation etc. for strong reversed shear (q_{min}> 3), moderate reversed shear(q_{min}> 2, and weak shear (q_{min}> 1).
H-mode power threshold	H-mode accessibility in ITER-FEAT , Data scatter
Density limit physics	Confinement degradation onset density; its dependence on aspect ratio, shape and neutral source
Pedestal physics	Scaling of pedestal properties and ELMs Effects of plasma shape on pedestal and ELMs

3. Magnets

3.1. Support of TF Coil Loads

3.1.1. Winding Pack Issues

Two options have been considered for the TF coil winding pack configuration:
- the radial plate design where the TF conductors use a thin circular jacket and are placed in spiral grooves machined on steel radial plates;
- the square conductor design where the conductor uses a thick-walled square jacket.

The advantages and drawbacks of these options are reviewed and the rationale for a choice is outlined.

Insulation

For both designs, radial plates and square conductors, the recommended procedure for the application of the conductor insulation is to follow the method used for the CS Model Coil. After heat treatment, the conductor is wrapped with insulation tapes (pre-impregnated glass and poliimide) and the insulation is cured. This allows a full visual inspection and voltage testing of the conductor insulation and gives a good guarantee that there is no pre-existent defect. The conductor is then either transferred to the radial plate or reformed into a double pancake. An insulating layer is then built up around each radial plate (or double pancake) and this assembly is filled with epoxy resin in a single impregnation step. The plates (or double pancakes) are bonded together to form a winding pack with ground insulation in a final impregnation step.

The radial plate and square conductor designs use therefore similar insulation manufacturing procedures. Even though the manufacturing procedures are similar, there are differences in the conductor geometry and operation conditions which give to the radial plate configuration major advantages in terms of the conductor insulation long term quality and reliability.

1) The jacket with a circular outer cross section is the optimum shape to apply the glass and poliimide insulation tapes. The result is an insulation which is uniform in thickness and also uniform in the relative glass/poliimide/epoxy content. This insulation is robust since it can contain a high density of glass and poliimide film.

2) During the magnet operation, the Lorentz forces acting on each conductor are transferred to the plate, without accumulation of forces on the conductor and its insulation. As a result, almost no primary load is applied to the conductor insulation and there is no degradation leading to damage due to mechanical cycling.

3) With circular conductors in radial plates, the insulation is not subject to the stress concentration effects which are always present at corners of square conductors.

4) With circular conductors in radial plates, delamination between the conductor insulation and the radial plate is of no consequence and has no impact on the mechanical behaviour of the winding pack.

In summary, the insulation of a circular conductor in radial plates is expected to be highly reliable. It is also expected to be very robust and able to easily stand the full coil ground voltage thus providing a second line of defense in the case of a ground insulation fault.

Another advantage of the radial plate configuration is that it provides a "double insulation" with two independent barriers and the capability to detect impending faults.

1) The conductor and ground insulations are independent and physically separated by the radial plate. It is therefore impossible for a single insulation fault to affect both conductor and ground insulations.
2) A single conductor insulation fault can be detected by monitoring the resistance between conductor and radial plate. In the event of such a fault, action taken before a second fault induces severe damage to the coil system.

The considerations above indicate that, with the radial plate design, faults internal to a TF coil and leading to coil damage are avoided by design.

There is, however, the possibility that faults external to a TF coil, for example at the TF coil terminal or along the coil feeders, may lead to a full coil short. The ITER design ensures that this type of fault does not occur: the TF coil terminals are separated by steel separator plates, and bus-conductors from one coil are routed in separate feeder tubes.

It can be concluded that, with radial plates, TF coil shorts are avoided by design. This is a very important statement in view of the severe thermal and mechanical damage induced by a TF coil short.

By contrast, the square conductor insulation is subject to large primary stress due to the in-plane and out-of-plane (cyclic) loads and to stress concentrations at corners of conductors. In particular, the square conductors show local tension regions in the insulation, which would cause local debonding at the corners extending in the worst case to about 20% of the jacket surface. With the square conductor design, the conductor and ground insulations are not separated and there is no possibility to detect impending faults in a TF coil. The occurrence of an insulation fault leading to significant damage cannot, therefore, be excluded.

Cost and radial build

Although the radial plates allow the use of a highly reliable turn insulation, they cannot be used without a cost penalty due to the radial plate manufacture and additional coil manufacturing steps to transfer conductors onto the plates. The cost difference between the radial plate and square conductor design options has been estimated using the 1998 ITER design unit costs. It has been found that the total TF coil cost with radial plates is about 8% more expensive than with square conductors when there is an identical radial build.

Some design and R&D activities have been requested in the EU and JA Home teams to study methods to reduce the manufacturing cost of the radial plates.

The radial plate design implies also a radial build penalty. The stress analysis of the TF coil inboard leg indicates that at similar stress levels in the case and radial plate (or square conductor jacket), the radial plate design requires a radial build which is 30 – 50 mm thicker than with square conductors.

Other considerations

Turn insulation voltage

With radial plates, each plate is connected (through a resistor) to the conductor cross-over. The turn insulation voltage is therefore 425 V for a coil terminal voltage of 5 kV. With square conductors, the turn to turn voltage is 35 v and the voltage between pancakes is 850 V.

The higher turn insulation voltage, in the case of the radial plate design, is not seen as a disadvantage in view of the high insulation reliability of this design.

Fast discharge and recool time:

- Radial plate design: In the event of a fast discharge of the TF system, eddy currents flow in the case and the radial plates. Heat conduction causes a quench of the superconductor after about 12 s. The radial plate temperature rises to about 60K and the conductor temperature to ~ 40 - 60K. During such an event, the helium in the TF coils is expelled and is collected in a cold (LN2 temperature) pressure vessel (volume of about 1800 m^3 and pressure of 1.8 MPa). Recooling and recharge of the TF magnet is expected to take less than 2 days.

- Square conductor design: In this case, the TF coil case temperature rises but this is not expected to cause a conductor quench. Recooling of the case is expected to take about half a day.

- Fast discharges are expected to be very infrequent and the difference in time to recool the magnet is not considered as a significant element in the choice.

Conclusions

The evaluation of the two winding pack configurations requires a balanced judgement between considerations of totally different nature such as insulation quality, radial build, cost, etc..

This judgement is therefore somewhat subjective since it critically depends on the weight and priority given certain aspects of the design.

Considering that insulation faults are the most probable cause of magnet failure and considering the difficulties involved in the replacement of a TF coil in ITER, the considerations on insulation reliability during operation have been given a high, overriding, priority over other considerations. This is the basis for the use of radial plates in the ITER TF coils.

3.1.2. Wedged support at the TF coil inboard legs

All along their inboard legs, the coil cases are wedged over their full radial thickness. About half of the centring force is reacted through the winding pack part of the coil, while the other half is reacted by the case.

The wedging surfaces must be accurately matched to achieve the required magnetic alignment and reduce stress peaks under the large wedging pressure. Precision machining of the wedging surfaces will be required as well as accurate surveying techniques to verify that deviations from the theoretical shape are within allowed limits.

Machining will ensure that deviations from flatness involve only long wavelengths and do not result in localized peak stress. Systematic errors, in particular on the wedge angle, could result in significant stress intensification and must be kept within tolerable limits, if necessary by using shims. Insulating shims are, in any case, necessary to avoid eddy currents flowing between adjacent coils. Analysis is underway to evaluate the effects of dimensional deviations and specify the acceptable range of tolerances.

It is assumed that the TF coil cases will be finish machined, surveyed and fitted with insulated shims before delivery.

3.1.3. Intercoil Structure Redesign

The main design driver for the inner intercoil structure (which is situated immediately above and below the inner straight leg of the TF coils) has been the requirement to achieve acceptable tensile stresses in the curved part of the coil in these regions. The allowable stresses are driven by cyclic fatigue considerations and, depending on the case material, fabrication history and welding procedures, are expected to be in the range 450-500MPa. Although the outer intercoil structure (forming four toroidal bands around the outboard curved regions of the coil) has only a small influence on the stresses in the inner curved region (due to the relatively high flexibility of the coils), the configuration of the inner intercoil structure can have a significant impact on the load conditions of the outer intercoil structures.

Many configurations of inner intercoil structure have been analysed with a detailed finite element model but the only one that gives acceptable stresses in the coil case, combined with an acceptable stress distribution within the structure (and especially the keys/bolts associated with the structure), is a set of poloidal keys between the coils. The intercoil structure itself is absorbed into the coil case, so that (at least at assembly) the wedged region of the coils extends into the curved regions by a thickening of the toroidal width of each coil case. The keys run in between the coils in these curved regions, normal to the coil centreline, extending to the inner (plasma facing) surface. A set of three or four in the poloidal direction appears adequate. The keys provide full support between the coils and prevent the development of torsion of the case which can make a large contribution to the case tensile stresses. At the same time, the flexibility of the case in bending gives a uniform poloidal distribution of load on the 3 or 4 keys. The poloidal keys are shown in Figure3.1-1.

In this curved region away from the central vault, the coil cases tend to separate on charging due to the overall expansion of the coil. The radial movement is small compared to the radial outward movement at the outer equator but is still sufficient to create an extra toroidal gap of about 0.5 mm between key and key slot. During plasma operation, the shear loads acting on the keys increase this gap to more than 1 mm. Key shapes which can tolerate this sort of "breathing" without losing contact have to be square or rectangular and produce high stress concentrations in the keyways. Detailed evaluations of the key and key slot stresses are still underway but at present the preferred solution is to use circular cross-section keys. The shear

loads acting on these create an extra de-wedging force which increases the gap between key and slot to more than 1mm. It is intended to suppress the breathing movement plus the extra de-wedging force by an upper and lower precompression ring. This ring is attached to each TF coil (and therefore requires eddy current barriers) in the upper and lower curved regions and is put into tension on assembly. The TF coils are therefore put into toroidal compression in the upper and lower curved regions (effectively, the wedged region of the central vault is extended above and below the inner straight leg) and toroidal separation in the key region is much reduced. The impact of the ring is summarised in Table 3.1-1 and 3.1-2

Table 3.1-1 Peak Tensile Stresses in the TF Coil Case

	Maximum Tensile Stress MPa	Min/Max Stress (R value)	Allowable Stress (LEFM with fixed initial defect - MPa)
With Ring			
Bottom of straight leg	516	0.65	560
In front of first key	342	0.42	440
Without Ring			
Bottom of straight leg	493	0.58	520
In front of first key	439	0.38	425

Table 3.1-2 Maximum Poloidal Key Shear Loads (4 Keys) in MN

	First Key (nearest inner leg)	Last Key
With Ring	16.2	14.4
Without Ring	19.5	14.7

To be effective, these precompression rings need to have a significantly lower elastic modulus than that of the case, so that the precompression is not sensitive to assembly tolerances. A thermal contraction coefficient larger than that of the case is also advantageous. The space available for the precompression rings between the CS and the inner PF coils is limited and a material that can provide the necessary hoop force within that space is a unidirectional glass fibre-epoxy composite. Any solution based on metallic materials would require a much larger (almost a factor of two larger) cross-sectional area than the glass fibre solution: aluminium wound as strips would offer the required elasticity and higher thermal contraction. The rings need to be placed close to the curved part of the coil, as extensive flange connections tends to rapidly reduce the effectiveness of the rings due to the flexibility of the flanges. The precompression is applied by tightening radial bolts between ring and the back of the coil case in the upper and lower curved regions (see Figure 3.1-1). The stresses in the rings are dominated by the precompression at room temperature. The material is stronger at 4K and there are no significant extra stresses due to out-of-plane movement of the TF coils (this is very small as the rings are close to the poloidal shear keys that restrain any coil rotation.

Table 3.1-3 summarises the main requirements for the rings for two of the most promising materials. On the basis of this, glass fibre is selected as the reference.

Table 3.1-3 Stresses in Precompression Rings at RT

Material	Allowable RT Tensile stress MPa	Cross-sectional Area of Ring m^2	Radial Displace-ment to Apply Precompression mm
Glass fibre	650	0.22	10
Aluminium Alloy	250	0.34	30

The use of the precompression rings has a significant impact on the outer intercoil structures (OIS) due to the changes in the radial expansion of the outer coil leg under the magnetic loads. It appears that the upper and lower structure rings are practically redundant. The poloidal keys carry the out-of-plane loads previously carried by the upper and lower OIS and the precompression rings cause the hoop tension (previously cause by the radial expansion of the coil) to drop to zero. The upper and lower OIS are maintained because they are used for coil positioning during assembly but they have no structural function (although the TF coil radial expansion creates significant key loads in these upper and lower OIS sections). Their extent can be reduced and their poloidal position can be flexible.

The outer intercoil structures directly above and below the equator are still requred to support the out-of-plane forces on the outer part of the coil, and the out-of-plane loads are not much affected by the inner intercoil structures. However, the precompression rings cause a significant reduction (by a factor of more than 3) in the hoop tension carried by these structures due to the radial expansion of the coil cases. The key loads are summarised in the Table 3.1-4.

Table 3.1-4 Tensile (Toroidal) Bolt Loads on the Equatorial OIS Sections in MN

	Upper Equatorial OIS	Lower Equatorial OIS
With Rings	7.9	1.9
Without Rings	22.8	17.7

The poloidal extent of the two equatorial OIS belts is determined by the out-of-plane loads and cannot be much reduced. There is some flexibility to position the belts to suit the requirements of the equatorial access gaps. A further major constraint on the design arises from the requirement for access to the vacuum vessel gravity supports (which connect to the TF coil cases) during assembly. The supports are placed behind the lower equatorial OIS ring and, in previous designs of this ring, are inaccessible once the ring is in place. The access requirement for the vacuum vessel supports has resulted in the choice of a "friction joint" type of OIS. This OIS is assembled after the TF coils (and the vacuum vessel supports) have been installed, by welding to the TF coil case on each side. The use of the inner precompression ring has reduced the toroidal load requirements on the equatorial OIS belts and the designs are now being reassessed to see if a prewelded and keyed/bolted box structure (with a removable central part to allow access to the vacuum vessel supports) can provide adequate out-of-plane support, eliminating in-situ welding.

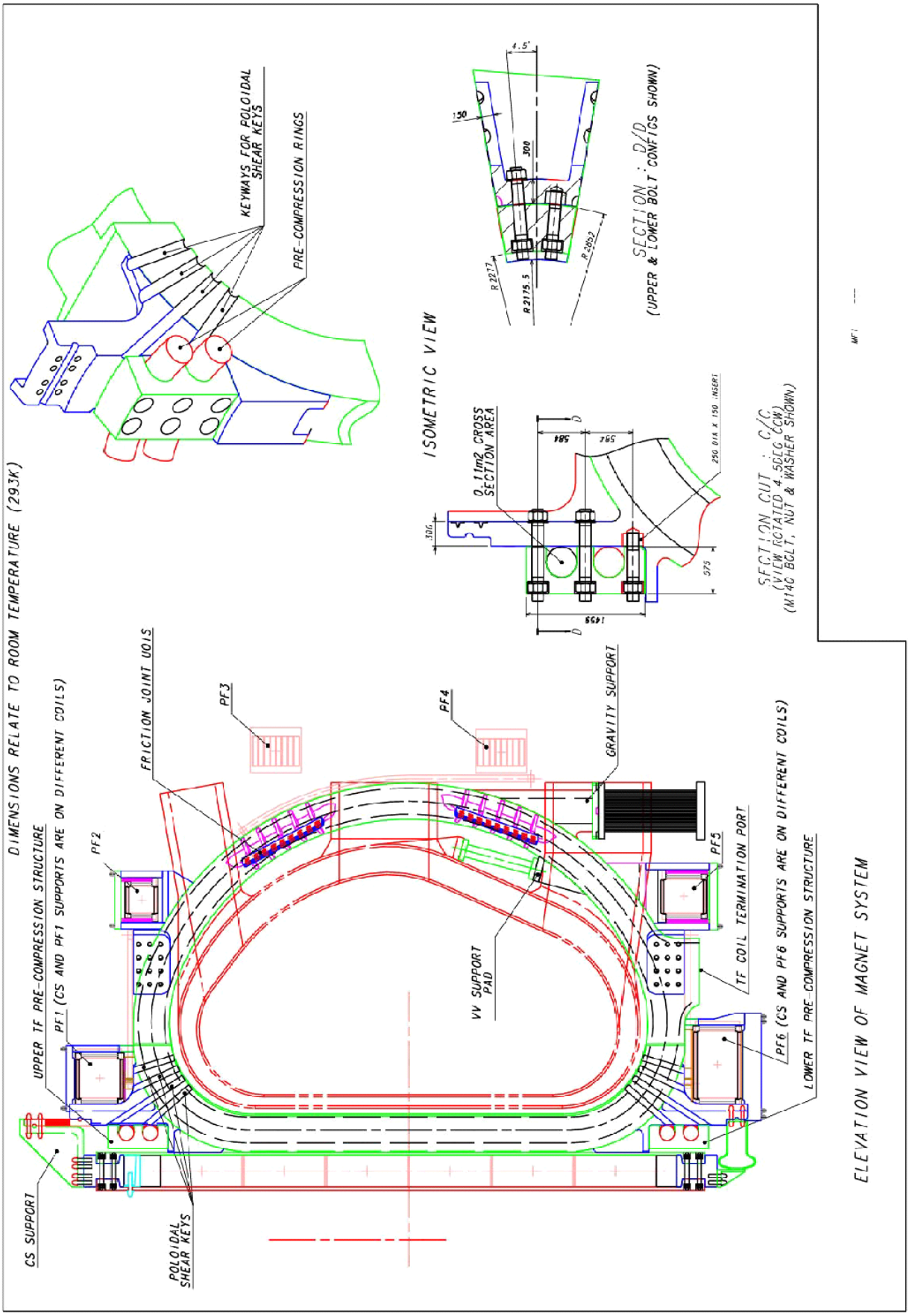
ELEVATION VIEW OF MAGNET SYSTEM
DIMENSIONS RELATE TO ROOM TEMPERATURE (293K)
UPPER TF PRE-COMPRESSION STRUCTURE
PF1 (CS AND PF1 SUPPORTS ARE ON DIFFERENT COILS)
LOWER TF PRE-COMPRESSION STRUCTURE
PF6 (CS AND PF6 SUPPORTS ARE ON DIFFERENT COILS)
PF2
PF3
PF4
PF5
FRICTION JOINT UOIS
GRAVITY SUPPORT
VV SUPPORT PAD
TF COIL TERMINATION PORT
CS SUPPORT
POLOIDAL SHEAR KEYS
ISOMETRIC VIEW
KEYWAYS FOR POLOIDAL SHEAR KEYS
PRE-COMPRESSION RINGS
SECTION : D/D
(UPPER & LOWER BOLT CONFIGS SHOWN)
SECTION CUT : C/C
(VIEW ROTATED 4.5DEG CCW)
(M140 BOLT, NUT & WASHER SHOWN)
0.1m2 CROSS SECTION AREA

Figure 3.1-1

3.2. Inductive Flux Generation

3.2.1. Choice of CS Jacket Material

The main function driving the design of the central solenoid is the generation of inductive flux to ramp up and maintain the plasma current. Flux generation in the solenoid is improved by:

(i) the choice of a maximum field compatible with the variation of the superconducting strand current density with field

(ii the use of the highest allowable tensile stresses in the jacket material

The requirements for the CS conductor jacket material in the FEAT ITER are primarily a high fatigue resistance to stress cycling. The jacket material can also affect the performance of Nb_3Sn superconductor due to differential contraction with the strands from the heat treatment temperature. This is a significant factor but not the main reason for choosing a jacket material.

Fatigue resistance can be assessed based on one of two procedures.

a) Fatigue life (S-N curves) measurements for the jacket, both base metal and weld

b) Linear Elastic Fracture Mechanics (LEFM) which requires the definition of an 'initial defect' and measurement of the material fatigue crack growth rate (FCGR). The initial defect is usually taken as the smallest defect that can be reliably detected in the material and welds during the fabrication inspections.

As indicated in the ODR, there are two basic design options for the CS jacket.

1. The use of an extruded jacket with a square outer section where the structural material goes through the Nb_3Sn heat treatment. The possible jacket materials are Incoloy 908, as developed for the CS Model Coil, or a ‘modified’ stainless steel if such a steel can be developed to meet the fatigue life requirements after heat treatment.
2. A double armour option involving the use of an inner titanium circular jacket (which undergoes the Nb_3Sn heat treatment and which matches the thermal contraction of the Nb3Sn) reinforced by two outer U-channels which are applied after the heat treatment of the conductor. In this case, the steel can be selected for optimum mechanical properties, without consideration of the degradation caused in steel by the heat treatment.

In the case of option 1 above, the possible jacket materials are Incoloy 908 and a 'modified' SS.

The problems of Incoloy 908 are well known:

a) it is highly sensitive to stress accelerated grain boundary oxidation (SAGBO) during the Nb_3Sn heat treatment, which requires very strict control of the heat treatment atmosphere (O_2<0.1 ppm)

b the welding procedure was not adequately developed by USHT in the EDA period. The welds suffer from local hot cracking due to Nb precipitation with multi-pass welding. The effect on fatigue is unknown but presumably not acceptable. A possible solution was identified towards the end of the EDA by USHT, using a low-Nb weld wire. This wire was never qualified by USHT but this work is now being undertaken by EUHT. (recent results indicate that the new wire solves the hot cracking issue).

There are two significant advantages of Incoloy. It is a precipitation hardened superalloy with (in the base metal) a very high fatigue resistance, and the thermal contraction matches Nb_3Sn. It was selected for the ITER CS reference on the basis that the weld problems can be solved and that process for heat treatment of Incoloy has been well established in the CSMC fabrication. Difficulties have been encountered by the EU in the heat treatment of an Incoloy pancake. This occurred with a thin circular TF jacket (not the CS square type) and the heat treatment was performed in an oven well outside the ITER specification.

The 'stainless steel' issues are less clear because 'stainless steel' is a generic term and does not define either the specific alloys required to withstand the Nb_3Sn heat treatment without embrittlement due to carbide precipitation, or those that have good cryogenic properties. For example, the JK2 proposed as the material for the second ITER reference option is a stainless steel that cannot withstand the Nb_3Sn heat treatment and which has a coefficient of thermal contraction close to Nb_3Sn between room temperature and 4K. As a result of R&D in EU and JA, several steels are known which seem to withstand the heat treatment without degradation of properties. The EU has manufactured 3 variants (all low carbon, high nitrogen modifications of the standard 316LN), one from Boehler, one from Valinox and one from Sandvik.

The measured FCGR (fatigue crack growth rate) performance of the Boehler and Valinox steels is extremely poor, about x5 higher than usually expected for high quality stainless steel (and x5 higher than measured for JK2). This may be due to the poor quality level of these steels (no electroslag refining) but this is not known definitely. The most recent supply, from Sandvik, was used for the TFMC. The EU has a task agreement (since 1996) which includes the fatigue characterisation (S-N and FCGR) of this steel but this has never been performed.

For fatigue life assessments based on FCGR, the assumed initial defect size is critical. The selection of an initial defect for use in an LEFM assessment is not only based on what can be 'seen' in an X-ray photograph but also on what is present, determined by destructive sectioning, and cannot be seen. The EU has referred to defect sizes of 0.1 mm ‘detected’ during the fabrication of CS coil jackets. However, it is known from subsequent investigations on the CSMC jackets that defects were present that were not detected by inspections but later became visible after winding operations. The defect size stated by the EUHT of 0.1 mm is not much larger than the material grain size (0.04 mm) and is unlikely to be supportable in a proper qualification procedure.

The use of realistic defects sizes (the JCT reference value is 0.5 mm^2 for a crack area) together with the available FCGR data for Boehler and Valinox steels would lead to an unacceptable CS design. Not only are the allowable stresses low (about 300 MPa compared to 400 MPa for Incoloy 908) but the thermal contraction coefficient causes degradation of the Nb_3Sn properties. In addition, the use of a steel jacket reduces the vertical precompression that can be applied to the CS and may bring some limitation in achievable plasma shaping.

Alternative fatigue assessment procedures (S-N curves) may be appropriate for application to the jacket welds as they can take into account the stress cycles needed to initiate a crack from a defect. At present this is not possible as almost no data is available for any of the 3 EU steels, base metal or weld (and generally S-N data for austenitic stainless steels at low temperature is very limited. It is not certain that this alternative procedure would allow higher

operating stresses as conventional safety factors with fatigue life predictions are higher than with FCGR-based predictions.

The JCT action in this situation has been as follows:

a) select Incoloy 908 as the provisional reference solution and Ti- stainless steel (JK2, without heat treatment) as an alternative solution;
b) try to establish with JAHT task agreements to demonstrate the JK2 fatigue properties and establish the Ti-JK2 fabrication route (the application of U channels after heat treatment is a complicated process);
c) place a task agreement with EUHT to provide S-N data on Valinox base and weld metal;
d) try to establish another task agreement with EUHT to manufacture and qualify a steel variant properly optimised for good fatigue performance after Nb_3Sn heat treatment.

3.2.2. Choice of the CS conductor cross-section: rectangular or square jackets

The qualitative reasons for choosing square CS conductors have been presented both to the Concept Improvement and Design Integration Task Forces in 1999 and to TAC. In view of the comments received from the EUHT on the possible use of rectangular conductors, this has now been quantified, confirming the original JCT judgment.

Stress Analysis

It is clear from simple geometric considerations that a vertically elongated jacket will provide better support to the vertical forces (for the same jacket area) than a square one. However, the difference between the two jacket configurations become negligibly small in the case of the CS winding pack because of the large fraction of structural material which is required to support the hoop stress.

The JCT has performed a stress analysis, using two CS winding packs with identical structural material fractions. One winding pack has the reference square conductor plus co-wound strip, the other has a rectangular conductor with an aspect ratio of 2.5 plus cowound strip. The results are given in the table.

	Toroidal Hoop Stress MPa	Tresca Stress MPa	Vertical Stress MPa
Stress Limits	*400*	*867*	*N.A.*
Square Conductor	392	546	-302
Rectangular Conductor	395	476	-269

The toroidal hoop stress is almost identical to the maximum principal tensile stress as it occurs on the inner surface of the jacket where the shear stress is zero. The cross-section of structural material in the CS conductor is determined by mechanical fatigue which depends on the toroidal hoop stress. The rectangular conductor design does not present any advantage in this respect.

Cable Performance and Supporting Data

Conductors with a rectangular cable will not achieve higher current densities than conductors with a circular cable unless the final substage wrap of inconel foil (used to control AC losses) is omitted.

Based on present knowledge, the following comments can be made on such rectangular cables.

a) AC losses would be unacceptable without an Inconel wrap. Although the rectangular shape helps reduce AC losses due to field changes parallel to the long side, the rectangular shape also gives a better contact between the final cable units than the circular shape with units arranged around a central hole.
b) The AC losses of cables with substage wraps are dominated by the last but one substage and the shape (rectangular or circular) has almost no impact.
c) Because of the different cable contact distribution and AC loss behaviour, the use of a rectangular conductor would require the AC loss characterisation work to be repeated.
d) When submitted to transverse changing fields, the round shape offers symmetry and hence the best conditions to provide uniform current distribution among sub-cables and strands. Predictive analysis of non-uniform current distributions and their effects on conductor performance is difficult and is more likely to be successful when applied to a symmetrical configuration.
e) The circular cable can be produced with a minimum size hole in the centre for short unit lengths. For coils with long unit lengths that require a greater cooling flow, the hole diameter can easily be increased without changing the cable concept.

Joints

It has been claimed that a rectangular conductor joint in the CS occupies less radial space than the square. This claim seems to be based on the assumptions that the joint is an overlap type, that the toroidal length in each case is the same, and that the top or bottom side of the conductor (the narrow side for the rectangular) is used as the contact surface.

Two comments can be made on this question.

a) For the same circumferential length of the joint, a rectangular conductor has a lower contact resistance area than a circular. This reduction in area has a very significant impact on the current distribution into the individual strands, as fewer of them come into contact with the copper sole plate of the joint. The rectangular joint could be made longer but this has a drastic impact on the joint AC losses in the CS.
b) If a rectangular joint with lower contact surface area is acceptable, the circular cable can be given a similar shape locally in the joint region. The overall compaction of the cable in the joint gives vertical space for such an adjustment.

Manufacture

The selection of a circular cross section for the cable was made at the beginning of EDA. Advantages in the manufacture of the cable and the jacketing process were important reasons of that choice.

- A circular cable is made of typically 6 identical sub-cables in a symmetrical configuration. This geometry minimizes the amount of deformation of the sub-cables

during the production of the cable and during the subsequent jacketing operation. As a result strand damage is also minimized.

- It has been verified that a circular cable can be pulled through a seamless jacket which has been fully inspected (X-ray, liquid penetrant, ..) and leak tested before the insertion of the cable. This gives the best guarantee of the jacket quality.

By contrast, rectangular conductors require a large deformation of the cable which probably sets an undesirable lower limit to the void fraction. It is not clear if a rectangular cable can be pulled through the jacket as cable torsion can create extra friction. The jacket is also subject to large cold work deformation especially at the corners and may not be able to be produced as seamless tubing.

Overall R&D Database

The entire conductor and magnet R&D effort of all ITER Parties since 1992 has been focused on circular conductors. The development has covered all aspects of conductor manufacture (cabling, jacketing) and performance evaluation (AC losses, short sample and joint performance) and culminates now in integrated performance testing of model coils. The circular conductor concept is common to all ITER coils (TF, CS and PF).
The use of a rectangular conductor would require to repeat many items of this development. It would also convey the message that EDA R&D has not been useful.

3.2.3. CS manufacture and compression structure and supports

The CS is pancake wound. In the current design, a single conductor length of 820 m is adequate for six pancakes. This “hexa-pancake” winding arrangement minimizes the number of joints at the outer diameter and, therefore, it reduces the complication associated with the joint configuration which includes the joint itself with its mechanical clamps, the helium pipes and the tie plates which carry the mechanical hoop tension. These components must fit in a narrow space between the CS and TF coils. On the other hand, this configuration requires more complicated manufacturing processes and tools, in particular for the winding of a conductor when the winding starts from the outer diameter. A preliminary study on the CS manufacture has been performed by industry and indicated a possible process to make hexa-pancakes with some conceptual design of tooling. The design of the cooling inlets at the high field cross-over point of each pancake is another issue that requires R&D to resolve. The use of the hexa-pancakes makes positioning of prepared jacket penetrations (formed before the cable is put in the jacket) very difficult, and forming them in-situ is complicated, with potential for strand damage and the introduction of weld defects. A more conventional double pancake winding is of course possible and is kept as a backup option, but it requires three times as many joints.

The CS consists of a stack of six electrically independent modules. The field curvature at the ends of the CS creates vertical forces on the modules. At IM (initial magnetization) and EOB (end of burn), these forces are towards the centre of the stack, whereas at some intermediate equilibrium configurations the end modules carry opposite currents to the central ones and are repelled. This means that a vertical support structure is required. This structure applies axial pre-compression to the coil stack so that the modules remain in contact during all operating conditions. To obtain uniform compression, tie plates running axially along the CS are provided at both inside and outside diameters and connect to pressure plates at top and bottom. This structure is designed so that it can restrain the maximum vertical separating load

of 75 MN acting on the end modules of the stack. The required axial tension in the structure is achieved partly by pretensioning at room temperature and partly by differential contraction during cool-down. This requires a jacket material of the CS conductor with a lower contraction coefficient than the tie plates which use stainless steel.

The whole CS stack is hung from the top of the TF coils through the precompression structure. The top supports consists of flexible plates which provide axial and toroidal registration of the CS but allow relative radial motion between the CS and the TF coils. At the bottom of the CS stack, springs provide a radial centering force.

3.3. Conductor Design Issues

3.3.1. Current Non-Uniformity

It is now widely recognised that the current in a cable made of parallel-connected strands is most unlikely to be uniformly distributed in each strand. The non-uniformity can be driven by resistive variations in the strands at the joints, or by inductive coupling variations between strands along the cable length. Transition between these two drivers is controlled by the time constant of circulating currents in the cable, which is of the order of 1000 to 10000s. In the ITER coils, the CS and PF coils are expected to have inductance-dominated current distributions and the TF to have resistance-dominated.

Current non-uniformity is not a problem in itself: only if it leads to degradation of the thermal stability level of the cable does it need to be avoided. In some coils (which are not typical of the ITER coil design), current non-uniformity has caused such phenomena as the 'ramp rate limit'. The ITER coils have various levels of current uniformity control:

- The cables are designed to be fully transposed with the strands in predictable positions around a central annulus, so that a uniform inductance can be expected.
- The joints are designed to give uniform contact resistances at the level of the final substage (one sixth of the cable, with about 150-200 strands). This avoids gross mal-distribution in the cable and is within the current capability of joint manufacturing technology to achieve. Current non-uniformity is dominated by current variations within the strands of each of the final subunits.
- The cables have a minimum level of transverse conductance between the strands in each of the final substages. This conductance has to be carefully controlled through the cable void fraction (and hence through the jacket manufacturing tolerances). Too high a conductance leads to a high AC loss, too low and fast current redistribution of current during thermal disturbances cannot occur.

The CSMC was designed to test the impact of both resistive and inductive current distributions in full-size ITER cables. The results so far (including steady and pulse tests of the main module up to 13T) show no sign of any performance degradation due to current non-uniformity. Numerical analysis of current non-uniformity is also being developed and verifies the ITER choice of design criteria (these criteria, updated from the 1998 ITER design, were discussed and agreed in March 1998 at a meeting attended by all HTs, and will be included in the ITER FEAT FDR at the end of this year.

3.3.2. PF Conductor Design

The PF conductor design rationale has been presented to the HTs in recent working documents[63]. These contain a detailed discussion on the factors controlling the design of the PF conductors and the reason that three or four grades should be chosen (to reduce cost).

The PF conductors have been designed in accordance with the criteria agreed with all HT. The copper: non-copper ratio is derived from the usual combination of requirements from the limiting current (Stekly), temperature margin and hot spot criteria, and (to achieve the lowest cost, most compact cable design) all three limits are satisfied at the design point. The highest field conductor (PF1 and 6 under back-up conditions, at 6.4T and 4.7K) requires a low Cu:nonCu ratio of about 1.6. The performance of NbTi rapidly improves with lower field so that the Cu:nonCu ratio rises to 6.75 for the PF2,3 and 4 conductors at 4T and 5K.

3.4. Limits to Elongation/Triangularity

Several analyses[64] have shown that the strong reverse (negative) shear plasmas *("long pulse")* modelled in the recent RTO/RC ITER studies pose less demand on the vertical stabilization system than the nominal (positive) shear counterparts *("high current")*. In fact, although the plasma elongation (κ) is typically larger for the reverse shear equilibria, the vertical field decay index[65] is smaller than in the negative shear case[66]. Moreover, the reverse shear plasmas are better coupled with the passive stabilization structures. As a result, the stability margin (m) and growth time (τ_g) of the negative shear plasmas (see box) are, typically, 50-100% larger than in the positive shear equilibria[67]. Because of these facts the stabilization system is designed for the "the most demanding" positive shear plasma and - a posteriori - checked to ensure that the reverse shear plasma can indeed be stabilized by a feedback loop designed for the negative shear case[68]. It turns out that the positive shear, Start Of Flat-top (SOF) equilibrium is the most demanding equilibrium as far as vertical stabilization is concerned[69].

The "plasma disturbances" considered at present to test the performance of the vertical stabilization system *in normal operation condition* are already quite severe (e.g. $\delta l_i \approx -0.1\ l_{i,ref}$). In this respect, using internal coils to stabilize plasma equilibria in the presence of even larger disturbances would not be consistent with the assumptions made on the design of other systems for the normal operation condition (e. g. maximum divertor heat loads in normal operation[70]).

For the case of positive shear plasma equilibrium at Start Of Flattop, an increase in κ leads to

[63] Basic Design Package for Analysis (BDPA) 2000 version2, 6 March 2000
[64] Report of RTO/RC-ITER Concept Improvement Task Force, 2 July 1999, N A0 RI 99-07-19 F1.
A. Kavin, "Study of Reversed Shear Plasmas in ITER-FEAT", ITER Naka JWS, February 2000.
[65] Therefore also the de-stabilizing force from the applied quadrupole field.
[66] A. Portone, "Plasma shape control and vertical stability", Point Design Review Meeting, Naka, 13 October 1998.
[67] Report of RTO/RC-ITER Concept Improvement Task Force, 2 July 1999, N A0 RI 99-07-19 F1.
[68] A. Kavin, "Control of Plasma with Strong Reversed Shear", Design Task Review Meeting, ITER Garching JWS, 9-10 March 2000.
[69] ITER-FEAT Outline Design Report, January 2000.
[70] ITER-FEAT Outline Design Report, January 2000.

a reduction of stability margin and growth time. Studies[71] have shown that up to $\kappa_{95}\approx 1.7$ the outer PF coils can be used to control the plasma. For $\kappa_{95}>1.7$ (see Table 3.4-1 and Figure 3.4–1 and –2) the stability margin drops below $m\approx 0.4$, the growth time drops below $\tau_g\approx 80$ ms and internal control coils becomes essential to allow reliable plasma stabilization and to limit the installed power necessary for control[72]. Therefore *internal coils are essential for plasma control as soon as* $\kappa_{95}>1.7$. The question now is *how much we can increase* κ_{95} *by using internal coils for stabilization*. From Figure 3.4-1 it appears that above $\kappa_{95}\approx 1.8$ the stability margin drops below $m\approx 0.3$ and the growth time below $\tau_g \approx 50$ ms. For reliable vertical stabilization (reduction of disruption rate during operation[73]) *we assume as design criterion* $m>0.3$. To achieve $m\approx 0.3$ for $\kappa_{95}>1.8$ it is necessary to design the in-vessel components to increase their passive stabilization capability. This can be obtained[74], for example, by attaching copper strips to the blanket modules to allow eddy currents flow along low resistance paths close to the plasma[75].

The use of internal coils to improve plasma stabilization at high plasma triangularity (for the same elongation) is not justifiable, the maximum δ achievable being limited by the PF equilibrium currents (and cost) rather than by the vertical stabilization capability of the out-of-vessel as opposed to the in-vessel coils.

In conclusion therefore, above $\kappa 95\approx 1.7$ internal control coils are needed to allow prompt control at the cost of relatively low installed power (typically < 300 MVA). Above $\kappa 95\approx 1.8$ internal control coils must be aid by copper stabilizers in the blanket that improve passive stabilization (in the CDA, for example, twin loops allowed $\kappa 95\approx 2$). Therefore, the use of the internal control coils "per se" does not allow substantial increases in vertical elongation (≈ 5%). Larger increases of plasma elongation (for example[76], ≈ 20%) can be achieved only provided that the in-vessel components (in particular, the blanket) are designed to keep m > 0.3.

Table 3.4-1[77]

design	I_p(MA)	R_p(m)	a(m)	βp	l_i	$\kappa 95\%$	m	τ_g(ms)
IAM	13.3	6.20	1.90	0.10	0.85	1.66	0.47	95
HK1	13.4	6.02	1.86	0.10	0.85	1.76	0.36	66
HK2	13.4	5.85	1.81	0.10	0.85	1.86	0.20	31

[71] Report of RTO/RC-ITER Concept Improvement Task Force, 2 July 1999, N A0 RI 99-07-19 F1. ITER-FEAT Outline Design Report, January 2000.
[72] Report of RTO/RC-ITER Concept Improvement Task Force, 2 July 1999, N A0 RI 99-07-19 F1.
[73] J.B. Lister, et Al., "Stability Margins of Elongated Plasmas in TCV and Implications for ITER", 26th EPS Conference on Controlled Fusion and Plasma Physics, Maastricht, 1999, European Conference Abstracts, Vol. 23J (1999) 1073-1076.
[74] ITER Poloidal Field System, ITER Documentation Series, No. 27, IAEA, Vienna, 1991.
[75] Such current flow is always present on the "inductive time scale" and, strictly speaking, the stability margin - defined in terms of "inductive mode current distribution" - increases as a result of this. However, for the reference blanket modules, the eddy currents decay very quickly (<10ms) and are not useful in increasing the passive stabilization features of the metallic structures.
[76] ITER Poloidal Field System, ITER Documentation Series, No. 27, IAEA, Vienna, 1991.
[77] R. Albanese et Al., CREATE Report, 31 May 1999, Issue 2.

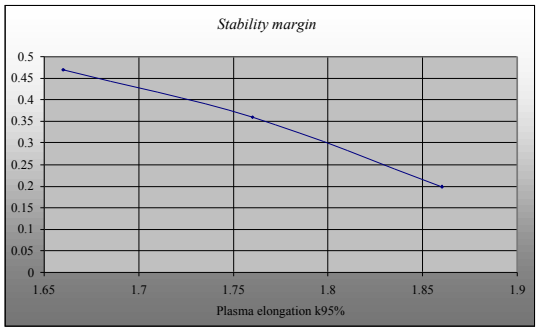

Figure 3.4-1 Stability margin vs. plasma elongation

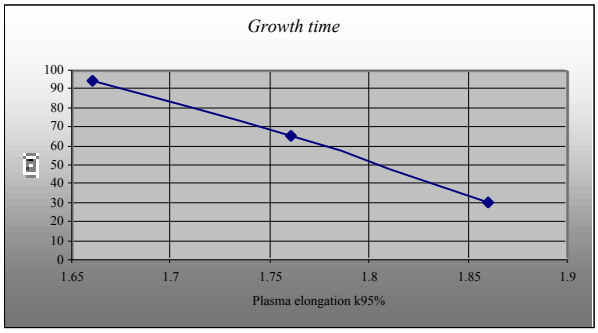

Figure 3.4-2 Instability growth time vs. plasma elongation

Stability margin and instability growth time

Background

The stability margin m is a measure of how far from the Alfven's unstable regime is the plasma equilibrium configuration under study. If m < 0 any perturbation to the plasma vertical position will grow on the μs-time scale related to the plasma inertia and the instability growth time τ_g will scale as $\tau_g \quad \sqrt{m_p/F_{dest}}$ where F_{dest} is the destabilizing force from the equilibrium field and m_p is the plasma mass. On the other hand, if m > 0 the growth time increases of several order of magnitude up to the ms time scale related to the L/R decay time of the image currents induced by any plasma displacement in the surrounding metallic structures and $\tau_g \quad m\ L/R$.

Discussion and conclusions

The stability margin m is defined as $m \equiv (F_{stab}^{ideal} / F_{dest}) - 1$ *where the stabilizing force acting on the plasma is given by the passive structures considered as ideally conducting. For the one-mode approximation to the eddy current distribution in the metallic structures and neglecting the plasma mass, the Kirchhoff's voltage law and the plasma momentum equation can be combined to give:*

$$m\tau_e\, dz/dt - z = 0 \qquad \tau_g = m\tau_e \tag{1}$$

where τ_e is the L/R decay time constant of the (one mode distribution) current in the passive structures. From (1) it follows that if the plasma parameters vary (for example, the plasma current density profile quantified by l_i) leading to a variation of the stability margin δm, the relative variation in the growth time $\delta\tau_g/\tau_g$ scales as:

$$\delta\tau_g / \tau_g = \delta m / m \tag{2}$$

To avoid that small variations in the (quite unpredictable) plasma current density profile may lead to large variations in the growth time and complications to the plasma stabilization, m should be "as large as possible" (see (2)).

In case of out-of-vessel control coils several studies[78] have shown that $m \approx 0.5$ and $\tau_g \approx 100$ ms lead to satisfactory control effort and robustness. Plasma variations up to $\delta m \approx -0.1$ (i.e. $m \approx 0.4$) leading to $\tau_g \approx 80$ ms are still controllable but with strong closed-loop degradation.

In case of in-vessel control coils the closed-loop system is more robust to plasma degradation. On the other hand[79], above $\kappa_{95} \approx 1.8$ m the stability margin drops below $m \approx 0.3$, the growth time drops (rapidly) below $\tau_g \approx 50$ ms and – more importantly – large relative variations ins τ_g may results from small variations in the plasma parameters. For example, at $m \approx 0.2$ an error of ≈ 5% in the quadrupole field due, for instance, to the limited accuracy of the PF coils current control system, the relative variation of growth time could be as large as $\delta\tau_g/\tau_g \approx 30\%$.

[78] Report of RTO/RC-ITER Concept Improvement Task Force, 2 July 1999, N A0 RI 99-07-19 F1.
[79] A. Portone, "Effects of Plasma Elongation on Vertical Stabilization Parameters", Plasma & Field Control Division, N 47 RI 29 99-05-14 F1, Naka JWS, 14 May 1999.

4. Vessel/In-Vessel

4.1. Manifolding of Blanket Coolant

The removal of the backplate has simplified the load assembly of ITER FEAT and reduced the inboard thickness with respect to the 1998 ITER design. Some functions, like the blanket module support and the plasma stabilisation, can only be transferred to the vessel. However, the supply of the coolant to the blanket modules can be achieved either by passages built inside the vessel wall or by separate ducts mounted between or behind the modules. Both solutions have been considered and their advantages and disadvantages have been presented[80].

To improve the leak detection procedure for the blanket requires an increase in the number of cooling manifolds to reduce the number of modules per parallel loop. The simplification of the double wall vessel and the ability to use standard welding techniques increases by removing many independent cooling passages. These facts, and recent design improvements, have led the separate manifolds to be now adopted as the reference design for ITER FEAT.

Inboard and outboard basic layout

In the inboard region (Figure 4.1-1), from the divertor cassette to the upper port opening, the blanket is segmented into 8 rows of 18 modules (toroidal span 20°) wedged towards the centre axis and covering the field joints. Since there are no gaps between the modules, the cooling manifolds are located in special grooves machined in the back of the modules. Behind each module there is an inlet and an outlet cooling manifold. The flexible branch pipes of the hydraulic connection are mounted between the manifolds over the 40 cm space. The single curvature plane manifolds are 20 cm either side of the field joint of the vacuum vessel, for 9 modules out of 18.

In the outboard region, from the upper port to the divertor port, the blanket is segmented into 9 rows of 36 modules (toroidal span 10° apart the port regions). The modules are rectangular parallelepipeds for assembly reasons which leaves triangular voids between the modules. The cooling manifolds are located in these voids and act as filler shield. Often they need more space than available (2-10 cm width increasing from the first wall towards the vessel) and cut outs are needed in the corner of the modules. Toroidally alternate manifolds are used for coolant inlet and outlet.

[80] Technical basis for the ITER-FEAT Outline Design , G A0 RI 2 00-01-18 R1.0 Section II.2.2

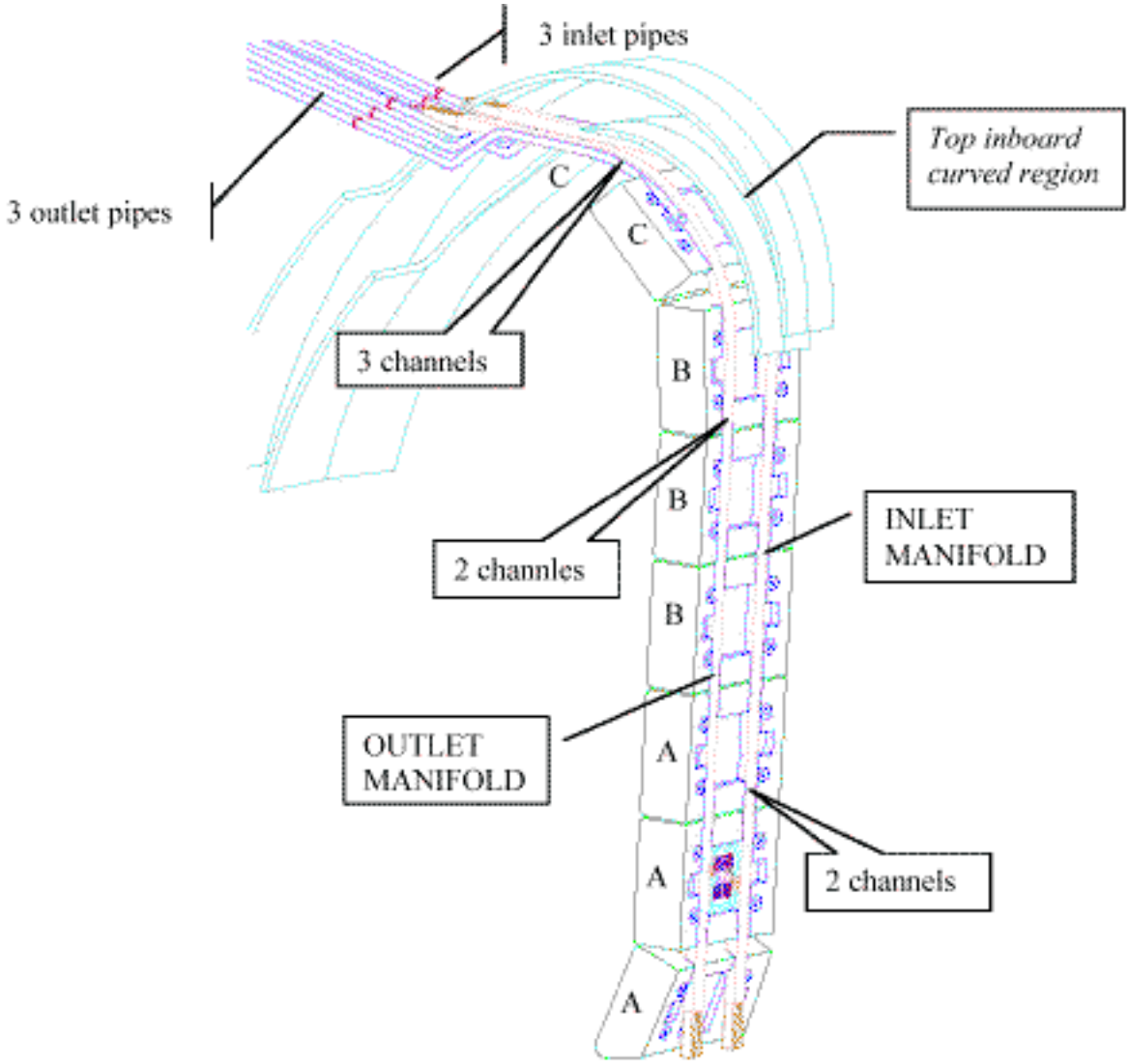

Figure 4.1 -1 – Cooling manifolds for inboard blanket, typical 20° sector.
(see also the cross section in Figure 4.1-4)

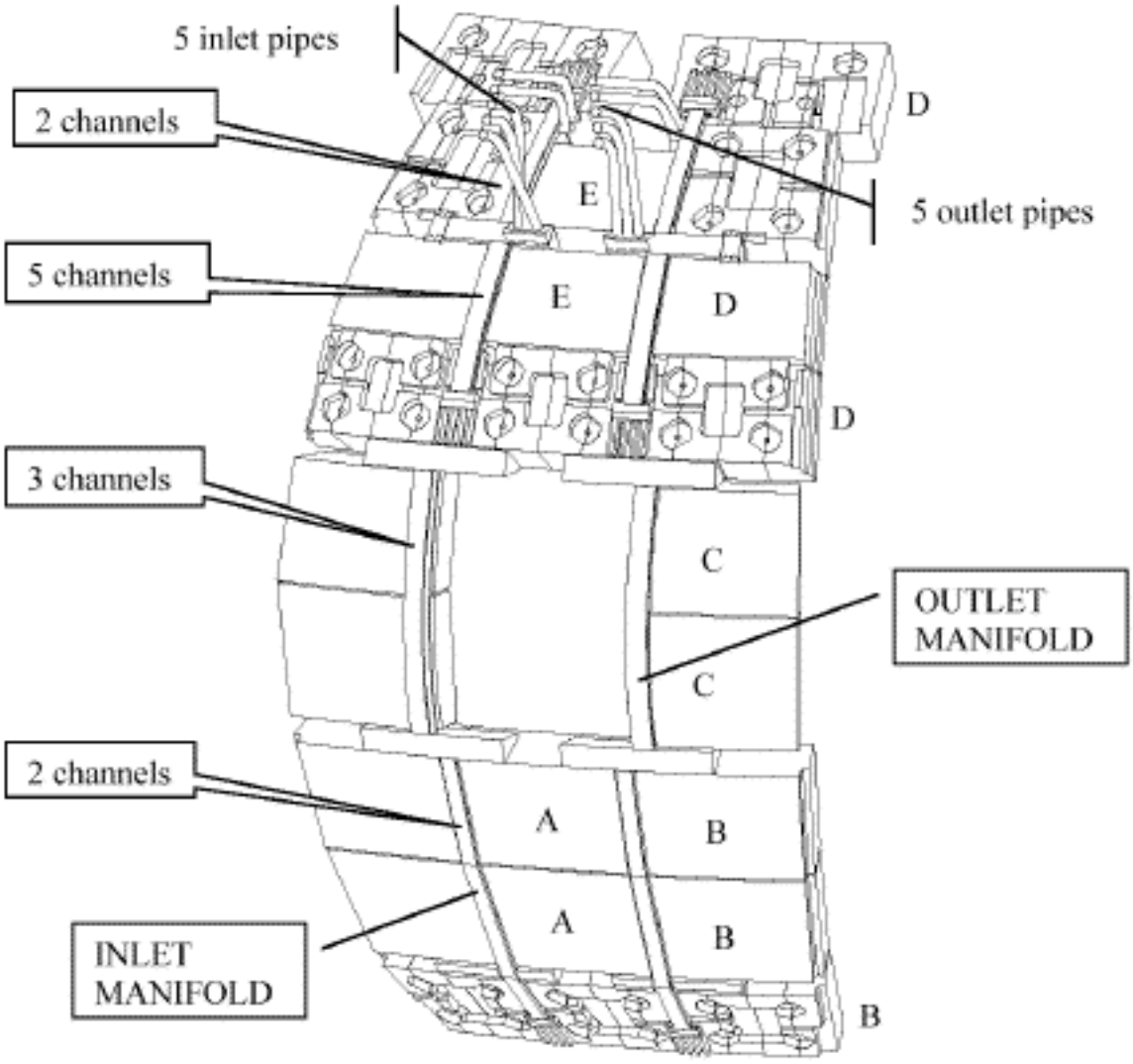

Figure 4.1-2 – Cooling manifolds for outboard blanket, 20° periodic arrangement
(see manifold cross sections in Figure 4.1-9)

Multiple loops per circuit
Each inboard manifold includes 3 independent cooling passages feeding separately the 8 modules in groups of 3-3-2, from the bottom up (see positions A, B and C in Figure 4.1-1).

Each outboard manifold includes 5 independent cooling passages feeding separately the 15 modules in groups of (see positions in Figure 4.1-2):
3-3, below the equatorial ports: centre (A) and adjacent (B)
2, between the equatorial port (C)
3-4, above the equatorial port: centre (E) and adjacent (D), including the module in between the upper ports.

The cooling loops are kept separate up to the heat transfer system room where they group into the 3 cooling circuits of the blanket. In this room individual cooling loops can be isolated from each other by ice plugs (if valves are not used) and be checked progressively for leaks with tracer elements.

Upper port allocation and diagnostics

All inboard and outboard manifolds end in the proximity of the upper port and are fed through it by circular pipes arranged in two ranks near to the side walls. The pipes are 2.5" and occupy 14 cm space including support clamps and welding access. There are 8 pipes on either side of all upper ports.

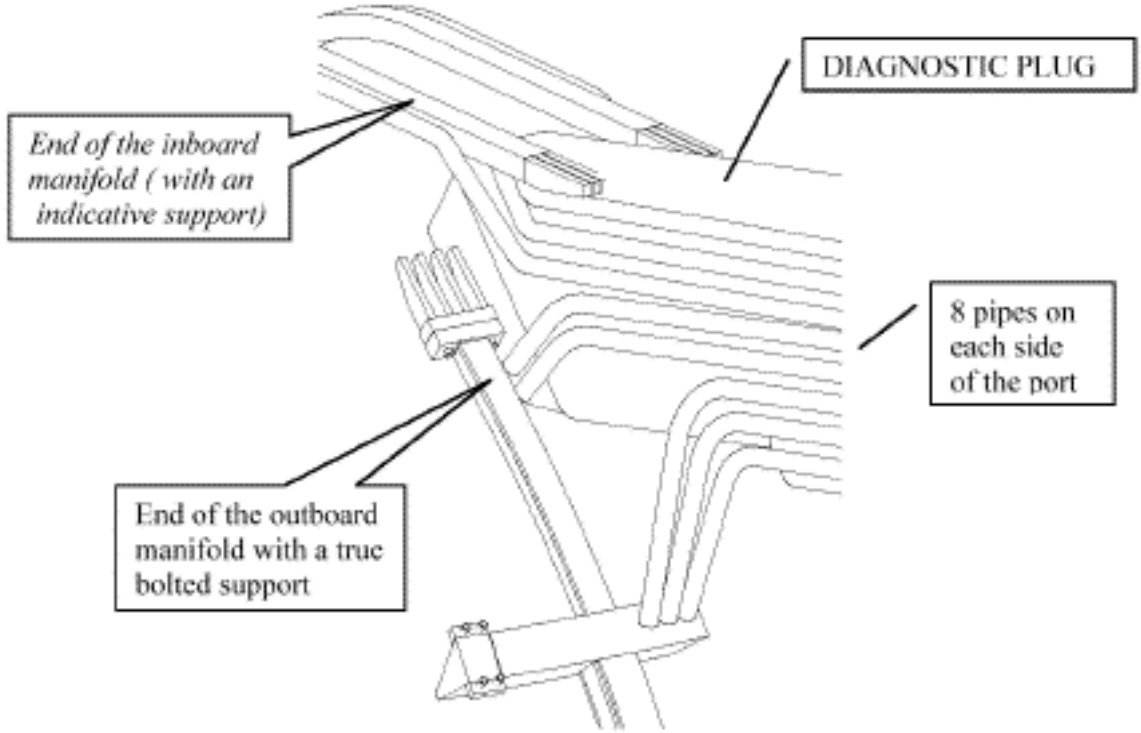

Figure 4.1-3 – Typical arrangement in the 18 upper ports (port duct omitted)

The access through the trapezoidal port is 58 cm wide on the top and 88 cm on the bottom. It is still adequate for EC antennas and diagnostic plugs. The permanent pipes should not cross the flange of the port and thus they are channelled upwards from the port duct before the flange through special twin chimneys built symmetrically either side of the split field joint.

The in-vessel diagnostics have few interferences with the separate cooling manifolds in the inboard blanket because the gap between the modules is free also for the passage of the cables. Outboard of the plasma the passages of the cables and the diagnostic positions need integration with the filler shields, as in the 1998 ITER design, and require ad-hoc cuts in the modules. Local modifications are required, but are feasible.

Manifold cross section design

The cross section of the manifolds is typically sized for 3 blanket modules, each needing a coolant flowrate of 8 kg/s in average. The coolant velocity derives from the pressure drop allowed in the manifolds, 1 bar over the 5 assumed in total, and the range is 6-9 m/s.

The manifolds have a rectangular cross-section to match better the modules and avoid gaps in the nuclear shielding. The restraint on the vessel is also easier than for circular cross-section pipes.

The manifolds are a welded assembly of 10 mm thick L, T, I profiles, plates and massive end flanges. The outboard manifolds include also forged and drilled blocks as horizontal filler shields above and below the ports. The material is the same stainless steel as the vacuum vessel: 316 L(N)-IG.

High reliability against leaks is provided by multipass welds, typically 3 passes in the 10 mm thickness, and their location where the bending moment of the coolant pressure is zero. In this way the welds have the same stress as in circular pipes. All corners, where stress intensification exists, are rounded because they are made from machined or rolled profiles, or because they are welded on both sides. The manifolds, being built at the factory, can be thoroughly checked for leaks and reliability.

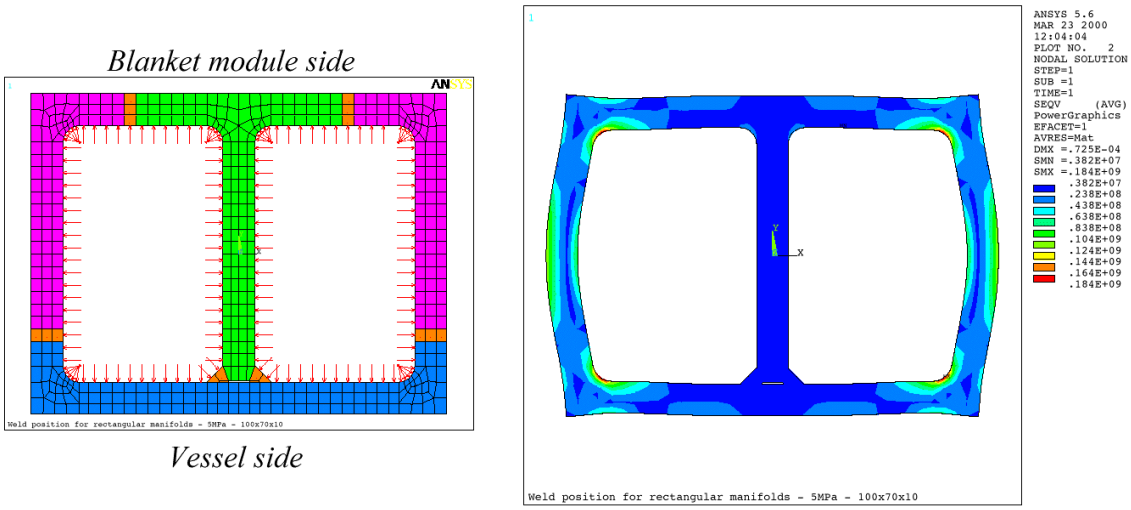

Figure 4.1-4 – Bending free welds in the manifold with 5MPa coolant pressure.

To allow in situ repair of any leak, all welds between the profiles are located in visible regions and can be reached after removal of the blanket modules.

Manifold restraint concept

The longitudinal thermal expansion of the manifolds in the poloidal plane is restrained by the vacuum vessel to avoid any sliding supports relying on low friction under vacuum. Instead the transverse thermal expansion, in the toroidal and radial planes, is not constrained.

The relatively thin manifolds induce negligible thermal stress in the vessel wall while they undergo a large thermal stress in the poloidal direction. Under present assumptions the inlet temperature of the blanket coolant is the same as the inlet temperature of the vessel coolant. Nominally the inlet manifold of the blanket is at the same temperature of the vessel and the outlet blanket manifold is 50°C warmer during pulses. The associated compressive stress of 157 MPa is within the 195 MPa thermal stress (1.5 S_m) allowed above the total primary stress (1.5 S_m) without reduction of the load capability. Therefore there is margin for temperature excursions ±20°C during the transients and inaccuracies of the temperature control system of the coolant. The undercooling of the inlet manifolds is possible within the above excursions, because the curved parts try to detach from the vessel wall. At present only 10°C undercooling of the inlet manifolds with respect to the vessel is envisaged in operation (5°C average vessel temperature higher than the coolant, 2°C vessel oscillation and 3°C blanket oscillation). Actually the coolant temperature fluctuates more but the heat capacity of

the system is large. Undercooling of the inlet manifolds is possible in operation within the above excursions. A number of more extreme accidental excursions are acceptable within the fatigue limit of the materials, i.e. the welded joints.

Support design

The typical longitudinal support is formed by a bracket on the vessel and a flange with two bolts at the end of the manifold. The bracket is welded to the vessel by a set of webs which distribute the reaction force (typically 750 kN) on a wide surface, decreasing the shear stress applied to the wall at 25 MPa. The manifolds are connected to the bracket by high strength M36 bolts, which can react also in tension the typical compressive load of the flange These bolts are made of Inconel 718 and are similar to those of the module supports.

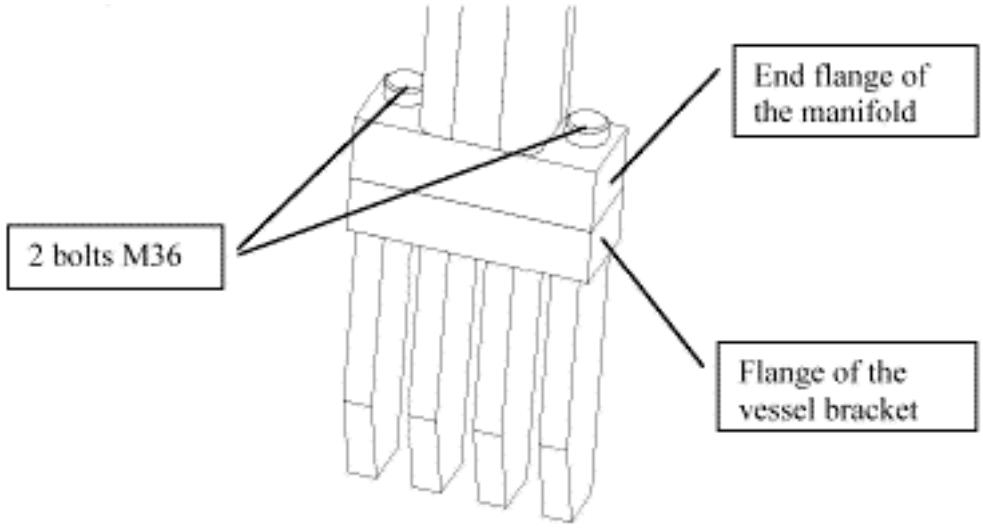

Figure 4.1-5 – The bolted lower end supports of the outboard manifolds.

Mechanical connection has been preferred to a strong weld because it reduces the possible vessel distortions during the initial assembly, it improves the disassembly of the manifolds for repair, and helps the separate manufacturing of the manifolds. However, the bolted flange is larger than a welded one and needs more material to be cut away in the back of the modules locally.

A welded connection has been preferred for the radial/toroidal supports which are small and distributed every 50 cm along the manifolds. These supports are formed by a thin socket applied to the vessel and a retention collar, made from 4 mm bent sheets welded with a fillet to the vessel wall. The manifolds sit inside the socket and cannot move toroidally.

Thermal stress analysis

The inboard manifolds are plane and their compressive force 750 kN is balanced by the two end supports. In the top inboard curved region they generate a pushing force of 450 kN/m poloidal towards the vessel. The straight part relies on the toroidal restraints to prevent buckling.

The outboard manifolds have an arc profile in the vertical plane and include two 15 cm offsets corresponding with the equatorial port, whose width is larger than the 10° toroidal span of the modules in the outboard blanket. The restraints at both ends of the toroidal filler shields provide the reaction torque which balances the offset between the compressed

manifold segments. The outboard manifold cross-section decreases from the top to the bottom because the row of modules are different and do not need to have the same cut outs as in the inboard blanket. To take account of the variation of the number of channels and thus of the compressive force, an intermediate support is located above the equatorial port. The efficiency of the support system and the stress condition of the manifolds has been verified with a 3D finite element model. The pushing force of the arc manifold towards the vessel is typically 250 kN/poloidal m radially.

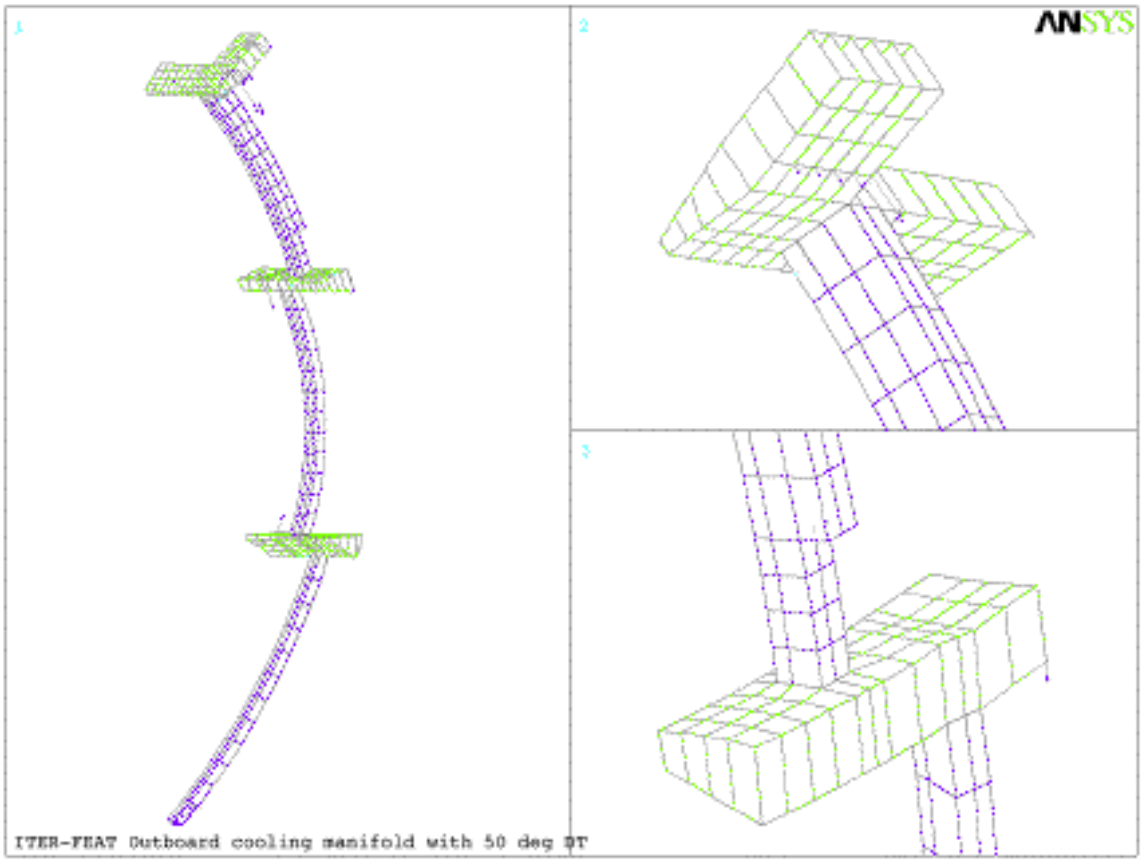

Figure 4.1-6 – Control of the reaction force distribution with a 3D finite element model (the upper manifold extension is missing).

Impact on the blanket module

In the inboard blanket modules narrow prismatic keys are located in between the flexible supports, to leave some vertical corridors free for the manifolds. A third smaller key is located in the middle of the module for centring. For alignment with the upper port the manifolds require the installation of the modules over the field joint in 9 cases out of 18. Therefore some centre key and some sockets of the electrical strap are located on the splice plate. The hydraulic connection is pre-assembled on the vessel and the two ends of the branches are welded to the manifolds. The modules on the inboard cylindrical vacuum vessel are similar because the manifold maintains the same size even if some channels end. The space they vacate is occupied by the remaining channels getting larger.

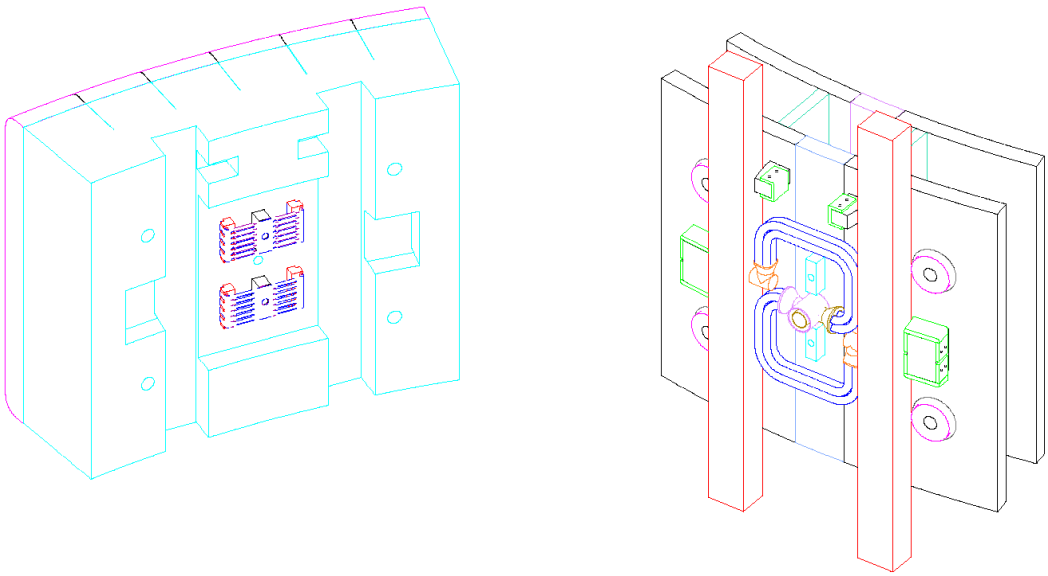

Figure 4.1-7 – Typical attachment of the inboard blanket modules.

In the outboard blanket, stub keys are used, because the space is large enough and they minimise the interface with the vessel. Modules mounted over the field joint need only electrical strap sockets on the splice plate. The branch pipes are mounted between the manifolds which need a tubular extension from the side to the centre of the modules.

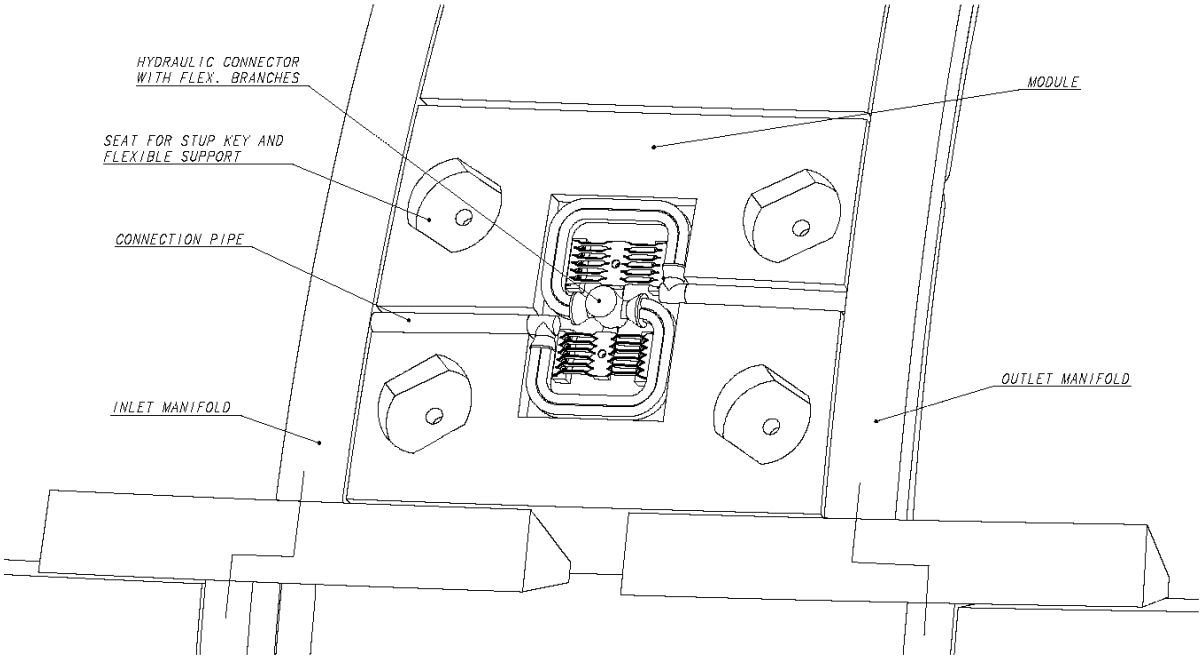

Figure 4.1-8 – Typical attachment of the outboard blanket modules.

Since in a row of modules the inlet/outlet manifolds occupy alternate positions, the coaxial nozzle of the hydraulic connection is inverted 180° to deliver/return the coolant to the module always in the same direction.

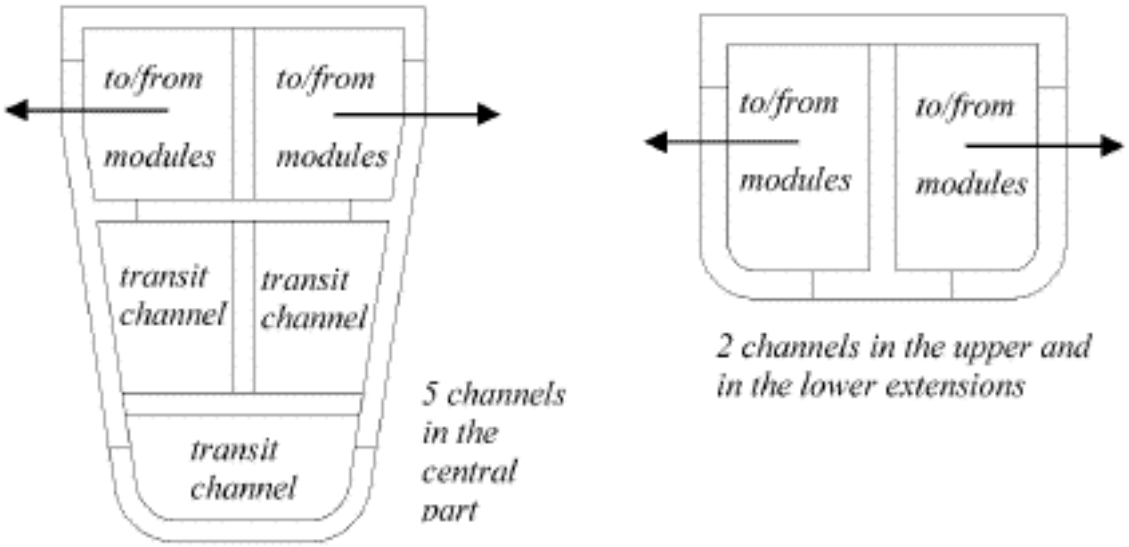

Fig. 4.1-9 – The variable cross section of the outboard manifolds.

Leak detection and repair

In the case of a leak in the blanket, the cooling loop including 2-4 modules is identified by tracer elements injected in the coolant. After that the loop is drained and dried and prepared for He leak testing, which may be necessary to check the hydraulic connections and to identify the faulty module, when the damage is not evident. The vacuum vessel is opened and the RH vehicle is prepared near to the leaking group of modules.

A previous study has shown that most of the water coolant in a loop is entrained upward through the manifolds by a strong gas stream. If this result were not confirmed, a drainage system should be installed.

In that case a siphon pipe reaches the lowest point inside the outlet manifold channel. These pipe are small, typically 16 mm in diameter and 1 mm thick, and hosted inside the manifold to avoid new vacuum boundaries. They will emerge from the manifolds inside the upper port. From here onward the pipes are routed separately and leave the pipe bore free for any crawler tool. There are 8 drain lines per port.

Electromagnetic loads

Significant electromagnetic loads arise in the manifolds from the poloidal currents induced by changes of the toroidal flux during the thermal quench of the plasma or the fast discharge of the TF coils. The former produces the pulling force which is reacted by the welded sheet clamps, the later pushes the manifolds against the support sockets on the vessel. The small radial field generates minor toroidal forces reacted by the indentation of the sockets.

In the inboard region a thermal quench produces a pulling force of 120 kN/m poloidal and a toroidal force 7.5 kN/m poloidal. The TF coil fast discharge produces a pushing force of 40 kN/m poloidal.

The horizontal filler shields integrated with the cooling manifolds have end supports which are electrically insulated and exclude radial currents to/from the vessel. All bolts use washers coated with ceramic insulation to prevent thread seizure by current flow.

Conclusions
Recent design evolutions show that the separate blanket cooling manifolds can be thick, robust and reliable. They can be repaired inside the vessel and are compatible with the diagnostic plugs and the EC antenna in the upper ports.

Since the separate manifolds avoid any vessel coolant contamination and improve the leak testing of the blanket they are adopted as the reference design for ITER FEAT.

4.2. Vacuum Vessel Design Development

4.2.1. Fabrication

The Vacuum Vessel (VV) is a torus-shaped, double-wall structure with shielding and cooling water between the shells. The double-wall structure is made from SS 316L(N)-IG, with stiffening ribs between the shells to give the required mechanical strength. The inner and outer shells are both 60 mm plates and the stiffening ribs 40 mm plate. The space between the shells will be filled with plates made of SS 304 containing 2% boron (SS 30467), and the ferromagnetic SS 430.

To minimize the final assembly time on site, and to deliver the vessel structure with a higher quality, the VV is to be fabricated in the factory as 9 sectors each spanning 40° and to be transported to the site. The practicality of transporting a large sector from the factory to the site is an important factor in the manufacture of the vessel and must be assessed after the site is selected. Each sector includes a full set of ports at the toroidal centre of the sector and a set of half ports (split on the port centre) on each side. The port stubs on the lateral sides of the sector are not installed in the factory. This allows the TF coils to be installed in the assembly area.

Due to the addition of blanket supports in the VV double wall structure, stiffening ribs between the shells are partially replaced by flexible support housings for the blanket module support. Currently, the VV design details are under development, taking account of the optimization of the layout of the ribs and support housings, the structural integrity of the VV, and the detailed fabrication procedure. One of the current design efforts is to reduce the number of the ribs to minimize the associated fabrication cost.

The shielding blocks are installed at the factory before shipment to the site for all circuits except in the area of the field joints. In addition, most of the instrumentation is to be installed at the factory.

Two concepts have been considered for the sector fabrication scheme. One is to complete the inner shell first because it forms the first confinement boundary. Butt weld joints can be fully applied to the inner shell and inspection can be easily performed. Next, all ribs and support housings would be welded to the inner shell. After shield blocks have been installed, parts of the outer shell would be welded (access is from the rib side and through the open space). The remaining parts of the outer shell would be welded (with a one-sided weld). Another concept is to utilize poloidal segments of a double wall structure, which are fabricated first then welded together to form a sector. This scheme was employed for the full-scale vessel sector fabrication in the L-3 R&D project.

The development of full base metal stress capability requires assurance of complete penetration at the weld root opening. To achieve complete penetration at the root, considering the specific configuration and assembly requirements for the VV, similar but slightly different weld details will be used for various areas of the shells, shell closure sections, and ports. Where access to the root side of the joint is not possible, a joint design is required that assures the root side is smooth and uniform which will allow it to be reliably inspected. This is required to achieve the full design allowances as specified by the welding codes.

Actual manufacturing welding process selection is influenced by various factors including material type, thickness, component design and intended service-specific requirements. A vessel of the size and complexity of the ITER vessel can be expected to utilize a combination of weld processes depending upon the type of weld joint, accessibility, and volumetric examination required. Both automated and manual welding are expected to be used during the actual vessel manufacturing.

All conventional manual, automatic, and most advanced welding processes are suitable for use on SS 316 L(N)-IG. ITER specifications identify inert gas tungsten arc welding (TIG) as the preferred process to be used for the vessel and port welds but other processes such as metal inert gas (MIG) welding, metal active gas (MAG) welding, and electron beam (EB) welding are also acceptable and will be considered as ways to increase welding productivity and decrease distortion. Welding procedures are to be qualified in accordance with an accepted code. Specified material properties at the weld joints, such as ferrite content in the deposited metals, must be assured.

Most weld joints are to have conventional configurations and to be radiographically inspected to assure 100% weld efficiency. It is considered that they could be easily code/standard qualified. However, the one-sided weld joints between the outer shell and the ribs and the field joints cannot be radiographically inspected and will be inspected by UT (ultrasonic testing). In this case, a special code case will be required. The current approach of the weld joint designs is to minimize the code cases.

To reduce the VV fabrication cost, a forged and/or cast structure has been investigated[81]. The region of the VV gravity support is a highly-stressed region, requiring numerous reinforcements. Instead of an all-welded shell structure, a forged structure would reduce the fabrication cost and improve the fabrication tolerances there. In addition, a large number of the housings in the VV for the blanket module support that have a relatively small and simple structure can be manufactured by precision casting for cost saving. A preliminary comparison of the fabrication costs between the forged/precision cast structures and the welded structures shows a cost benefit for the forged/precision cast structure. Powder HIPing is also being considered for further cost reduction.

The most important VV R&D performed so far during the EDA was associated with the fabrication of a sector. The Full Scale Sector Model, fabricated and tested as a part of the L-3 project, provided critical information related to fabrication technology required to produce a high quality sector, and the magnitude of welding distortions and achievable tolerances. Since the basic design of the ITER-FEAT VV is the same as the fabricated sector

[81] "Improvement of VV fabrication method for RC-ITER" - JAHT report, INT-9022 - June 11, 1999 and "EU contribution to the task force report, Section VI.5 Improvement of manufacturing processes for cost reduction," EUHT report, June 14, 1999.

model (i.e., the material, the basic torus shape, and the double wall structure with shielding and cooling water between the shells), this R&D also validated the fundamental feasibility of the ITER-FEAT double wall design. Additional R&D, such as the fabrication of a partial VV sector model, may be required to confirm the improved fabrication technology and associated tolerances, as a first step to be done by the industrial firm chosen for manufacturing the vacuum vessel.

4.2.2. Vacuum Vessel Loads/Function vs 1998 ITER

The primary functions of the ITER-FEAT Vacuum Vessel (VV) are the same as for the 1998 ITER design. These functions are to provide a high quality vacuum for the plasma, as well as the first confinement barrier of radioactive materials and a second barrier (after the cryostat) for the separation of air. The total decay heat can be removed by the water in the VV cooling system, even when all the in-vessel cooling loops are not functioning. The vessel still supports the blanket and divertor components, however the blanket modules are attached directly to the VV since the back plate has been eliminated. In addition, a tight fitting configuration of the VV aids the plasma vertical stability, and the ferromagnetic material in the VV reduces the toroidal field ripple. Along with other in-vessel components, the VV provides radiation shielding in particular for the magnets, and even more so to reduce the post shutdown radiation level in the cryostat.

The water flow velocity and flow rate for normal operation needs to cope with the nuclear heating rate in the VV, and keep thermal stresses in the VV structure at acceptable levels. Table 4.2-1 summarizes the VV cooling and baking conditions for the VV. The required water flow condition for normal operation is forced turbulent flow. In order to maintain stresses at acceptable levels for the separate manifold under the current design, it is necessary for the VV cooling water inlet temperature to be similar to the blanket water inlet temperature which is 100°C. Capability of natural convection cooling is provided to remove the decay heat of both the VV and blanket during off-normal events, e.g., the event of a multiple cooling pump trip.

Table 4.2-1 Cooling/Baking Conditions of the Vacuum Vessel

Parameters	Unit	Value
Maximum Total Heat Removal	MW	~10
Water Parameters		
- Normal Operation		
- Inlet / Outlet Temperatures	°C	~100 / ~ 104
- Inlet Pressure	MPa	~ 1.1
- Flow Velocity	m/s	0.04
- Total Flow Rate for Parallel Cooling System	kg/s	~ 950
- Baking Operation		
- Inlet Temperature	°C	200
- Inlet Pressure	MPa	~ 2.4

As was the case for the 1998 ITER, the ITER-FEAT VV must withstand many individual and combined loading conditions during both normal and off-normal operation (see box[82]). For normal operating conditions (category I and II events), the most severe loads are caused by the coolant pressure, VV and in-vessel component weights, seismic events, plasma

[82] Annex to ITER Design Requirements & Guidelines Level 1 (DRG1) G A0 GDRD 2 W0.2

disruptions and VDEs, and the TF coil fast discharge (TFCFD). The loads that will most likely drive the design are due to the centred disruption, VDE, and TFCFD. A summary of VV loads is shown in Table 4.2-2.

Load combinations

A set of rules are being used across the ITER design to establish event combinations and to classify them. A fundamental question is to establish the probability of one condition triggering another loading event. In fact, after an initiating condition, other additional conditions may occur.

- *Conditions are here called "likely" to occur if their conditional probability is higher than 1%.*

- *Conditions are here called "unlikely" to occur if their conditional probability is smaller than 1%.*

Whenever lacking a more comprehensive probabilistic analysis, conditions are categorized as follows:

- *Category I, for a combination of:*
  - *All category I conditions when occurring at the same time or likely to be triggered by the initiating condition.*

- *Category II, for a combination of:*
  - *The above category I combinations with other category I conditions also when they are unlikely to be triggered by the initiating condition.*
  - *A category II condition with other category I and II conditions which are present or likely to be triggered by the initiating condition.*

- *Category III, for a combination of:*
  - *The above category II combinations with other category II and I conditions also when they are unlikely to be triggered by the initiating condition.*
  - *A category III condition with other category I, II, and III conditions which are present or likely to be triggered by the initiating condition.*

- *Category IV, for a combination of:*
  - *The above category III combinations with other category III, II and I conditions also when they are unlikely to be triggered by the initiating condition.*
  - *A category IV condition with other category I, II, III, and IV conditions which are present or likely to be triggered by the initiating condition.*

Following the above general considerations, the following table shows the typical combinations for the definition of seismic events SL-1 and SL-2. The subsequent box gives the definition of Disr. I & II plasma disruptions and VDE I, II & III vertical displacement events.

Load Combinations and Their Categories

Pressr	*Seism*	*Plasma*	*Magnet*	*Others CatI*	*Others CatII*	*Others CatIII*	*Others CatIV*	*Cat*	*# of cycles*
		VDE I		*L*				*I*	*150*
		Disr. I		*L*				*I*	*3000*
		Disr. I	***F.Disc***	*L*				*I*	*50*
		L	*L*	***I***				*I*	*-*
LOCAII		*Disr. I*						*II*	*50*
		VDE I		*U*				*II*	*-*
		Disr. I		*U*				*II*	*-*
		Disr. I	***F.Disc***	*U*				*II*	*-*
		U	*U*	***I***				*II*	*-*
LOCAII		***Disr. II***		*L*	*L*			*II*	*300*
LOCAII		***VDE II***		*L*	*L*			*II*	*15*
	SL-1	*Disr. I*		*L*	*L*			*II*	*-*
	SL-1	*VDE I*		*L*	*L*			*II*	*-*
		L	*L*	*L*	***I***			*II*	*-*
LOCAIII		***Disr. II***		*U*	*U*			*III*	*-*
LOCAIII		***VDE II***		*U*	*U*			*III*	*-*
		Disr. II	***F.Disc***	*U*	*U*			*III*	*-*
		U	*U*	*U*	***I***			*III*	*-*
	SL-1	*Disr. II*	*F.Disc*	*U*	*U*			*III*	*-*
	SL-1	*VDE II*	*F.Disc*	*U*	*U*			*III*	*-*
LOCAIII		***VDE III***		*L*	*L*	*L*		*III*	*-*
		L	*L*	*L*	*L*	***I***		*III*	*-*
LOCA IV		*Disr. I*						*IV*	*-*
LOCAIV		***VDE III***		*U*	*U*	*U*		*IV*	*-*
		U	*U*	*U*	*U*	***I***		*IV*	*-*
	SL-2	*VDE I*		*L*	*L*	*L*	*L*	*IV*	*-*
	SL-2	*Disr. I*		*L*	*L*	*L*	*L*	*IV*	*-*
		L	*L*	*L*	*L*	*L*	***I***	*IV*	*-*

Disruption Definitions

Type I - a normal worst case fast disruption. *Its characteristics are:*

Initial Plasma State	*EOB*
Condition category	*I: Normal*
Initial Plasma current	*15 MA*
Total duration to zero plasma current	*54 ms*
Peak Plasma current	*~16 MA*
Expected number of events	*3000*

Type II - an upset worst case fast disruption. *Its characteristics are:*

Initial Plasma State	*EOB*
Condition category	*II: Likely*
Initial Plasma current	*15 MA*
Total duration to zero plasma current	*27 ms*
Peak Plasma current	*~16 MA*
Expected number of events	*300*

VDE Type II. *In this worst case scenario:*

1. *the plasma remains in a healthy (full beta and plasma current) configuration until it becomes a limiter plasma when a fast thermal quench takes place (loss of beta).*
2. *the plasma continues to drift vertically without current quench until q_{edge} reaches the critical value of 1.5. At that time a slow plasma disruption is initiated.*
3. *slow disruptions are thought to give rise to higher vertical loads on the passive structure since they allow additional plasma vertical drift into the destabilizing quadrupolar field.*
4. *halo currents will develop and will contribute to the global vertical equilibrium. They will start developing as soon as the plasma becomes limiter-like.*

The above VDE scenario followed by a slow current quench (VDE/S) can be summarized by:

Definition of type III VDE followed by slow current quench

	VDE/S type III
Initial Plasma State	*EOB*
Condition category	*III: Unlikely*
Current Quench initiator	*q=1.5*
Plasma Current quench duration	*~100 ms*
Direction of movement	*Up / down*
Expected number of events	*-*
*Peak (Ihalo*Pf/Iplasma) (1)*	*0.58*
Peak total net horizontal load [MN]	*25*
(1) Pf = Toroidal peaking factor of the halo currents	

Disruption Definitions (continued)

Type II VDE

For these slow VDEs (VDE/S), the assumption is that they will occur 15 times in the lifetime of the machine and that they will generate a load equal to 75% of the Type III VDE/S. Their Category is II.

Type I VDE

For these slow VDEs (VDE/S), the assumption is that they will occur 150 times in the lifetime of the machine and that they will generate a load equal to 60% of the Type III VDE/S. Their Category is I.

VDE's followed by fast current quench (VDE/F)

Type I ,II, and III VDE's are particularly severe for the intensity of the net vertical loads and their impact on the Vacuum Vessel.

An equal number of VDE's of all types (I,II,and III), followed by a fast current quench are considered in the design with the assumption of a toroidal peaking factor as well as a net horizontal load equal to half of what is assumed for the VDE/F.

Definition of type III VDE followed by fast current quench

	VDE/F type III
Initial Plasma State	*EOB*
Condition category	*III: Unlikely*
Current Quench initiator	*q=1.5*
Plasma Current quench duration	*as Disrupt type II*
Direction of movement	*Up / down*
Expected number of events	*-*
*Peak (Ihalo*Pf/Iplasma) (1)*	*0.58/2=0.29*
Peak total net horizontal load [MN]	*25/2=12.5*
(1) Pf = Toroidal peaking factor of the halo currents	

The major changes in the loads for the ITER-FEAT VV with respect to the 1998 ITER VV result from design modifications in the following areas.

1. Changes related to the smaller machine size, the lower plasma current and the new magnetic configuration. These changes tend to reduce VV loads.
2. The elimination of the back plate which results in; (a) increased induced and halo currents, (b) direct loads from the blanket modules to the VV, and (c) increased nuclear heating to the VV. These changes tend to increase VV loads.

Table 4.2-2 VV Load Summary

	ITER Load Category	1998 ITER	ITER-FEAT*
Water pressure (Normal operation/Baking operation) (MPa)	I	0.4/1.8	1.1/2.4
Gravity load (MN)	I	190	100
Plasma current quench			
- EM pressure on inboard/outboard VV wall due to induced currents (MPa)	II	1.2/0.6	1.2/0.6
Centered disruption			
- Maximum radial moment on a module at the inboard wall (MNm)	II	-1.25	-0.65
- Maximum poloidal moment on a module at the inboard wall (MNm)	II	0.77	0.61
VDE followed by a fast current quench (Fast VDE)			
- Maximum radial moment on a module at the inboard wall (MNm)	III	-1.74	-0.88
- Maximum poloidal moment on a module at the inboard wall (MNm)	III	1.0	0.76
VDE followed by a slow current quench (Slow VDE)			
- Maximum EM pressure on the VV wall due to halo current (MPa)	III	2.8	3.9
- Poloidal force on a module (MN)	III	1.0	1.0
- Radial force on a module (MN)	III	1.3	0.4
- Maximum total net vertical force on VV and blanket for downward/ upward slow VDE (MN)	III	-150/ 80	-71/52
- Maximum total net horizontal force on the VV and blanket (plasma tilting and shifting) (MN)	III	50	25
TF coil fast discharge			
- EM pressure on the VV inboard wall due to the poloidal induced current (MPa) [Current quench time (sec)]	I	2.1 [15]	1.6 [11]

*: According to the most recent assessment[83]. for 15 MA plasma operation. Load values on blanket modules may vary depending on the blanket module design.

A preliminary assessment of the electromagnetic loads on the VV and on the blanket module has been made for the case of 17.4 MA plasma operation. Assuming that the toroidal field remains constant in comparison with the 15 MA operation case, the electromagnetic loads on the blanket modules due to the induced currents coupled with the toroidal field, the loads on the VV and the blanket modules due to halo currents coupled with the toroidal field increase linearly with the plasma current (by a factor of 1.16). The electromagnetic pressure on the inboard and outboard wall, mainly caused by the interaction of the induced toroidal current due to the plasma quench and the poloidal field, increases proportionally to the square of the ratio of the plasma currents (a factor of 1.33). The electromagnetic pressure due to the TF coil fast discharge remains the same.

[83] G 73 MD 34 00-04-19 W 0.1, "FEAT category III fast/slow downward/upward VDE simulation" and G 16 MD 280 00-05-22 W 0.1, "EM loads on modules for the ITER-FEAT."

4.2.3. Structural Assessment of the Vacuum Vessel

The most severe loading conditions for the VV are the toroidal field coil fast discharge (TFCFD) and the load combination with electromagnetic loads due to a plasma vertical instability. In this load combination a high compressive stress occurs in the VV inboard wall and the VV structure has to withstand buckling instability. A non-linear analysis has to be performed assuming the worst possible geometrical imperfection.

The direct attachment of the blanket modules to the VV shell produces local stress and geometrical discontinuities of the VV shells. Detailed analyses have been performed to assess the stress level in locations of geometrical discontinuities and where concentrated loads are applied.

The location of the VV supports has an impact in the stress distribution and local stress and influences the VV deformation and dynamic behaviour. A comparison of the results obtained with different support locations has been performed.

Toroidal field coil fast discharge

In the case of a TFCFD, the induced poloidal currents in the VV interact with the toroidal magnetic field causing compressive stress in the VV inboard wall. Elastic buckling analysis[84] has shown that the critical elastic buckling pressure is much larger than the pressure causing a stress level above the yield.

The inelastic buckling analysis requires the definition of the initial imperfection of the VV geometry. Different shapes of the VV geometrical imperfections have been considered[85]. The type of geometrical imperfection that has the minimum critical inelastic pressure is the radial misalignment of adjacent sectors. An assessment performed assuming a VV geometry similar to the present ITER FEAT VV design has given a critical buckling pressure of 6.6 MPa (misalignment of adjacent sectors = ±5 mm).

Following, for example, the recommendations from a code, e.g. RCC-MR, and assuming a load factor (ratio between the inelastic buckling and the operating load) of 2.5, the maximum allowable electromagnetic pressure value on the inboard wall is 2.64 MPa (the estimated pressure for ITER FEAT in case of TFCFD is 1.6 MPa). An analysis on the reduction of the total double wall thickness at the inboard wall of 100 mm (from 388 mm to 288 mm) has given a relatively small reduction of the critical pressure (~5%) (ITER FEAT VV inboard wall is 338 mm). Also the increase of the initial imperfection of the VV geometry from ±5 mm to ±10 mm causes a reduction of the critical pressure of ~4%.

Load combination : TFCFD and Plasma VDE

To reduce the primary stress in the VV, the inboard wall can be reinforced by making the triangular support frame that holds the lower modules of the blanket at the inboard wall toroidally continuous. This solution gives also advantages for the plasma stability. Three

[84] G Sannazzaro - G 15 MD 144 99-04-27 W0.1 - Elastic buckling of the RTO-RC ITER VV inboard wall due to TFC fast current discharge - 15 June, 1999.
[85] G Sannazzaro - G 15 MD 149 99-06-15 W0.1 - Inelastic buckling of the RTO/RC ITER VV inboard wall due to TFC fast current discharge - 15 June, 1999.

design options of the support frame shape and size have been considered[86]: 1) large frame (1.6m high), 2) small frame (0.9m high) and 3) no frame.

Table 4.2-3 summarizes the results obtained for the following load conditions:

Loads conditions : 1) TFCFD : 1.6 MPa at the inboard wall
2) TFCFD (1.6 MPa) + Downward VDE I (2.3 MPa)
3) TFCFD (1.6 MPa) + Downward VDE II (2.8 MPa)

Table 4.2-3 Summary of Primary Membrane Stress Results for TFCFD and VDE Events

Static analysis results : Primary membrane stress intensity (MPa) and stress safety margin in brackets (1) in the VV inboard wall for the 3 design options					
Load case	Load category	Allowable (MPa)	Large frame (1.6m)	Small frame (0.9m)	No frame model
TFCFD	I	137	62 (2.2)	62 (2.2)	62 (2.2)
TFCFD + VDE I	II	137	100 (1.37)	121 (1.13)	131 (1.05)
TFCFD + VDE II	III	164	114 (1.44)	137 (1.20)	147 (1.12)

(1) The stress safety margin is the ratio between the allowable stress and the calculated stress.

The non-linear buckling analyses[87] have given the following results for the 3 types of reinforcements.

Table 4.2-4 Summary of Non-linear Buckling Analyses

Buckling safety margin for the 3 design options – Geometrical imperfection type : sector misalignment +/-5 mm				
Load case	Allowable safety margin (RCC-MR)	Large frame model	Small frame model	No frame model
TFCFD	2.5			4.1
TFCFD + VDE I	2.5	2.9	2.5	2.4
TFCFD + VDE II	2.0	2.5	2.2	2.1

The present design of the ITER FEAT VV has adopted the “small frame option”. For this option the buckling load does not exceed the allowable value, but is very close to it.

Stress in the VV due to the direct attachment of the blanket modules to the VV

The VV has to provide support to the blanket modules. At the attachment points the VV needs to be reinforced to avoid large local stresses. The main loads from the blanket modules to the VV are caused by fast plasma disruption. The induced currents in the blanket modules

[86] TAC Meeting – Presentation by K Ioki – Naka, December, 1999.
[87] TAC Meeting – Presentation by K Ioki – Naka, December, 1999.

generate poloidal and radial moments. Each module is radially supported by 4 flexible cartridges that transfer the poloidal moments to the VV shells. The flexible cartridges are recessed inside the VV wall, rather than in the blanket module. This solution has the advantage that the nuclear heat generation on the flexible cartridges is strongly reduced, and the design of the blanket module is simpler. On the other hand, the continuity of the inner VV shell is lost and stress concentration is generated at the holes required to locate the flexible supports.

Several designs have been studied to limit the induced currents and the poloidal moment on the blanket modules and to minimize the stress in the VV. Present evaluations (studies are still in progress) show that the poloidal moment can be reduced to a maximum value of ~ 0.6 MNm and the consequent membrane + bending stress in the VV shell can be limited to 90 MPa.

Two different design options to support the radial moment (the moment along the axis normal to the module first wall) applied to the module in case of plasma disruption and VDE have been considered: stub keys and shear keys. (Stub keys are extensions of the cylindrical housings for the flexible attachments that engage into the back of the blanket modules, whereas the shear keys are solid blocks welded to the vessel shell).. In an analysis performed on the modules attached to the inner VV wall[88] (EM loads on these modules are larger than those on the outboard wall) large stresses have been found in case the radial moment is reacted by the stub keys; therefore the "shear key" design option, with an appropriate reinforcement, has been selected for the modules at the inboard wall.

Operation at 17.4 MA plasma current

The increase of the electromagnetic loads from 15 MA to 17.4 MA operation reduces the stress safety factor for primary loads to values very close to 1. Table 4.2-5 summarizes the comparison between the results for the two operation scenarios at 15 and 17.4 MA. Preliminary buckling analysis has shown that for the present VV design the buckling safety factor is 2.3 for the load case combination TFCFD + VDE I in case of 17.4 MA operation, which is slightly smaller than the allowable value (following the RCC-MR code the allowable value is 2.5). Therefore, a more accurate analysis is still to be performed, reviewing the assumed conditions, which may be conservative. If its results do not improve the buckling safety factor, the requirement to allow operation at 17 MA will lead to make the current VV structure stronger against buckling at the location of the lower inboard wall, to satisfy the code requirement (for example, by adding a locally continuous toroidal reinforcement).

[88] G Sannazzaro - G 15 MD 135 98-11-13 W0.1 - Primary Stress in the VV Inboard Wall due to the Module Direct Attachment (RC-ITER IAM Configuration - Short Flexible)

Table 4.2-5 Comparison of Results from 15 MA and 17.4 MA Plasma Current Operation

Primary membrane (Pm) stress intensity (MPa) and stress safety factor in brackets (1) in the VV inboard wall + buckling safety factor for the 2 operational scenarios: 15 and 17.4 MA						
	Pm (MPa)			Buckling safety factor (2)		
Load case	Ip=15 MA	Ip=17.4 MA	Limit	Ip=15 MA	Ip=17.4 MA	Limit (3)
TFCFD	62 (2.2)	62 (2.2)	137	4.1	4.1	2.5
TFCFD + VDE I	121 (1.13)	127 (1.08)	137	2.5	2.3	2.5
TFCFD + VDE II	137 (1.20)	149 (1.10)	164	2.2	2.0	2.0

(1) The stress safety factor is the ratio between the allowable stress and the calculated stress.
(2) Ratio inelastic buckling load/operational load
(3) The limits are based on RCC-MR

VV support location

The ITER FEAT VV supports have been modified with respect to the 1998 ITER design. A study has been performed to estimate the effect on the stress in the VV of the location of the VV vertical supports from static vertical loads[89]. Three possible locations have been considered: 1) bottom of the VV (same as 1998 ITER design), 2) between the equatorial ports, and 3) top of the VV.

The analysis of the VV behaviour for vertical static loads for the 3 support options, shows that there is not a great difference in the stress values in the main VV structure. The support option 2 generates a slightly larger stress in the VV main shells at the inboard wall mainly due to a larger stress in the poloidal direction. Some localized stress occurs in the support case options 1 and 3 in the poloidal ribs, but these stress values can be reduced by local reinforcements. Vertical displacements of the inboard wall are much larger for support option 2 (equatorial), but the overall value is relatively small (3.8 mm for 80 MN vertical static load due to downward VDE). On the other end, in this case the displacement of the ports, especially the equatorial port, is smaller than in the other two cases.

A design of the VV support made of flexible plates (similar to the 1998 ITER design backplate supports) located between the equatorial port has been developed. The structural analysis[90] has shown that these supports can withstand the envisaged loads on the VV, including seismic and thermal loads.

In comparison to the ITER 1998 design (where the horizontal supports were located at the equatorial port near the port extension) this solution has the advantage that the horizontal stiffness of the overall VV structure is increased. Therefore the first horizontal natural frequency is expected to increase giving a smaller dynamic factor for horizontal seismic loads.

[89] G Sannazzaro - G 15 MD 162 99-10-04 W0.1 - Stress in the RTO/RV ITER VV for different vertical support locations - 4 October, 1999
[90] F Elio – G 16 MD 248 99-10-13 – Peripheral flexible plate supports for the vacuum vessel and the magnets

Overall assessment

The VV must withstand many individual and combined loading conditions during both normal and off-normal operation. Analyses done to date are those considered for the most severe loading cases which will most likely drive the basic design of the VV structure. Although further analyses are required for numerous loading conditions to confirm the structural integrity of the VV, based on the analyses performed to date, the VV appears structurally capable of withstanding the loads to which it can be expected to be subjected

4.3. Design Implications of Divertor Material Choice

The plasma facing material selection for the divertor has been made largely on the basis of lifetime. However, other considerations that have to be taken into account are the generation and control of dust, which is a safety issue, and the chemical trapping of tritium with carbon, which is both a safety and an operational issue. In order to simplify the complex interrelated issues associated with armour choice for the divertor, the discussion below has been broken down into three sections; armour selection, tritium inventory and control, and dust and management of dust.

From the candidate armours for the divertor (Be, C & W), carbon has been selected for the strike point regions of the scrape-off layer (SOL) on the lower vertical target, and tungsten for the upper vertical target/baffle, gas box liner and dome PFCs. Carbon is the choice around the strike points, since beryllium would have an inadequate life-time and W would melt during high power transients and could form surface irregularities that might later form hot spots in normal steady-heat flux operation. Elsewhere, W has been selected because it has the lowest sputter yield in regions where erosion is dominated by charge-exchange (CX) sputtering. However, with the above material selection, of particular concern is the co-deposition of tritium with carbon, which could severely limit the operational availability of ITER by trapping the entire allowable inventory in co-deposited layers. The prospects of using tungsten in the region of the strike point are improving and the divertor design, which offers the possibility of routine remote exchange of the divertor cassettes, lends itself to a change to an all tungsten armoured divertor prior to, or during, the D-T phase.

Armour Selection

The choice of armour for the divertor is a compromise which takes into account power handling capability, armour lifetime, plasma compatibility, tritium retention, activation etc. In terms of lifetime and sustaining the heat flux, the most demanding component is the lower target, where the goal is to survive the following:

- 3000 full power discharges of 400 sec, with a steady state heat flux ~ 10 $MW.m^{-2}$;
- one in ten discharges to include a slow transients (~ 10 sec), where the normal semi-detached operation of the divertor is interrupted and the full power of the SOL is assumed to strike the target (20 $MW.m^{-2}$);
- one in ten discharges to end in a disruption;
- occasional giant ELMs and a significant number of small ELMs.

During the EDA, the silver-free joining of carbon to copper has advanced to a level where armoured plasma facing components can routinely operate with heat loads of 20 MW/m^2, and following a relatively short development period, W armoured prototypes already promise to be as reliable, at similar heat flux, as their carbon armoured counterparts[91].

With regard to erosion lifetime, this is maximised if the cladding is as thick as allowed by the predicted steady-state power load (e.g. ~ 10 mm Be, ~20 mm W, ~ 20 mm CFC) and can be improved further if the threshold for sputtering is higher than the particle energy. The latter consideration favours high Z plasma facing materials such as W (sputtering threshold for D and T are ~ 210 eV and 140 eV, respectively), in particular for the parts of the divertor where CX sputtering is dominant (no ion sheath acceleration). Hence, W is the armour choice for the dome and upper vertical target. CFC is chosen near the strike-points because it sublimes, rather than melts during disruption thermal quenches or giant ELMs, thereby avoiding surface irregularities that might later form hot spots in normal steady-heat flux operation.

Apart from the issues of high heat flux capability and erosion lifetime, the final armour choice also depends on the plasma compatibility and the effect on tritium inventory of the armours. Plasma compatibility is a strong concern for the high Z plasma facing material, such as tungsten. However, ASDEX Upgrade (W)[92] and C-Mod (Mo)[93] have provided evidence that high-Z walled devices can operate, at least in certain modes, without plasma contamination, and further evidence should be provided as ASDEX Upgrade increases, in stages, the W coverage of the first wall[94].

Tritium Inventory

There are concerns over tritium inventory because carbon is considered as a plasma facing material. During D-T operation the co-deposition of tritium with carbon has the potential to trap the entire allowable tritium inventory for ITER-FEAT in a few hundred pulses. Estimates range from 1 to 5 g tritium/pulse[95], the lower value based on physical sputtering alone, and the higher value including both physical and chemical sputtering. The codeposition rate that may result from Be wall erosion is estimated to be < 0.5 g-T/pulse. Even though the divertor is designed to allow the strike point of the SOL to be swept across the vertical target in order to release the T trapped during normal operation, unless specific measures are taken the T will be trapped in the private region of the separatrix and the pumping ducts. In an attempt to mitigate this, controlling the temperature of the private region PFCs is being studied and may provide a workable solution. The design proposal is to employ a "hot" liner. To achieve high operating temperatures, it is proposed to use the

[91] M. Merola, et al., Manufacturing and Testing of a Prototypical Divertor Vertical Target for ITER, 9th Int. Conf. on Fusion Reactor Materials, October 10-15, 1999, Colorado Springs, to appear in J. Nucl. Materials.
G. Vieider, et al; European Development of Prototypes for ITER High Heat Flux Components, ISFNT-5, Rome, 1999.
A. Makhankov et.al. Development and Optimization of Tungsten Armour Geometry for ITER Divertor. Proceed. of 20 Symposium on Fusion Technology, Marseille, September 1998, p.267-270
R.E.Nygren, et al; "Heat sinks armoured with tungsten rods" ISFNT-5 Rome, Sept. 1999
[92] Krieger, K., Maier, H., Neu, R., and the ASDEX Upgrade Team, J. Nucl. Mater. **266-269** (1999) 207
[93] Greenwald, M., H Mode confinement in Alcator C-MOD, Nuclear Fusion, 37 (1997) 793
[94] Neu, R., et al., Plasma operation with tungsten tiles at the central column of ASDEX Upgrade, presented at the 14th International PSI Conference, Rosenheim, May 2000, to appear in J. Nucl. Mater.
[95] G. Federici, et al., *Assessment of Erosion and Tritium Codeposition in ITER-FEAT*, presented at the 14th International PSI Conference, Rosenheim, May 2000, to appear in J. Nucl. Mater.

radiated power from the divertor channel to heat radiatively cooled, tungsten tiles[96]. These tiles are shaped in such a way as to prevent or minimise line-of-sight from the plasma to the cassette body and to create a labrynth through which the helium ash, hydrogen isotopes, and other impurities are pumped from the divertor channels, while providing sufficient length for the hydrocarbons entrained in the gas stream to undergo many collisions with the hot surface of the liner.

In support of this design, laboratory experiments have been carried out at the Institute for Physical Chemistry (IPC) in Moscow. These are aimed at understanding the chemistry of carbon deposition on the hot liner and on the cold surfaces of the divertor and vessel beyond the liner. Although, somewhat preliminary and the subject of ongoing further verification, the main conclusions from these studies can be summarised as follows[97]: 1) the 'hot' liner (to be operated in a range of 800-1000˚C) converts a large fraction of active radical carbon species impinging onto the surfaces of the private region to stable volatile molecules which are pumped away without residual deposits; 2) the remaining fraction of active radicals, although small has a relatively low sticking coefficient and passes through the liner where it leads to the formation of thin, soft, hydrogenated films on the relatively cold (< 150˚C) structures behind the liner. One way of overcoming the deposition of these films is to ensure that the pumping duct behind the liner is kept hot enough (T>300˚C) in order to minimise the sticking of radicals in regions inside the divertor private region. However, in itself this is not enough and an ancillary 'cold' catcher plate must be added to the design, to minimise the formation of tritium-bearing films on cold surfaces downstream of the divertor and all over the vessel. This catcher plate would concentrate active hydrocarbon species escaping through the liner, from where the T could be reclaimed by occasional heating of the catcher to release the T in the form of stable gas molecules, or alternatively by mechanically removing T-bearing flakes to an ex-vessel reclamation facility (e.g. by using a conveyor).. In addition to codeposition on and behind the liner, there will be tritium in the films forming on the surface of the tiles located in the area of net-deposition in the divertor and in the gaps and crevices of the numerous castellations of the plasma-facing components. The deposits on surfaces exposed to the plasma are expected to be recycled, but the films building up in gaps are of concern and need the same attention as those in the private region.

R&D is in progress that will contribute to the to the liner design. IPC experiments use RF and magnetron sources in conjunction with methane, but there are still large uncertainties in the applicability of the results to the ITER divertor. Tests carried out in IPP-Garching[98] and a test with more relevant plasma chemistry to be carried out in the Berlin Plasma Linear Simulator (PLI), should allow, by the end of 2000, better insights into the functioning of the liner. It is important to determine the sticking coefficients versus temperature of the CH radicals found in the divertor exhaust gas stream. Additionally, possible mixed-material effects need further investigation.

[96] A. Makhankov, et. al; "Design of a Radiative Semi-transparent Liner for the ITER Divertor Cassette", ISFNT-5 Rome 1999

[97] I. Arkhipov, et al., , to be presented at the 14th International Conference on Plasma Surface Interactions, Rosenheim, Germany, May 22-26, 2000, to appear in J. Nucl. Mater.

[98] von Keudell, A., et al., *Surface reactions of hydrocarbon-radicals: suppression of the redeposition in fusion experiments via a divertor liner*, presented at the 14th International PSI Conference, Rosenheim, May 2000, to appear in J. Nucl. Mater.

Although it is unreasonable to expect the co-deposition of carbon with tritium to be stopped altogether. However, reduction by one to two orders of magnitude in the rate will reach the anticipated erosion lifetime of the target, when the tritium trapped in the divertor can be reclaimed by baking in the hot cell.

The only methods proven effective for removing tritium so far involve (1) oxidation of the codeposited layers (e.g., thermo-oxidative erosion > 250˚C, or O plasma discharges) or (2) physical removal. For carbon codeposited films, oxidation rates strongly depend on the microstructure of the layers. Mixing of materials shows that higher temperatures might be required for erosion of the films and release of the retained hydrogenic-species [99]. Therefore, although baking at 240˚C may remove soft films, due to the variability of film properties, a baking capability at temperatures greater than 300˚C. would be required. However, frequent use of oxygen bakes raises collateral issues of damage on other reactor vessel components, as well as recovery time for normal plasma operation.

Dust and Dust Management

Dust will be composed of Be (first wall), W (divertor) and C (divertor strike point) causing a significant safety problem associated with hazards of chemical explosion (Be and C dust) and radiological contamination (W and C dust). The definition of dust is somewhat uncertain, but particle sizes <100 μm can be considered as dust. It is anticipated that the tritium bearing co-deposits will build up on cold surfaces in the divertor and in some areas, these films will become thick enough to detach and produce carbon flakes. These flakes (>100 μm), although not strictly dust, are likely to dominate the total mass of dust in the divertor.

There is a large uncertainty in the prediction of the production rate of dust for ITER-FEAT, which have been derived from tokamak experience and code simulations. However, the dust may well require routine removal and will in any case require monitoring in order to guarantee that the levels do not breach the specified safety limits. Two in-vessel dust limits are specified. The first limit is for the dust held on hot surfaces, which has the potential to generate hydrogen during an accident when steam is in contact with the dust. Potentially the worst case is for beryllium dust, which has an exothermic and hence, self-sustained reaction with steam. The limit in this case for particles << 10 μm, that are highly reactive because of their relatively large surface area, is in the range 10 – 20 kg. The second limit is the overall amount of dust that can be mobilised during an accident and, hence, escape into the environment causing a radiological hazard. This is set at a few hundred kg. Within a machine the scale of ITER-FEAT, with an in-vessel surface well in excess of 1000 m^2, these limits represent values that will be difficult to guarantee.

At first sight the limit of 10 - 20 kg on the hot surfaces appears the hardest to fulfil. It is reasonable to assume that dust cannot exist on the hot surfaces directly exposed to the plasma and so fortunately, the critical reservoirs for ‘hot’ dust are limited to the grooves of the horizontal surface of the dome, and the divertor baffle. These grooves or castellations in the tungsten armour are an essential feature of the design and must remain in order to relieve stresses during cyclic loading with high heat flux, thus maximising the fatigue lifetime of the armour to heat-sink joint. Initial analysis shows that the volume of dust that can be contained in these grooves is of a similar order to the ‘administrative’ limit (10 – 20 kg). Hence, the present design of the plasma-facing surfaces is being optimised to minimise dust

[99] M. Balden, ICFRM-9 – 1999, to appear in J. Nucl. Mater.

accumulation (e.g., by decreasing the number and dimensions of the grooves). If the total quantity of chemically reactive dust on 'hot' PFCs can be maintained below the 'administrative' limit, and the authorities responsible for safety can be convinced of this argument, then there will be no need to have reliable methods to measure accumulation of chemically reactive dust in the grooves. What may help further is that the self-sustainable reactivity of beryllium dust with steam may be inhibited, because steam access is restricted to much of the material confined in the grooves. An R&D activity has been launched to study this possibility.

This leaves the rest of the dust (and flakes), not residing on hot surfaces. The majority of this is expected to collect in and beneath the divertor, and based on the experience gained from existing tokamaks, the majority of this will accumulate beneath the inner vertical target, carried there by a combination of grad B drift and gravity. A cross-section of the divertor shows that there is scope for introducing dust handling systems that can either remove dust on-line or during the interval between pulses. Two separate regions are potentially available for this use within the divertor. Firstly the space between the underside of the divertor cassettes and the vacuum vessel, and secondly, the region between the dome PFC and the cassette body.

An R&D activity has been launched[100] that that has manufactured artificial tokamak dust based on measurements of actual tokamak dust, and this will be used to study the transport of dust during accidents, as well as developing means to extract the dust from the vessel. Within this task the effectiveness of various dust removal methods will be studied, ranging from the global, such as removing dust suspended by gas re-circulation or liquid wash, to the local, such as vibratory conveyors. In addition, it is hoped that, with better knowledge of the behaviour of the dust, the quantity remaining can be lowered to levels that require infrequent interventions.

Conclusions

Bearing in mind all the above, the prudent position remains initially to install carbon as armour on the targets, which is forgiving when exposed to disruptions and is acceptable from a plasma contamination viewpoint, and to maintain the option to switch to a more reactor-relevant all tungsten armoured targets prior to D-T operation, when tritium inventory becomes an issue. The decision to make this change will depend on the progress made in controlling the plasma, in particular, on the frequency and severity of disruptions and, on the other hand, the success achieved in mitigating the effects of T co-deposition.

In addition to replacing the targets, it may be necessary to thoroughly clean the carbon from all in-vessel surfaces, since the residual layers will continue to have the potential to collect T by isotope exchange. Hence, even if carbon is considered only for the H and D phases, methods need to be developed that can adequately remove the carbon deposits. Apart from mechanical methods of removing the carbon deposits, baking in the presence of a partial pressure of oxygen has been shown to be effective in removing the soft hydrogenated carbon layers responsible for retaining most of the tritium. This bake, at a temperature to be better determined, may take many days to be effective, but has the potential to reach all the in-vessel surfaces of the machine and may be worthwhile as a one-off event prior to a switch to all tungsten armour.

[100] Eu report on dust.

In summary, D-T operation with carbon poses many problems and in the end these may prove impractical to overcome, but pending the results of on-going R&D with both carbon and tungsten, carbon remains the armour choice for the strike point region of the vertical targets. Tungsten is the choice for all other plasma facing surfaces of the divertor.

5. Buildings and Plant Services

5.1. Developments in Building/Services Design

TAC has questioned some aspects of the design of the buildings for ITER-FEAT.

- With regard to the tokamak building general layout, there was a general question on the available access for services and vertical distribution, particularly the use of the vertical pipe shafts connecting the upper and lower pipe chases.
- The concept of combining the tokamak and tritium building onto a common basemat, as was indicated to be a possibility in the ODR.
- The concept of the diagnostic hall, as its concept and description in the ODR was limited.

These three concerns are addressed below.

Vertical Access in the Tokamak Building

The ITER-FEAT tokamak building is considerably more compact than it was for 1998 ITER design. The current building measures 69.5 meters from east to west, and 77.8 meters from north to south. The building has been redesigned since the 1998 ITER design, and has more challenges to accommodate all the equipment and services required to make ITER-FEAT functional. A particular challenge was to provide access from the bottom of the vessel to the top, as there would be only one area for the heat transfer system. It was decided early on in the reduced cost study to investigate and, if feasible, adopt the idea of using vertical pipe shafts connecting two donut shaped pipe chases, one at the top and the other at the bottom, of the vacuum vessel. These pipe shafts are located outside the bioshield, so that the radiation fields that the contents are exposed to is minimized. These pipe chases collect and deliver cooling water lines to each port for blanket, divertor, and vacuum vessel cooling, as well as providing for system drainage. The biggest user of these pipe shafts is the heat transfer piping. In addition to the piping, the vertical shafts allow for vertical connections of cryolines, which are required to be in close proximity to the vessel to minimize their costs and layout problems. Further, they can be used for conductors, as in cabling and wiring, where the radiation and insulation properties are compatible. There is some, but limited, access available into these pipe shafts during maintenance, so that components and lines can be inspected, monitored and, if necessary, repaired.

Another function of these vertical pipe shafts is to provide a relatively easy and non-restrictive path for accommodating the pressure rise that results from an ex-vessel LOCA (see section 0). The LOCA overpressure is confined to the upper and lower pipe chases, the TCWS vault, and the NB cell. The vertical pipe shafts connect the upper and lower pipe chases at 18 positions around the machine, making such connections relatively unrestricted and providing relatively uniform pressure distribution in this event. The four vertical pipe shafts (see Figure 5.1-1 (a) and (b)) in the north end of the building on the equatorial level (at ports 3, 4, 5, and 6) have no concrete walls, but open directly to the NB cell. In a similar fashion, the seven vertical pipe shafts (at ports 1,2,3 and 15, 16, 17, and 18) on the east side have no concrete walls, but open directly to the TCWS vault.

In addition to these vertical pipe shafts, the ITER-FEAT tokamak building provides limited vertical communication in the four corners of the building,. At these positions are located the stairways, the personnel lifts, the HVAC duct chase (which is used for other vertical access but is limited by available size).

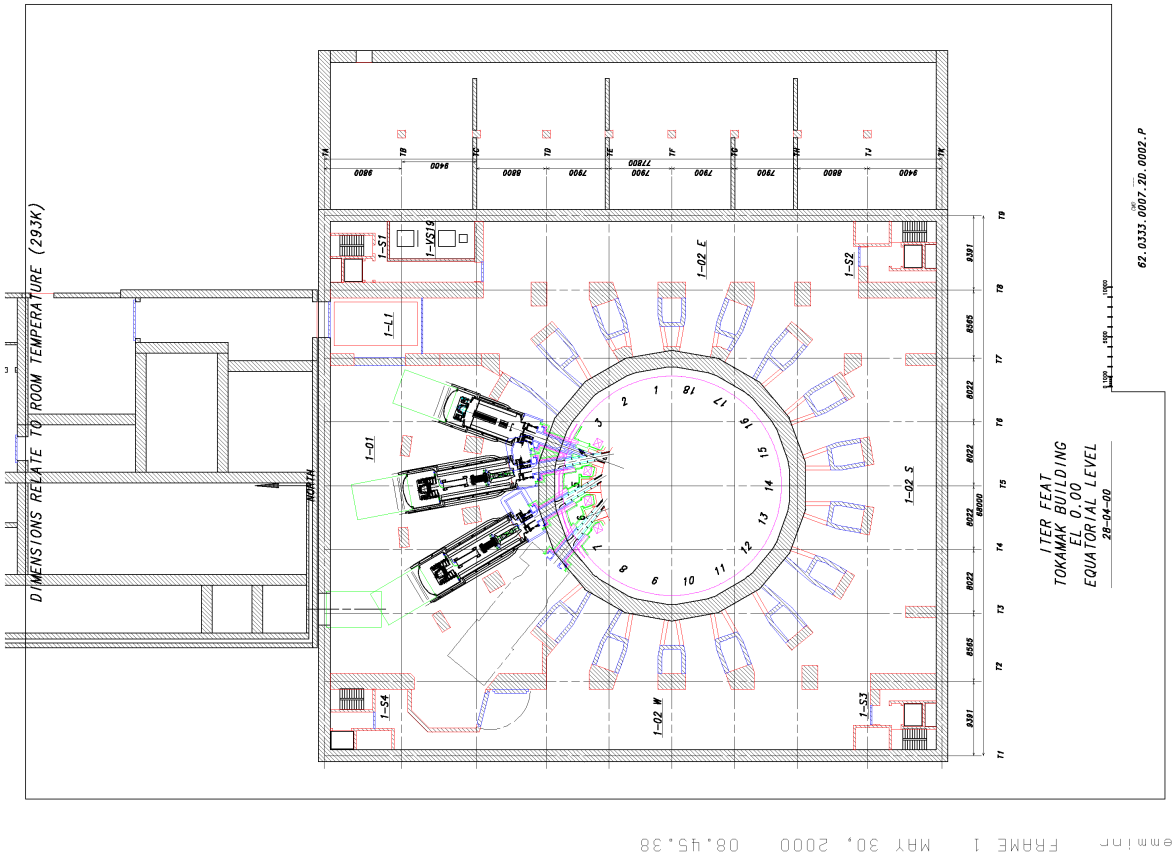

Figure 5.1-1(a) **Tokamak Building Floor Plan at Equatorial Port Level Showing Vertical Penetrations.**

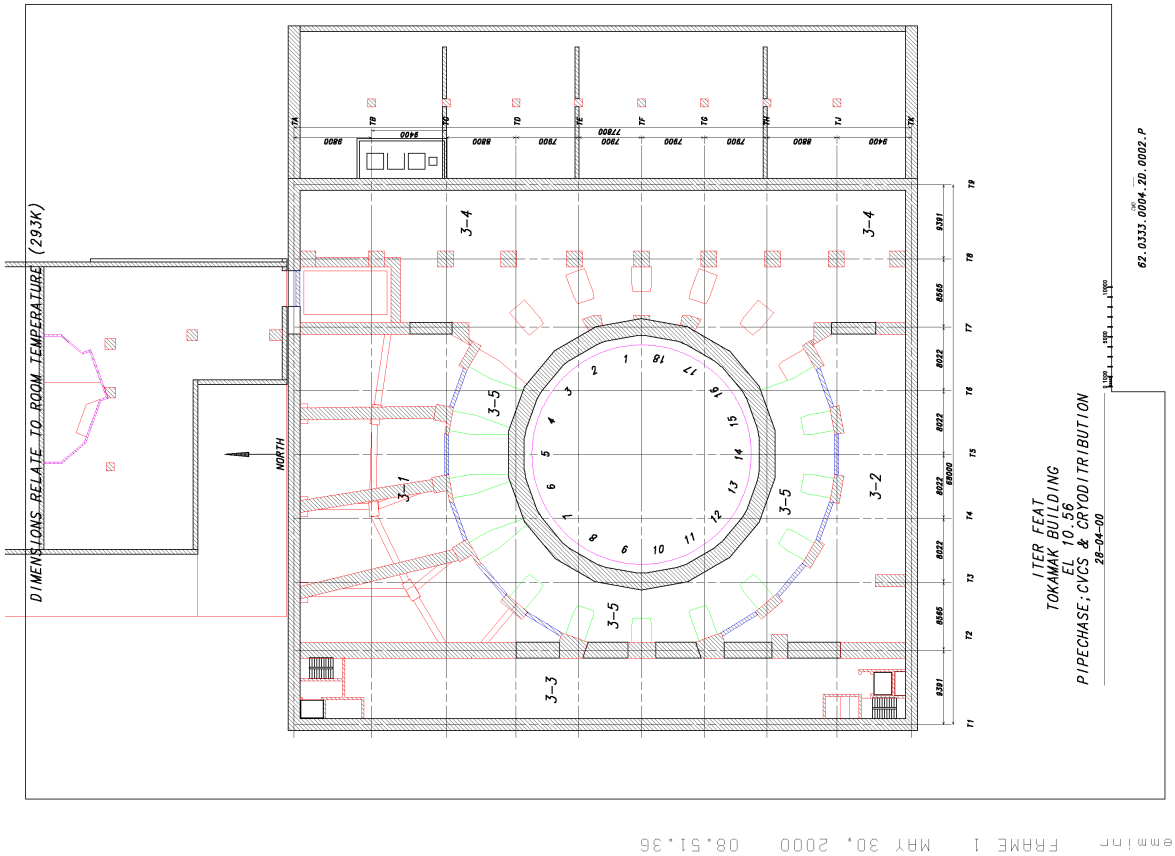

Figure 5.1-1(b) **Tokamak Building Floor Plan at the TCWS Level Showing Vertical Penetrations.**

These studies have so far not identified any problems and have relieved previous concerns on the ability to achieve the necessary vertical access.

Combined Tokamak and Tritium Building on a Common Basemat

In examining the layout of the tokamak building and the tritium building, and in reviewing the connections that are required between these buildings, it became apparent that there was a significant advantage in locating them on a common basemat. The first reason was safety and in consideration of the seismic event that safety systems and hazardous systems are required to be designed for. Placing the two buildings on a common basemat allows us to ignore the "seismic gap" that would otherwise be required between such buildings to allow for insertion of sufficient length of flexible connections such that they would survive the design basis earthquake. This gap would have to be of the order of 500 mm to 1500 mm, depending on the nature of the connecting components, whether it was a small diameter pipe, a large HVAC or VDS duct, or cables or power supplies. Further, once the combined building is on a common basemat, there is much more flexibility in the design of the tokamak building services, especially the HVAC and various detritiation systems, and it allows for expansion of tokamak building-related services where required. Also, a common basemat reduces the complexity of analyzing the structures.

This feature is shown in Figure 5.1-2.

Diagnostic Hall

In a continuing effort to simplify and combine functions of buildings and to minimize costs, the Diagnostic Hall has been added to the west side of the tokamak building. The diagnostic hall is 20 m by 63 meters, and has a number of floors dedicated to diagnostic instrumentation and cubicles. In addition, the building also houses the TF coil fast discharge resistors and capacitors, and also serves as the electrical busbar feed to the tokamak building. Figure 5.1-3 show the proposed layout of the diagnostic hall. There is ample room in this building for air conditioning units as well as for load centres. The main components of the diagnostic hall are the diagnostic instrumentation, and these are tied to the tokamak building as shown in the following figure.

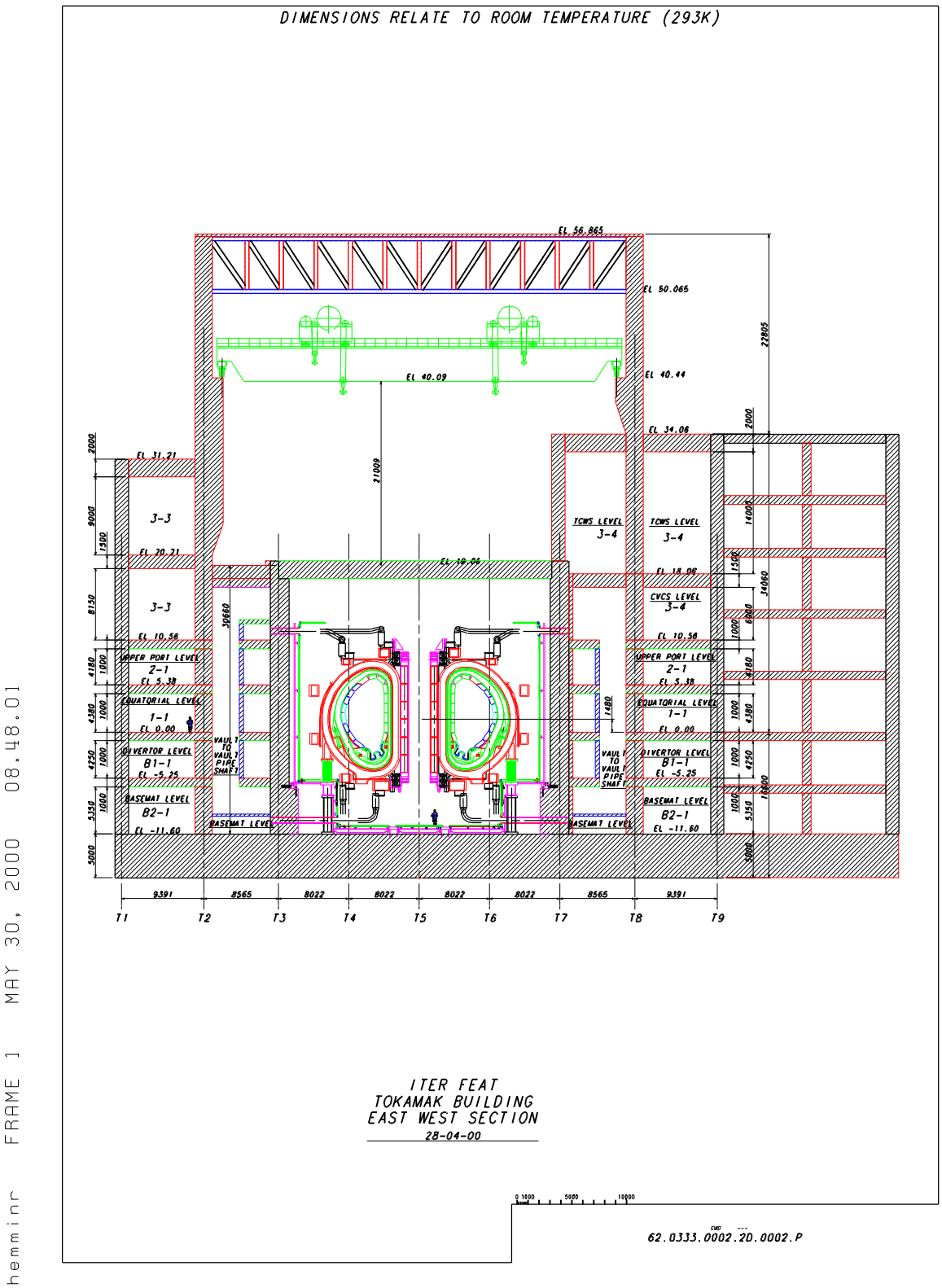

Figure 5.1-2 Tokamak and Tritium Building on Common Basemat

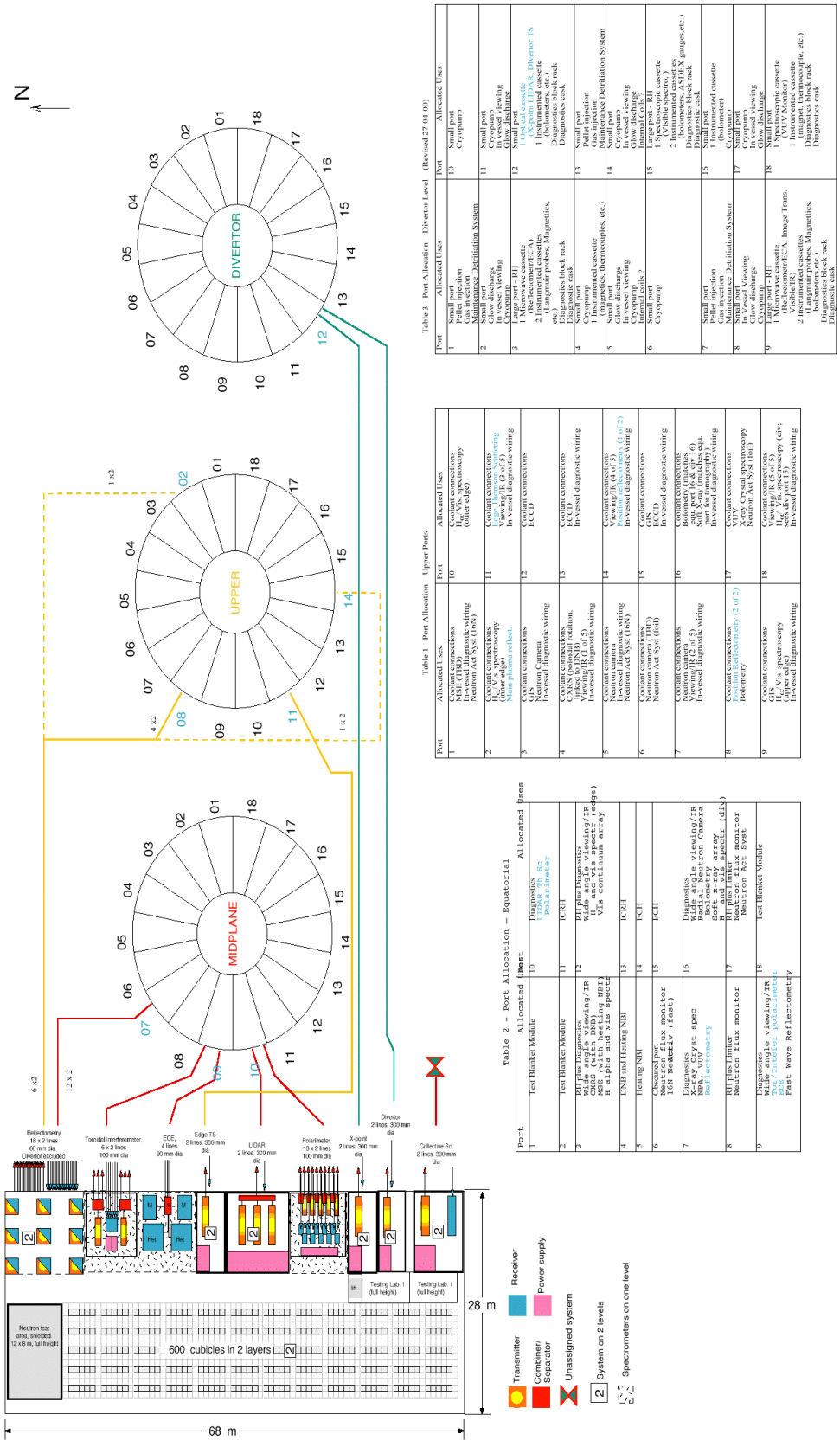

Figure 5.1-3 Diagnostic Hall Showing Links to Tokamak Building

5.2. Hot Cell Building

5.2.1. Building Size and Layout Requirements

The rationale for the conceptual hot cell building layout and size (Figure 5.2-1, 5.2-2 and 5.2-3) are determined by the maintenance requirements and by a few main design features which have evolved from a number of studies and reviews which particularly aimed at simplification of the remote processes. The main features and requirements for space are given below:

(a) hot cell arrangement on one (ground) level;
(b) in-line (i.e. during maintenance shutdown) repair and refurbishment concept (assumption for the present layout);
(c) common in-vessel component refurbishment area is used instead of dedicated hot cells;
(d) common in-vessel component storage is used instead of dedicated cells;
(e) common radioactive waste processing and storage area is used instead of dedicated cells;
(f) common repair/test area for all diagnostic and RF heating port plugs including interspace blocks;
(g) component receiving/dust cleaning cell with required three docking ports that, together with current dimensions of transfer casks, determine the size of hot cell transportation/docking area;
(h) RH tool exchange holding and repair/storage area;
(i) RH equipment test stand and transfer cask storage area on top of the hot cell building;
(j) new parts and components receiving and storage area;
(k) cranes/manipulators and transportation devices retraction/maintenance space;
(l) ADS/VDS/HVAC space (see below);
(m) load center area for services such as lighting and power supply;
(n) biological shielding, air locks, access and escape routes for personnel.

The sizing of the hot cell receiving room, processing room and storage space is based on meeting the requirements for maximum allowable maintenance duration. The sizing of the hot cell receiving room is based on unloading and loading of three casks during the same shift. The process room size is based on simultaneous refurbishment of one divertor cassette and one blanket module. In parallel, port plugs can be refurbished and tested by insertion in special port interfaces. The storage space is based on simultaneous storage of 24 blanket modules, 16 divertor cassettes and 6 port plugs. The detailed refurbishment procedures and the necessary RH equipment are still under detailed study. It may therefore be expected that further design optimization will be applied.

Most of the other room sizes are a logical consequence of their functional requirements, i.e., space needed for casks to maneuvering, space for equipment, e.g., HVAC, etc.

The wall thickness is based on the shielding and structural requirements. The current maximum thickness of 1.35 cm (normal concrete of 2.35 g/cm^3 density) for the walls that

separate access zone D from access zone B was defined for the 1998 ITER design[101], and need to be checked for ITER-FEAT.

5.2.2. ADS/VDS Requirements

The required hot cell ADS capacity is based on in-vessel component tritium release rate and derived air concentration (DAC) within the hot cells. Based on the tritium release rate best estimate of 6 TBq/hr (3 TBq/hr for the divertor and 3 TBq/hr for the other in-vessel components) of the "cold" torus with some dust and co-deposited tritium cleaning, it was found that the tritium off-gassing rate per cassette is 1.5 Ci/hr and ~ 0.2 Ci/hr per blanket module.

Taking into account the tokamak maintenance logistic design study, no more than 11 divertor cassettes can be within the hot cells at the same time, giving a tritium out-gassing rate of 16.5 Ci/hr. There also could be two port plugs or 6 blanket modules at the same time, giving an additional 1.2 Ci/hr. In total the tritium out-gassing rate within the hot cells (receiving, storage, refurbishment, waste processing) is ~18 Ci/hr as basis value for ADS capacity calculation. The ADS design capacity of 4500 m^3/hr provides a DAC value of 500.

A VDS design capacity of 500 m^3/hr is proposed based on a 100% volume/day in-leakage rate for all rooms of the hot cell building. A normal VDS capacity of 316 m^3/hr is determined by 100% volume/day air in-leakage rate for the 4 zone D hot cells and their total volume of 7630 m^3.

The standby VDS capacity depends on the following scenarios:
1. accidental tritium release,
2. work with temporary localized secondary enclosures,
3. purge and detritiation of contaminated equipment.

The standby VDS capacity of 160 m^3/hr was calculated based on 100% volume/day air in-leakage rate and the volume of 4 zone B rooms which may simultaneously require VDS.

5.2.3. Dose and Dust Requirements

The expected surface contact dose levels of tokamak components stored within the storage cell, are listed in Table 5.2-1 (1998 ITER design):

[101] "Hot Cell Building Shielding Criteria." ITER Task D230-C5. January 1996. IBERTEF.

Table 5.2-1. Hot Cell Component Surface Contact Dose Levels (Dose in Sv/h)

Component	Time After Shutdown			
	30 days	90 days	150 days	1 year
Limiter Module	1.4E+03	9.2E+02	6.6E+02	3.1E+02
IBB Module	9.5E+02	6.2E+02	4.4E+02	2.1E+02
OBB Module	1.4E+03	9.2E+02	6.6E+02	3.1E+02
Divertor Body & Dome	9.5E+02	6.2E+02	4.4E+02	2.1E+02
Divertor HHFC Stainless Steel	9.5E+02	6.2E+02	4.4E+02	2.1E+02
Divertor HHFC Copper	4.1E+02	3.6E+02	3.3E+02	2.7E+02
Divertor HHFC Tungsten	2.0E+02	1.4E+02	9.4E+01	2.8E+02

Even though the tokamak will include provisions for dust removal, it is assumed that considerable amounts of dust on components (mainly divertor cassettes) can be delivered to the hot cell area. Therefore, the receiving cell fulfils a double function as component cleaning facility, in order to minimize the amount of activated dust inside the hot cell processing and storage areas.

5.2.4. Design Outline

The HCB is organized on two main levels, with the main hot cell functions on the ground floor, include in-vessel component docking, dust cleaning, storage, repair/testing, remote handling (RH) tools exchange/ maintenance, waste processing and waste storage/shipping, and new parts/ components receiving/storage. Upper level functions include RH equipment test, transfer casks storage, atmosphere confinement control and atmosphere detritiation equipment.

The hot cell building is available during the initial installation phase of the tokamak in-vessel components to provide a pre-assembly, Be-controlled area and a facility for loading components into transfer casks.

The hot cell building is designed such that it can be expanded to meet future increased processing capacity needs, e.g., for the decommissioning phase of ITER.

Port plugs requiring refurbishment will not normally be off-loaded into the HC receiving cell but instead be installed inside the special docking ports, to allow remote refurbishment from inside the HC and hands-on maintenance at the front side of the plug, including functional testing, if required.

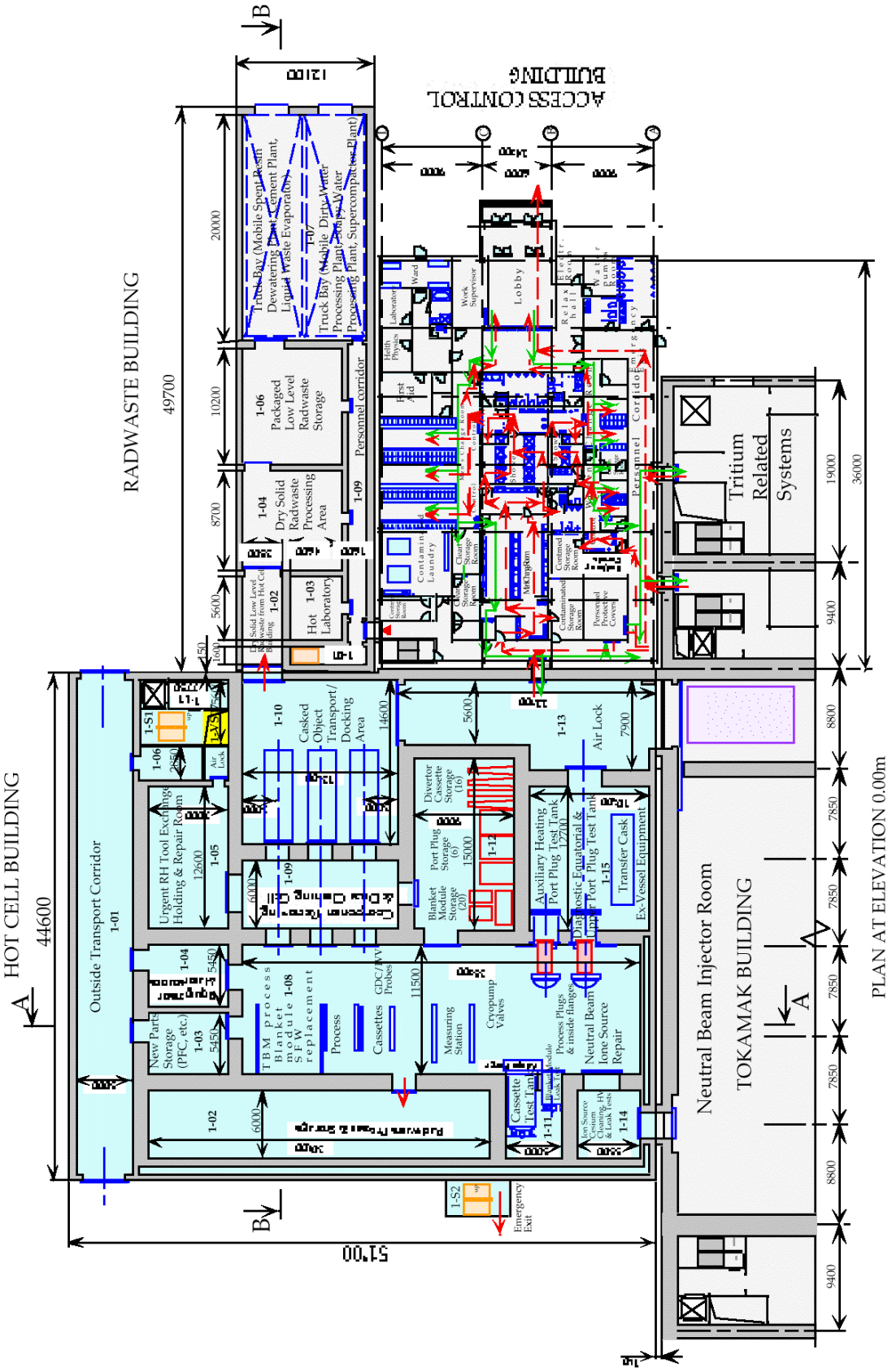

Figure 5.2-1 Hot Cell Building Ground Floor Plan

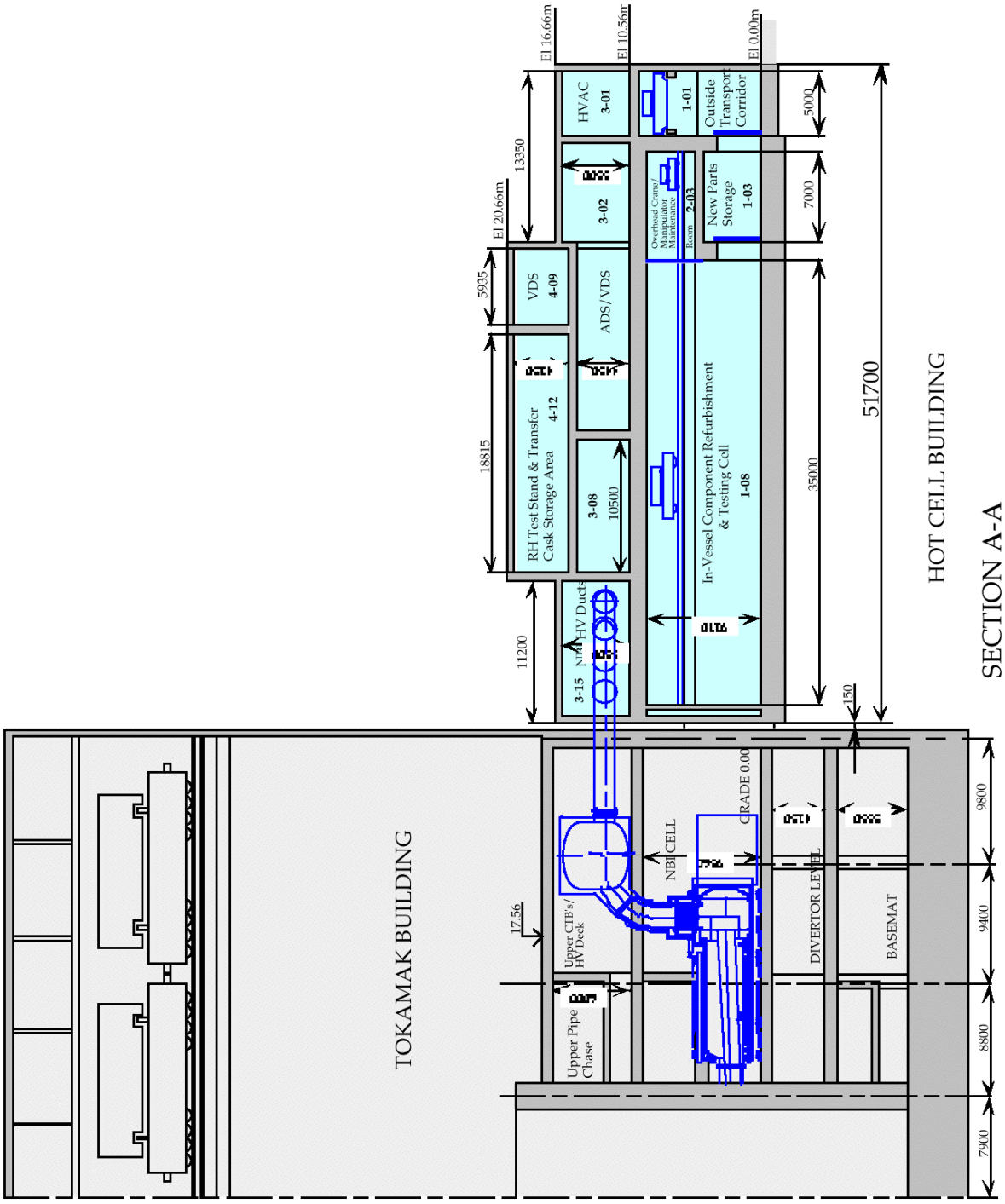

Figure 5.2-2 Hot Cell Building Horizontal Section AA in Figure 5.2-1

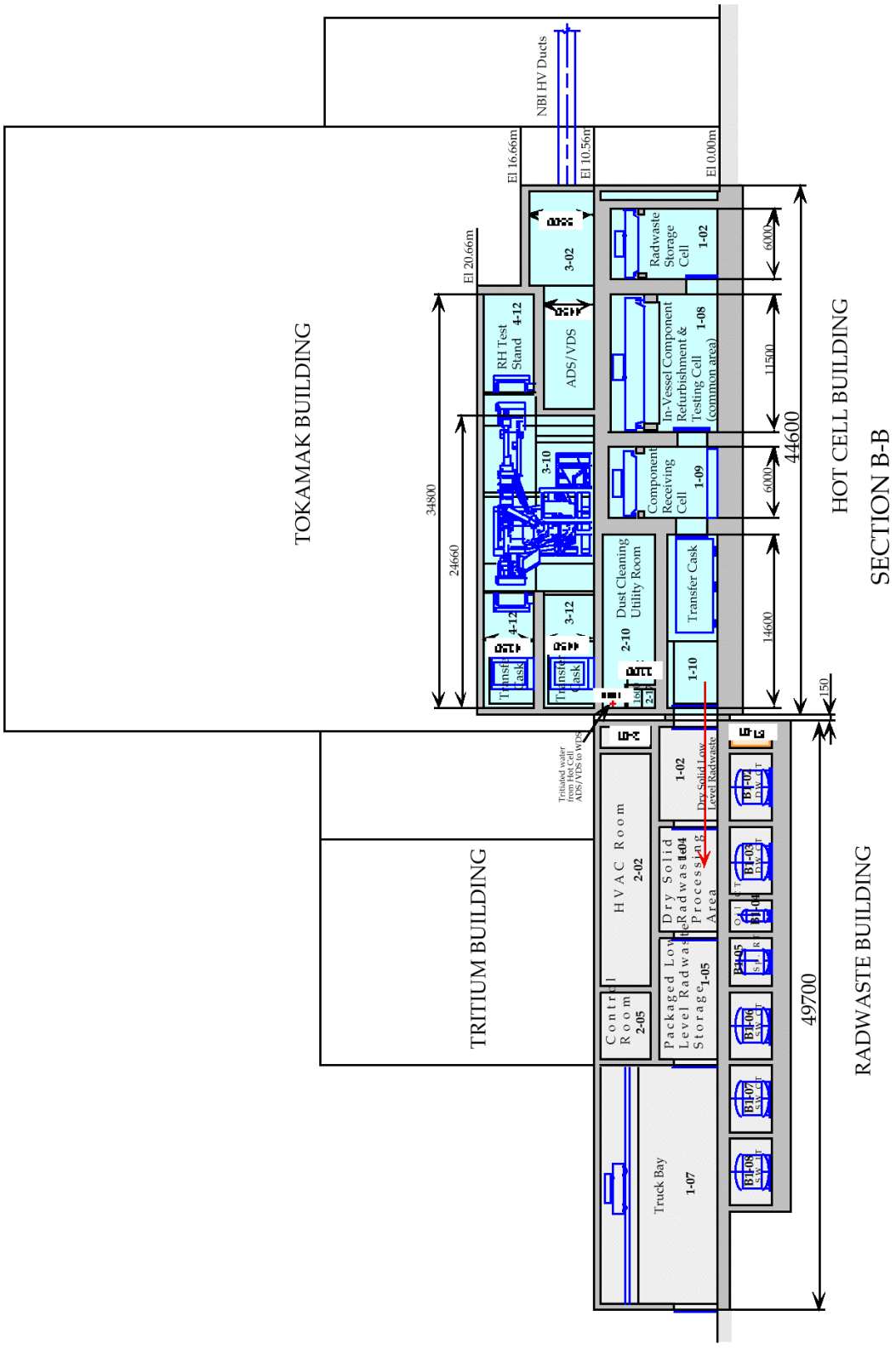

Figure 5.2-3 Hot Cell Building Vertical section BB in Figure 5.2-1

5.2.5. Hot Cell Docking and Storage System

The hot cell docking and storage system consists of six major subsystems as described below.

Docking Sub-System

The cask transportation system provides the passage of transfer casks from the tokamak building to the hot cell docking ports and provides the appropriate rotations of the transfer casks in the docking area (transport corridor). The docking ports, which have identical double-seal door systems to the corresponding docking ports in the tokamak pit, provide hermetical connection of the transfer casks to the receiving cell. The receiving cell with three docking ports connects to three cells, namely: in-vessel component storage cell, in-vessel component repair/ refurbishment cell, and urgent remote handling tools exchange holding and repair cell. Within the receiving cell, dust cleaning operations for all received objects are carried out.

The docking ports have exchangeable docking adapters, which enable a port to receive different types of tokamak components (except a NB ion source) during a maintenance campaign. There is a dedicated docking port for the NB ion source transfer cask. Direct-access docking from inside the tokamak NB cell is available for maintenance operations on NB ion sources, should this be required.

Dust Cleaning Sub-System

This sub-system provides the clean up of dust on components and RH tools delivered by transfer casks from the tokamak to the receiving cell. Although the tokamak will include provisions for dust removal, it is assumed that dust on components (mainly divertor cassettes) can be delivered to the hot cell area. To prevent contamination from spreading, dust is thoroughly removed from components. The dust recovered by the primary collector is enclosed in the dust canister. The cap of the canister is equipped with a porous sintered metal filter to enable baking the canister for further detritiation, should this be required.

Nitrogen Purge Sub-System

After transfer cask undocking, the atmosphere in the transfer cask must be purged with nitrogen.

Storage Sub-System

The sub-system acts as a buffer between tokamak remote maintenance operations and hot cell repair/waste operations. Objects such as divertor cassettes are withdrawn from the tokamak and then delivered to the hot cell storage sub-system, which places them into storage locations before repair/waste processing. All transportation and storage functions are performed remotely within shielded cells in the hot cell building.

In order to support the process operations a storage cell is provided. This storage cell is dedicated to in-vessel components, which are expected to be changed several times during the life of the ITER plant.

Remote Handling Tool Storage/Repair Sub-System

A storage cell is provided for urgent RH tools, which are immediately needed for exchanging without undocking the transfer cask from the receiving cell during a tokamak maintenance campaign. Rotation of the RH tools within this cell corresponds to the operational sequence of the object replacement schedule.

After dust cleaning of RH tools (if needed) inside the receiving cell, the repair activities within the RH tool storage/repair cell can be carried out by "hands-on" procedures. Access for workers into this cell could be provided through an air-lock.

Control, interlock and monitoring

All hot cell systems and equipment status, as well as environmental conditions and interlock system status are provided to the supervisory control system.

5.2.6. Hot Cell Repair/Testing System

The hot cell repair/testing system processes components which have become activated by neutron exposure and/or contaminated with tritium or activated dust particles and which have been removed from the tokamak for repair or refurbishment and testing prior to return to service. Remote handling tools and equipment, which are used for removal /installation of tokamak components are also repaired and returned to service.

The processing includes examination, preparation of service plans, preparation of samples for material evaluation, evaluation and segregation of parts into those which can be reused and those which must be replaced, disassembly, replacement of parts, re-assembly, and inspection/testing. Components, which enter the system for repair, may be diverted, following evaluation, to the hot cell waste processing system. The system includes equipment for monitoring and control of all repair/testing operations.

The system comprises the following processing stations and system elements:
1) Divertor cassettes plasma facing components (PFCs) replacement workstation
2) Blanket module separable first wall (SFW) replacement workstation
3) Equatorial and upper port plugs repair/test tanks (ICH&CD, ECH&CD and diagnostic plugs)
4) Cryopump valves repair
5) NB ion source repair/testing
6) Two testing tanks for divertor cassettes and blanket modules, respectively
7) New parts/sub-components storage room
8) Transporters
9) Equipment maintenance facility

5.2.7. Hot Cell Waste Processing and Storage System

The hot cell waste processing and storage system processes and storse solid radioactive materials which have been removed from the tokamak and which will be discarded. The hot

cell waste processing and storage system is designed to process discarded tokamak materials, which have become activated by neutrons, and/or contaminated with dust/tritium.

Waste processing includes disassembly, cutting, preparation of samples for material evaluation, containerization of radwaste, and recovery of tritium from plasma-facing components and T-contaminated dust, if required. The hot cell waste processing and storage system provides up to 2 months storage of radioactive waste. The specific waste processing and storage operations are determined by the nature of the component, its state of degradation, the extent and nature of its radioactivity, the level of tritium contamination, and the host country regulations for processing and packaging radwaste for final disposal.

5.2.8. Hot Cell Radioactivity and Toxic Material Control System

The hot cell radioactivity and toxic material control system provides high level radiation shielding, as well as airborne tritium and radioactive/toxic dust confinement. The necessity to address tritium and toxic Be dust distinguishes the ITER hot cell from most other hot cells.

Three access control zones are utilized, which regulate access according to exposure conditions and contamination levels. The hot cell atmosphere is controlled by dividing the work areas into ventilation groups according to the hazard level of airborne tritium. Assignment of work areas to specific ventilation groups is based on the DAC of HTO. Areas with the highest tritium levels are assigned the lowest room pressure, so that the leakage is always from lower to higher tritium concentrations.

To minimize tritiated water generation from air in-leakage, low humidity (dried) air is circulated through the air spaces around the hot cells. Thus, only dry air is subject to inleakage. In this way the generation of tritiated water is minimised.

Tritiated water is transferred from the hot cell atmosphere detritiation system (ADS) and vent detritiation system (VDS) into the water detritiation system (WDS) of the tritium building.

6. Operation

6.1. Limits to Pulse Length

The ITER-FEAT pulse length is limited by:
1) the available inductive flux or current drive power installed;
2) the number of torus cryopumps installed;
3) the heat rejection capacity of the site cooling water system;
4) the processing capability of the tritium plant.

In the design of the TF conductor, nuclear heating has been considered as a steady state heat load. Therefore, the TF coils are compatible with steady state operation at 15 MA without any modification of the cooling conditions.

For cooling water equipment, the critical system is the heat rejection system, e.g. the basin size and cooling tower capacity. The other systems have no limitation because they have full steady state capacity for a fusion power of 500 MW plus 100 MW of additional heating.

The cooling tower design considers the temperature levelling effect in the hot basin and is sized for the maximum allowable temperature in the hot basin with a flat top of 500 s and the worst atmospheric conditions (highest air temperature and humidity). Any increase in pulse length leads therefore to a higher temperature in the cold basin which feeds the tokamak components.

The temperature levelling effect in the basins and the cooling tower characteristics under the worse air condition and cooler condition has been evaluated[102]. The allowable pulse duration with 500 MW of fusion power and 100 MW of additional heating power, in the case of the worst atmospheric (nominal) conditions, are:
- ~2000 s in the case of full mixing in the hot basin only;
- ~4000 s in the case of full mixing in both hot and cold basins.

Full mixing may require additional investment.

In the case that the air temperature is lower than 26.1 ºC (winter case), studies[103] have shown that an infinite pulse duration can be accommodated.

For the T-plant, the design scenario assumed was that the 6 cryopumps would pump all exhaust gas throughout the full pulse length (~ 450 s) and be sequentially regenerated during the dwell time. The processing capacity of the T-plant could therefore be limited to approximately 30% of the fuelling rate. This has considerable cost advantages and reduces the loop inventory. The storage onto cryopumps is limited by the total inventory in the VV as well as by the deflagration limit of the hydrogen stored on cryopumps. The latter limit is generally reached before the former. Increasing the burn time significantly beyond the inductive limit, requires the regeneration of pumps during plasma operation, and the installation of 10 pumps so that some may be under regeneration during the burn.

There are two ways, or a mix of the two, to upgrade the T-plant for long pulse operation.

[102] Technical basis for the ITER-FEAT Outline Design Report G A0 RI 2 00-01-18 R1.0 Chapter II.5
[103] Y. Kataoka, “Cooling tower design and operable duration under steady state condition”

(i) Increase the processing capacity to allow full steady state operation. Using simple engineering cost scaling factors, this would roughly double the cost of the front-end permeators, impurity processing and isotope separation system (ISS). Moreover, it would also significantly increase the inventory in the loop, particularly in the ISS.

(ii) Replace intermediate storage on cryopumps with intermediate storage on hydride beds. This would require an increase in the capacity of the front-end permeator and the addition of some 10 (or more) hydride beds. The exact number of additional beds depends on a number of factors that are under study. This upgrade would also significantly increase the tritium inventory in the fuel cycle loop.

Method (ii) can, in principle, be added at a later stage to the plant. It is likely to be cheaper than (i), but this needs confirmation. The main drawback of method (ii) is that the unloading of the hydride beds used for interim storage of the tokamak exhaust, after passing through the front-end permeator, and preparations for reloading, take considerable time, and requires the processing of the large batch of exhaust gas with up to ~780 g of tritium. Therefore, if long pulse operation should be envisaged as routine operation or as a frequently used scenario, method (i) would be the natural choice.

6.2. Limits to Fusion Power

The TF coils can tolerate, in steady state conditions, the nuclear heating associated with the 17 MA scenario by increasing the cryogen mass flow rate in the conductors from 8 to 10 g/s.

The cryoplant can accommodate steady state operation with a fusion power of 700 MW. This assessment is based on the current values of the heat loads.

When a larger fusion power, but with much shorter burn time (typically 100 s), is considered, a proper transient thermohydraulic analysis is required. In this analysis, the heat capacity of the TF coil metal parts (case, radial plate) plays a role to limit the rate of rise of the conductor temperature, and the electrical insulation layers (turn and ground) act as thermal barriers to slow down the diffusion of heat into the conductor. Requirements on mass flow rates are expected to be reduced as compared to those found for steady state conditions.

For the ex-vessel portion of the water cooling system, the maximum pulse duration with 700 MW of fusion power has been evaluated[104]. The maximum pulse duration is limited by the allowable maximum inlet temperature for the in-vessel components. The higher fusion power results in an increase of the inlet temperature due to the mismatch between the heat load and the heat which can be rejected through the heat exchanger.

The results show that the allowable pulse duration varies between ~60 s (nominal case) and ~260 s (winter case). From these results, it is concluded that ~700 MW is the maximum power when a pulse duration longer than 100 s is required.

[104] Y. Kataoka, "Study on allowable duration of high-beta operation for heat removal systems"

7. Safety

7.1. Methodological Improvements

In December 1999 the TAC recommended that:

"*comprehensive and integrated safety assessments should be conducted in future to be consistent with the detailed design work, with particular attention paid to the licensability of ITER/FEAT. Further refinement on the estimation of source terms arising from the radioactive inventory is to be encouraged in order to characterise the nuclear aspects of ITER and improve the safety and licensing process in the Parties*"

If the releasable inventory can be kept below a value such that dose limits in a Host Country are not exceeded even if the entire amount is released, it is expected that the licensing process will be simplified because the details of the accident sequence become much less important in demonstrating that dose limits are met. Tritium and in-vessel dust inventories were reviewed at the Point Design Meeting (Naka, February 2000). Aggressive targets for tritium inventories for in-vessel and the fuel cycle were set (subject to confirmation of feasibility) based on a review of Japanese and Canadian dose limits and typical site characteristics.

Tritium Inventory Guidelines

Tritium Inventory	Guideline
Maximum mobilisable inventory within the vacuum vessel [g]	≤ 450 (working guideline subject to confirmation of feasibility)
Maximum mobilisable inventory in the pumping and fuelling systems and the tritium plant [g]	≤ 450 (working guideline subject to confirmation of feasibility)
Long-term storage [g]	≤ 450 per independent storage area
Maximum mobilisable in hot cell [g]	≤ 250

Key issues of in-vessel dust and tritium removal and monitoring are addressed in section 4.3.

The extensive analysis base available in NSSR-2 is being used to improve the implementation of safety in the design. Specifically, the confinement approach is being reviewed and refined to obtain a balance of safety requirements imposed on the systems with confinement functions. Safety-related specifications for a system or component comprise two parts:

- minimum performance specifications assumed in the safety analyses (e.g. leak tightness, detritiation efficiency, heat removal capacity, etc.)
- level of assurance, reliability, or degree of confidence required from the system or component to be consistent with the assumptions in the safety analyses.

An initial set of minimum performance specifications have been developed in the Plant Safety Requirements. It is expected that as the design progresses and the ITER-FEAT safety analysis results become available, there will be changes in specifications.

The pre-1998 ITER safety design approach used the idea of "two strong barriers" for confinement and placed nearly equal weight on all safety functions (i.e. confinement, heat removal, control of chemical energy, control of magnetic energy, control of coolant enthalpy, etc.). For ITER-FEAT, having the detailed results from NSSR-2 available as background, the safety design focuses on confinement as THE safety function; the others being recognised as required to protect confinement barriers. A "lines-of-defence" (LOD) methodology is being used to provide the initial identification of systems providing confinement. The benefit of the LOD approach is that it provides a systematic method to obtain the required level of safety while balancing the requirements imposed on systems and components. The number and characteristics of an approach depends upon the inventory at risk. Two types of lines of defence and an equivalence rule are considered.

- A **very reliable LOD** (type 'a') results from robustness, redundancy, conservatism, and inherent or passive features. These lines of defence would be analogous to systems characterised by an unavailability of less than 10^{-3}-10^{-4} per demand or by a failure rate (or occurrence rate) less than 10^{-3}-10^{-4} per year.

- A **reliable LOD** (type 'b') does not have the same degree of conservatism that is characteristic of a type 'a' LOD. These lines of defence would be analogous to systems characterised by an unavailability of less than 10^{-1}-10^{-2} per demand or by a failure rate (or occurrence rate) less than 10^{-1}-10^{-2} per year.

- Multiple, diverse/independent type 'b' LODs can be considered equivalent to a type 'a' LOD if their combined reliability is consistent with the reliability of a type 'a' LOD.

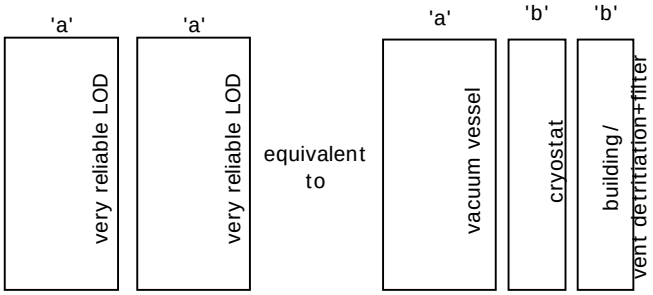

The general confinement approach being implemented for systems that penetrate the vacuum vessel and cryostat, such as diagnostics, is to provide a pair of windows or isolation valves (e.g. windows are considered a type 'b' line of defence) capable of withstanding the pressures, temperatures, forces, radiation conditions, etc., and a means (e.g. rupture disk or perforated wave guide) to ensure venting into a room where the discharge can be filtered, detritiated and monitored, in the case of an in-vessel accident with failure of the windows. A system by system review if being carried out by the safety group and designers to ensure an acceptable design.

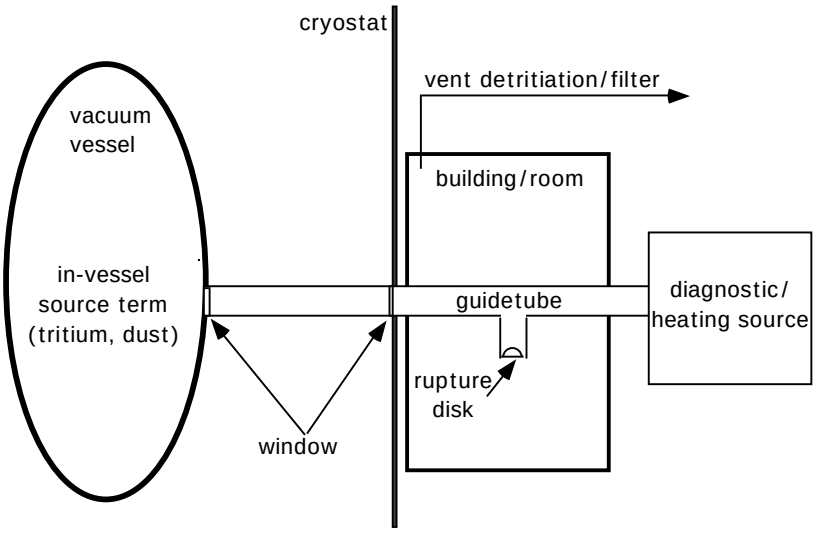

7.2. Design Changes due to Safety Considerations

As noted in the Outline Design Report, detailed analysis of the design is needed to clarify the conditions under which the technical need for a stack for ITER-FEAT can be avoided. The dependence on a high stack may reduce the safety attractiveness of ITER-FEAT for siting and fusion in general. For NSSR-2 it was assumed that a 100 m stack existed in determining the appropriate release guidelines to use as acceptance criteria. In all but a couple of accident sequences, releases were orders of magnitude below release guidelines. If inventories are kept to reasonable values or reduced (as noted in section 7.1), confinement improvements are implemented to avoid or mitigate “bypass events” (as noted in section 7.1), and estimates of operational losses are reduced (in progress), then a tall stack is not needed to meet project release guidelines. A controlled, monitored release point is still needed, and the height could be increased if needed for Host Country licensing.

The TCWS vault, pipe chases to the vault, and the NB cell provide part of the confinement barrier for the in-vessel and TCWS source terms. The TCWS vault and NB cell are designed to be leaktight and withstand pressures following coolant spills. Exhaust from these areas can be treated by filters and detritiation systems and is directed to the monitored plant exhaust.

It is only during pulsed operation of the plasma (coolant temperatures ~ 150°C) that an ex-vessel LOCA can lead to in-vessel failures and hence potentially release the in-vessel source term (tritium, dust) into the TCWS vaults. The stainless steel piping used in the TCWS piping is ductile, and incipient failures will be revealed by leaks before any crack reaches a critical crack size. For such materials and with a reasonable leak detection system, double-ended guillotine failures can be considered "hypothetical events". Nonetheless, the TCWS vault and its connected volumes can also confine the pressure caused by any pipe failure during plasma operation up to and including a double-ended guillotine rupture. A pressure of ~200 kPa(a) is adequate to confine such a release with a margin to allow for computational uncertainty. In addition, the TCWS vaults are designed to confine the pressures resulting from a leak in the TCWS piping under any foreseen operating conditions. Due to the higher

temperatures, a leak during machine baking conditions (coolant temperatures ~240°C) is limiting. A pressure of ~200 kPa(a) is also adequate to confine such a leak.

In assessing the ultimate safety margins of ITER-FEAT, "cliff edge effects", where the consequences increase significantly if some parameter increases, should be avoided. In the case of the TCWS vault, a failure of the vault due to overpressure is avoided by having the pressure relieved by blow out panels to the environment. The releases would be limited to tritium and activated corrosion products (ACP) in the TCWS loop which are below Category IV (Extremely Unlikely Event) release guidelines.

This approach of confining breaks even up to double-ended guillotine failures during plasma operation adds margin to the design and decreases the importance to public safety of being able to correctly predict critical crack sizes and leak rates and of having a sensitive leak detection system capable of working under transient conditions such as during a pulse.

An important issue for water-cooled plasma-facing components with beryllium is the beryllium steam reaction that can occur during accidents when there is an ingress of coolant into the vacuum vessel. This reaction is exothermic and leads to production of hydrogen. The approach in ITER-FEAT is to limit the potential production of hydrogen by controlling the amount of reactive dust on hot surfaces and limiting long term temperatures under accident conditions. Of particular concern is the consequence of a problem with heat removal from plasma facing components while the plasma continues. To mitigate the potential for Be-steam reactions after ex-vessel loss of cooling accident a design study will be done with the objective to develop pockets of liquids (e.g. water) which will burst into the plasma chamber at high temperature (about 400°C) and terminate the plasma burn. The estimated water amount needed in these pockets is a few cm^3. The pockets will be in the shadow of the plasma about 5-10 cm away from the first wall surface. Two pockets will be installed per cooling loop (preferably on equatorial modules), i.e. a total of 6 modules will be equipped with these pockets. If successfully developed, the need for safety credit of the fusion power shutdown system may vanish.

7.3. Safety Assessment

The initial assignment of Safety Importance Classification (SIC) to all ITER-FEAT systems and components has been completed taking into account issues identified in the 1998 ITER design and safety assessment, and the above methodology. The implications of an assigned Safety Importance Classification in terms of design, fabrication, testing, operation, etc. is also being addressed in more detail. The assignment of Safety Importance Classification, and implementation in the design, is being refined as the design progresses and ITER-FEAT safety analysis becomes available.

The Generic Site Safety Report (GSSR) will document the safety assessment of ITER-FEAT, and it will follow the structure and content of the previous Non-Site-Specific Safety Report (NSSR-2) produced for the 1998 ITER design:

Volume I	Safety Approach
Volume II	Safety Design
Volume III	Radiological and Energy Source Terms
Volume IV	Normal Operation
Volume V	Radioactive Materials and Waste

Volume VI	Occupational Safety
Volume VII	Analysis of Reference Events
Volume VIII	Ultimate Safety Margins
Volume IX	External Hazards Assessment
Volume X	Sequence Analysis
Volume XI	Safety Models and Codes

In addition to providing evidence to the Parties that the design of ITER is sound, the GSSR is intended to assist potential Host Countries in the preparation of regulatory submissions for siting. Regulatory submissions must be prepared by experts from the Host Country familiar with the regulatory requirements and regulator's expectations. At this stage in the Project, the GSSR can support siting decisions, but further design detail and Host-Country-specific safety assessments are likely to be needed to obtain regulatory approval for construction.

At the Technical Meeting on Safety and Environment held in Garching, February 2000, the contents of GSSR, and in particular, changes from NSSR-2, were reviewed and agreed with Home Team safety experts, including representatives from Japan and Canada who are in discussions with their regulators about licensing ITER. The detailed contents of each volume were discussed, and the tasks to provide the underlying analysis agreed by the JCT and Home Teams. In particular, the extent of update needed for the sequence analysis, the set of reference events, and the scope of analysis for ultimate safety margins, were agreed upon.

Maintaining consistency between the evolving design and the safety assessments is facilitated through the use of bounding assessments to accommodate design evolution and the use of a Safety Analysis Data List and Analysis Specifications for each volume used by all contributors to GSSR. These will be updated periodically to reflect the latest safety-relevant design parameters. This approach was proven successful in producing NSSR-2.